

AN ABSTRACT OF THE THESIS OF

Weinan Zhao for the degree of Master of Science in Chemical Engineering presented on December 5, 2017.

Title: Density Function Theory Study of CO₂ Dissociation on Ni and Ni Based Alloy Surface

Abstract approved: _____

Líney Árnadóttir

Abstract: The corrosion and degradation of Ni and its alloys in supercritical carbon dioxide (Sc-CO₂) is an emerging issue for material selection and implementation of Sc-CO₂ thermal cycles in industry. In this study, we apply density functional theory (DFT) to study the initial steps of carburization of the Ni (111) surface and two types of Ni-Cr alloy surface in a CO₂ environment. The overall carburization reaction, CO₂ ↔ C_{ads} + O₂ can be broken into four elementary steps, CO₂ activation, two surface reactions, CO₂ dissociation to CO and O followed by dissociation of CO to O and C. In this study, we concentrate on the thermodynamics of the two surface reactions and determine their activation barriers. We determine the energy of the activate state of CO₂ and its dissociated products to compare the thermodynamics of the different elementary reactions steps. On Ni (111), activated CO₂ is most stable on a hollow site with adsorption energy of 0.24 eV, employing linear CO₂ as reference state, indicating that it is thermodynamically unfavorable. The coadsorption of CO and O, which are products of the first step of CO₂ dissociation, are most stable on fcc site and hcp site respectively. The interactions between the two adsorbates are slightly attractive. This initial CO₂ dissociation step is exothermic by 0.53 eV with a kinetic barrier of 0.61 eV. The further dissociation of CO to C and O on Ni (111) is endothermic by more than 2 eV and has large activation barrier, 3.38 eV. The results of these two elementary steps of CO₂ dissociation are in good agreement with previous literature. The high barriers makes this reaction path unlikely to be the main

reaction path for the carburization of Ni surfaces but co-adsorbates and surface defects are likely to play a major role in this process. The CO_2 dissociation step is also studied on two Ni based alloy surfaces, $\text{Ni}_{8.33}\text{Cr}_{1.67}$ and Ni_5Cr_5 . On $\text{Ni}_{8.33}\text{Cr}_{1.67}$, activated CO_2 is most stable on a bridge site with the energy of 0.18 eV, compared to a linear CO_2 in the gas phase, indicating that the interaction between CO_2 and alloy surface is thermodynamically unfavorable but more favorable than on Ni. The co-adsorption of CO and O, the products of the initial dissociation step, is most stable when two adsorbates stay on ontop site and hcp site, respectively. The interaction between the two adsorbates are still slightly attractive similar to the Ni (111) surface. The activation barriers for the two elementary steps of CO_2 dissociation are 1.44 eV and 1.90 eV, respectively. Both of these steps are exothermic with the reaction energy of 1.00 eV and 0.46 eV, respectively. The higher activation barrier for the first step compared to pure Ni surface indicates that Ni-Cr has a better corrosion resistance in Sc- CO_2 environment. A Ni_5Cr_5 alloy is studied to model Cr surface enrichment, on this surface activated CO_2 is most stable on fcc site with the adsorption energy of -0.76 eV, relative to linear CO_2 in gas phase, indicating that the interaction is thermodynamically favorable. In general, the interactions between CO_2 and the surface increase with Cr content. The co-adsorption of CO and O is most stable on bridge and hcp site with attractive interaction between the two adsorbates. The activation barrier for the first elementary step of CO_2 on Ni_5Cr_5 is 0.91 eV which is higher than pure Ni surface. The step is exothermic with the energy of 0.68 eV. Comparison of CO_2 dissociation on different Ni and Ni_xCr_y surfaces shows that the stability of $\text{CO}_{2,\text{ads}}$ increases with Cr content and the initial dissociation step of CO_2 to $\text{CO} + \text{O}$ has lowest barrier on the Ni surface of the surfaces studied suggesting a more rapid CO_2 dissociation on the Ni surface.

©Copyright by Weinan Zhao
December 5, 2017
All Rights Reserved

Density Function Theory Study of CO₂ Dissociation on Ni and Ni-Based Alloy
Surfaces

by
Weinan Zhao

A THESIS

submitted to

Oregon State University

in partial fulfillment of
the requirements for the
degree of

Master of Science

Presented December 5, 2017
Commencement June 2018

Master of Science thesis of Weinan Zhao presented on December 5, 2017

APPROVED:

Major Professor, representing Chemical Engineering

Head of the School of Chemical, Biological, and Environmental Engineering

Dean of the Graduate School

I understand that my thesis will become part of the permanent collection of Oregon State University libraries. My signature below authorizes release of my thesis to any reader upon request.

Weinan Zhao, Author

ACKNOWLEDGEMENTS

The author expresses sincere appreciation to Dr. Líney Árnadóttir and everyone who has had a major influence on his life. You know who you are.

TABLE OF CONTENTS

	<u>Page</u>
1. Introduction.....	1
1.1. Supercritical carbon dioxide (Sc-CO ₂) and its properties.....	2
1.2. Applications of Sc-CO ₂	3
1.3. Corrosion issue caused by Sc-CO ₂	6
1.4. Carburization corrosion mechanism.....	9
1.5. Ni and Ni based alloy.....	11
1.6. Motivation.....	13
2. Theoretical Background.....	15
2.1. Density Functional Theory (DFT).....	15
2.2. Nudged Elastic Band (NEB) Method.....	20
3. Computational Modeling and Results.....	23
3.1. Surface Slab Setup.....	23
3.1.1. Ni (111) surface.....	23
3.1.2. Ni-Cr alloy.....	25
3.2. DFT computational details.....	34
3.3. Lattice Constant for Ni, Cr and Ni Cr Alloy.....	36
3.3.1. Ni.....	36
3.3.2. Cr.....	36
3.3.3. NiCr Alloy.....	37

TABLE OF CONTENTS (Continued)

	<u>Page</u>
3.3.3.1. Ni ₅ Cr ₅	37
3.3.3.2. Ni _{8.33} Cr _{1.67}	37
3.4. Adsorption models.....	38
3.4.1. Adsorption on Ni (111).....	38
3.4.1.1. CO ₂ adsorption.....	38
3.4.1.2. CO adsorption.....	43
3.4.1.3. O adsorption.....	45
3.4.1.4. C adsorption.....	46
3.4.1.5. CO and O co-adsorption.....	48
3.4.1.6. C and O co-adsorption.....	50
3.4.2. Adsorption on NiCr alloy.....	51
3.4.2.1. Ni _{8.33} Cr _{1.67}	51
3.4.2.1.1. CO ₂ adsorption.....	51
3.4.2.1.2. CO adsorption.....	53
3.4.2.1.3. O adsorption.....	54
3.4.2.1.4. C adsorption.....	55
3.4.2.1.5. CO and O co-adsorption.....	56
3.4.2.1.6. C and O co-adsorption.....	57
3.4.2.2. Ni ₅ Cr ₅	59
3.4.2.2.1. CO ₂ adsorption.....	59
3.4.2.2.2. CO adsorption.....	61

TABLE OF CONTENTS (Continued)

	<u>Page</u>
3.4.2.2.3. O adsorption.....	62
3.4.2.2.4. C adsorption.....	62
3.4.2.2.5. CO and O co-adsorption.....	63
3.4.2.2.6. C and O co-adsorption.....	64
3.5. Nudged Elastic Band (NEB) calculation.....	65
3.5.1. CO ₂ activation and dissociation on Ni (111).....	65
3.5.1.1. CO ₂ activation.....	65
3.5.1.2. $\text{CO}_2^{\delta-} \rightleftharpoons \text{CO} + \text{O}$	66
3.5.1.3. $\text{CO} \rightleftharpoons \text{C} + \text{O}$	67
3.5.1.4. Overall reaction mechanism of CO ₂ dissociation on Ni(111).....	68
3.5.2. CO ₂ dissociation on Ni _{8.33} Cr _{1.67}	69
3.5.2.1. $\text{CO}_2^{\delta-} \rightleftharpoons \text{CO} + \text{O}$	69
3.5.2.2. $\text{CO} \rightleftharpoons \text{C} + \text{O}$	69
3.5.2.3. Overall reaction mechanism of CO ₂ dissociation on Ni _{8.33} Cr _{1.67} Alloy.....	70
3.5.3. CO ₂ dissociation on Ni ₅ Cr ₅	71
3.5.3.1. $\text{CO}_2 \rightleftharpoons \text{CO} + \text{O}$	71
3.5.4. Overall minima energy path for CO ₂ dissociation on Ni(111), Ni _{8.33} Cr _{1.67} and Ni ₅ Cr ₅	72
4. Conclusion and Recommendations for Future Work.....	73
References.....	76
Appendix.....	83

LIST OF FIGURES

<u>Figure</u>	<u>Page</u>
1.1. Phase Diagram of CO ₂	2
1.2. Simplified Diagram for the Principles of Power Conversion Cycle with Sc-CO ₂ as Working Fluid.....	4
1.3. Simplified diagram of steam Rankine Cycle.....	5
1.4. Simplified diagram of heated supercritical CO ₂ Brayton Cycle.....	5
1.5. Ni-Cr phase diagrams according to mole fraction of Ni.....	12
1.6. Crystal Structure for Ni ₃ Cr.....	13
2.1. Illustration of density functional theory.....	17
2.2. Illustration of the theory in NEB calculation.....	21
2.3. Minima Energy path for O atom diffuse from hcp site to fcc site on Ni (111) surface...22	
3.1. Relaxed Ni (111) surface.....	24
3.2. Four adsorption site on a Ni (111) surface.....	25
3.3. Schematic of Ni _{9.4} Cr _{0.6} , Ni _{8.8} Cr _{1.2} and Ni _{7.5} Cr _{2.5}	26
3.4. 2x2x4 Ni-Cr (111) alloy surface with four Ni atoms replaced by Cr atoms in each layer based on models.....	27
3.5. Schematics of type L1 ₀ crystal structure of Ni ₅ Cr ₅ alloy.....	28
3.6. Schematics of the most stable bulk crystal structure of Ni _{6.7} Cr _{3.3} alloy.....	29
3.7. Schematics of type DO ₆₀ bulk crystal structure of Ni _{7.5} Cr _{2.5} alloy.....	29
3.8. Schemitic of type D1 _a bulk crystal structure of Ni ₈ Cr ₂ alloy.....	30
3.9. Schemitic of L1 ₂ bulk crystal structure of Ni _{7.5} Cr _{2.5} alloy.....	31
3.10. Schematics of Ni ₅ Cr ₅ alloy.....	32

LIST OF FIGURES (Continued)

<u>Figure</u>	<u>Page</u>
3.11. Schematics of Model II-a, the $L1_0$ structure after relaxed volume.....	33
3.12. Schematics of nine adsorption sites on Ni_5Cr_5 (111) alloy surface.....	34
3.13. Schematic of CO_2 activation process before dissociation.....	40
3.14. Physisorption of CO_2 on Ni (111) surface.....	41
3.15. Four adsorption configurations for CO_2 activated state on Ni (111).....	42
3.16. Four adsorption models for CO chemisorption on Ni (111).....	45
3.17. Four adsorption models for O chemisorption on Ni (111).....	46
3.18. Four adsorption models for C chemisorption on Ni (111).....	47
3.19. Available adsorption sites on Ni (2x2) surface for CO and O co-adsorption.....	48
3.20. Adsorption model for CO and O co-adsorption on Ni (111).....	49
3.21. Adsorption model for C and O co-adsorption on Ni (111).....	50
3.22. Four adsorption models for CO_2 activated state on $Ni_{8.33}Cr_{1.67}$ alloy.....	52
3.23. Adsorption for CO on $Ni_{8.33}Cr_{1.67}$	53
3.24. Four adsorption models for O adsorption on $Ni_{8.33}Cr_{1.67}$ alloy.....	55
3.25. Four adsorption models for C adsorption on $Ni_{8.33}Cr_{1.67}$ alloy.....	56
3.26. Adsorption model for CO and O co-adsorption on $Ni_{8.33}Cr_{1.67}$	57
3.27. Adsorption model for C and O co-adsorption on $Ni_{8.33}Cr_{1.67}$	58
3.28. Configuration of CO_2 physisorption on Ni_5Cr_5 surface.....	59
3.29. Activated state of CO_2 on Ni_5Cr_5 surface.....	60
3.30. The most stable adsorption site for CO adsorption on Ni_5Cr_5 surface.....	61
3.31. The most stable adsorption site for O adsorption on Ni_5Cr_5 surface.....	62

LIST OF FIGURES (Continued)

<u>Figure</u>	<u>Page</u>
3.32. The most stable adsorption site for C on Ni ₅ Cr ₅ surface.....	63
3.33. Adsorption model for CO and O co-adsorption on Ni ₅ Cr ₅	63
3.34. Adsorption model for C and O co-adsorption on Ni ₅ Cr ₅	64
3.35. Diagram of the reaction energy of the CO ₂ direct dissociation.....	66
3.36. Diagram of the reaction energy of the CO ₂ direct dissociation.....	67
3.37. Diagram of the reaction energy of the CO dissociation.....	67
3.38. Diagram of the reaction energy of the overall reaction mechanism of CO ₂ dissociation on Ni (111).....	68
3.39. Diagram of the reaction energy of the CO ₂ ^{δ-} direct dissociation on Ni _{8.33} Cr _{1.67} alloy surface.....	69
3.40. Diagram of the reaction energy of the CO dissociation on Ni _{8.33} Cr _{1.67} alloy surface.....	70
3.41. Diagram of the reaction energy of the overall reaction mechanism of CO ₂ dissociation on Ni _{8.33} Cr _{1.67} alloy.....	71
3.42. Diagram of the reaction energy of the CO ₂ ^{δ-} direct dissociation on Ni ₅ Cr ₅ alloy surface.....	72
3.43. Diagram of the overall minima energy path for CO ₂ dissociation on Ni(111), Ni _{8.33} Cr _{1.67} and Ni ₅ Cr ₅	73

LIST OF TABLES

<u>Table</u>	<u>Page</u>
1.1. Main compositions of four types of alloys in % mass fraction.....	7
1.2. Main composition of three types of Ni based alloys in % mass fraction.....	8
1.3. Alloys with their highest operation temperature.....	9
3.1. The lattice constant of Model I to IV of Ni ₅ Cr ₅ alloy.....	35
3.2. The adsorption energy of CO ₂ , CO, CO+O and C+O adsorption on Ni (111) surface for different number of K-points.....	35
3.3. Calculated lattice constant and reference data for fcc-Ni, bcc-Ni, bcc-Cr and fcc-Cr.....	35
3.4. Calculated lattice constant and reference data for fcc-Ni, bcc-Ni, bcc-Cr and fcc-Cr.....	37
3.5. Adsorption energy and bond length for CO ₂ in physisorption and activated state on Ni (111) surface.....	42
3.6. Adsorption energy and bond length for CO ₂ in activated state on Ni (111) surface.....	44
3.7. O adsorption energy and lattice parameter on Ni (111).....	46
3.8. C adsorption energy and bond length on Ni (111).....	47
3.9. Adsorption energy and bond length for CO ₂ activated state on Ni _{8.33} Cr _{1.67} alloy.....	52
3.10. Adsorption energy and bond length for CO chemisorption on Ni _{8.33} Cr _{1.67}	53
3.11. O adsorption energy and bond length on Ni _{8.33} Cr _{1.67}	54
3.12. C adsorption energy and bond length on Ni _{8.33} Cr _{1.67}	56
3.13. Adsorption energy and bond length for CO ₂ activated state on Ni ₅ Cr ₅ alloy.....	60
A1. Total energy of all adsorbates, surfaces and adsorption models.....	83
A2. Structural parameters for all adsorption models studied.....	84

1. Introduction

Humankind has been seeking to improve chemical and economical process efficiencies, chemical safety and durability of chemical processes since the establishment of chemical industry. Three types of fossil fuel: coal, petroleum and natural gas have been the main fuel sources for electricity generation in the last few decades [1-4]. They have brought improved quality of life but also exhaust emission such as sulfur oxides, nitric oxide and carbon monoxide. Air quality has been greatly affected leading to serious social issues. One of the broadly applied alternative methods in electricity generating is nuclear power. But the conventional nuclear power plant is less thermal efficient than fossil fuel power plant in working cycle because of the low operation temperature of conventional nuclear power plant [4]. Supercritical fluids have attracted more and more researchers' attention as an alternative thermal fluid with its unique properties and possibly wide fields of applications. Replacing traditional working fluid with supercritical working fluid in conventional fossil power plant can improve the operational temperature making them more thermally efficient, up to 5% compared to steam Rankine Cycle [1, 4]. Nuclear power plants operated with supercritical fluids will be more efficient than conventional power plants with higher operational temperature power cycles [1, 2] this is one of many reasons why studies focusing on supercritical fluids have become a hot topic in material science.

Supercritical fluids are fluids above the supercritical points where there is no liquid-gas phase boundary in the system [1, 2]. This unique status gives supercritical fluids combined properties of both liquid and gas with corresponding high density, low viscosity and no surface tension. Supercritical fluids show excellent properties in liquid mobility and mass transfer.

Supercritical carbon dioxide (Sc-CO₂) is probably one of the most popular supercritical fluids that are employed in various applications food industries, manufacturing industries and nuclear industries [2].

1.1. Supercritical carbon dioxide (Sc-CO₂) and its properties

The phase diagram for CO₂ is shown in Figure 1.1. The supercritical point for CO₂ is 31.1 °C and 7.38MPa [1, 2].

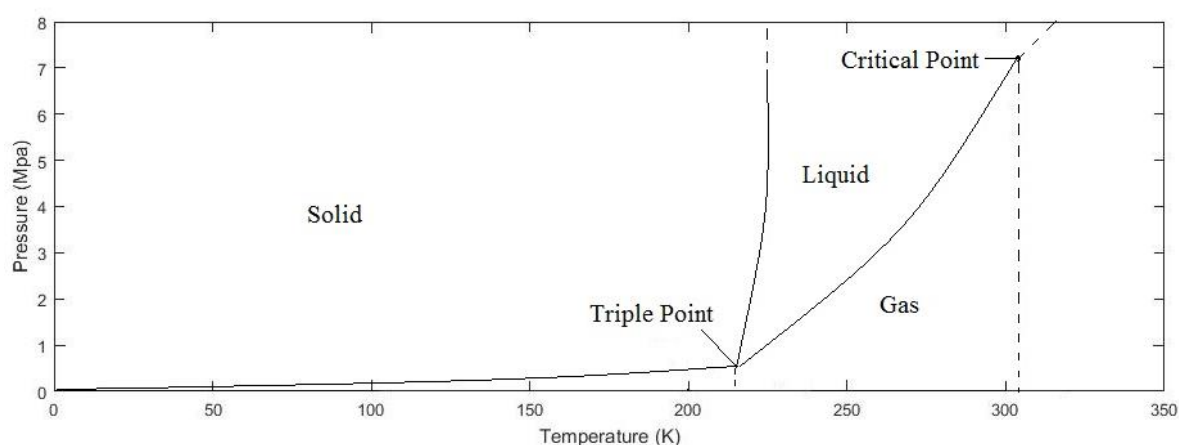


Figure 1.1 Phase Diagram of CO₂. CO₂ that is above the critical point is Sc-CO₂. At that state, there is no liquid-gas phase boundary.

CO₂ that is above the critical points will act as a transparent fluid. CO₂ is considered a greenhouse but compared to many of the volatile organic compounds (VOCs) often used as cooling fluids, it is still less harmful to the environment and more importantly, CO₂ is nonflammable, which enhances the safety index of the factory. Sc-CO₂, as a solvent, causes less contamination of the reactant and products and leaves less residue after the products extraction process compare to conventional solvents simplifying separations and cleaning of effluents [1]. This makes Sc-CO₂ a perfect solvent for non-polar compounds with low molecular weight [1]. CO₂ is also quite cheap, easy to synthesize and store.

1.2. Applications of Sc-CO₂

Sc-CO₂ is an ideal substitution solvent for several of industries. At low temperature, typically below 150 °C, Sc-CO₂ can be utilized as an alternative solvent for water in the dyeing process. With its low viscosity and high diffusion rate, Sc-CO₂ as a dyeing solvent in dry dyeing process can obtain better penetration into the material than water and also avoid highly contaminated waste [3]. Therefore, the efficiency of dyeing is increased and the environment is also better protected by the application. Sc-CO₂ has also been widely employed in food industries. For instance, it can be applied in the decaffeination process from raw materials of coffee or tea. Several studies have shown that Sc-CO₂ can extract hops or oils from plant materials [3]. Aiming to reduce CO₂ releasing rate from fossil burning and other industrial processes, Sc-CO₂ can be used as CO₂ capture and storage in fossil fuel plants as a substituted absorber [2, 4] that may effectively reduce the emission of greenhouse gases in the plant. Some studies also indicate that Sc-CO₂ has a great potential application in chemical synthesis, polymer production and processing, as well as in semiconductor and powder production [1].

The applications of CO₂ at low temperature are well studied [1, 2] while higher temperature applications have drawn more recent interests [2, 4]. At high temperature, generally over 400 °C, Sc-CO₂ has a broader prospect in energy industries. As a working fluid, Sc-CO₂ shows great properties in power generating turbines [2]. The principles behind applying Sc-CO₂ into power conversion cycle are shown in Figure 1.2.

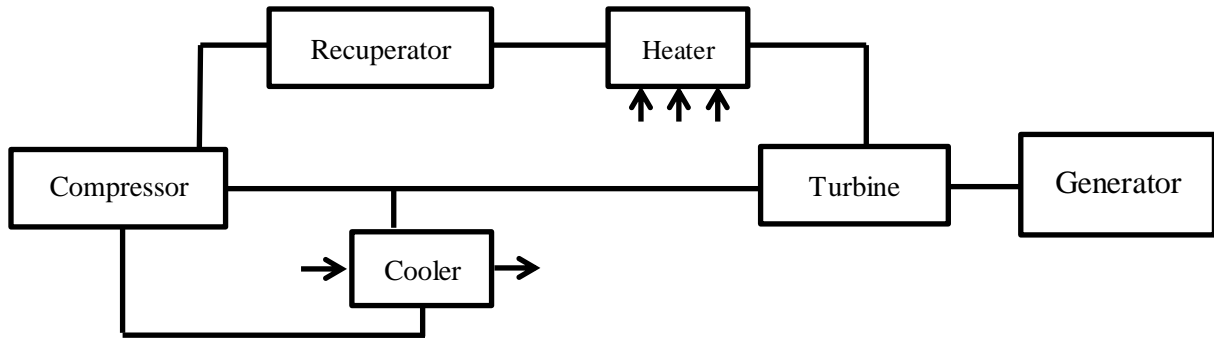


Figure 1.2 Simplified diagram of the principles of power conversion cycle with Sc-CO₂ as working fluid.

Utilizing Sc-CO₂ in the reaction system in fossil fuel power plants will significantly increase its thermal efficiency. Some plants operators and vendors in California, US and Paris, France have already started to employ this technology into their processes, such as Pratt Whitney & Rocketdyne and Electricite De France [4].

Sc-CO₂ fluid attracts more and more interest from researchers for its application in power conversion systems [4]. Power cycle based on Sc-CO₂ could potentially replace the conventional steam Rankine cycle (steam turbine) and air Brayton cycle (gas turbine system) as Sc-CO₂ power cycle can operate at higher temperature and also enhance the safety and reliability of the system [4]. For conventional water-steam cooled nuclear plant, mainly with steam Rankine Cycle shown in Figure 1.3, the operation temperature is as low as 300 °C [4].

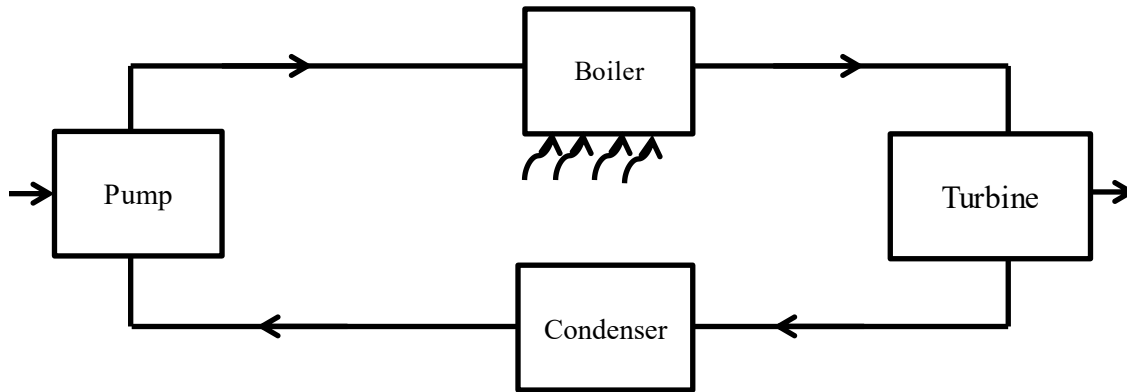


Figure 1.3 Simplified diagram of steam Rankine Cycle.

The conventional water-steam cooled nuclear plant is limited by the low thermal efficiency compared to common power plant using fossil energy, mainly gas turbine system [2, 4]. If Sc-CO₂ were to replace water and utilized in Sc-CO₂ Brayton cycle in nuclear power plant, as shown in Figure 1.4, the operation temperature can be increased to above 500 °C which would finally lead to higher net thermal efficiency for nuclear power plant, greater than 50% [1, 4].

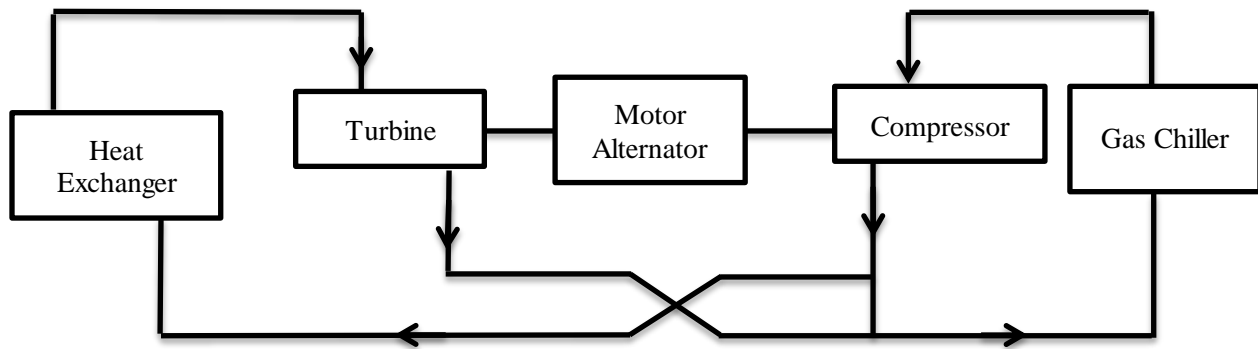


Figure 1.4 Simplified diagram of heated supercritical CO₂ Brayton Cycle.

Sc-CO₂ Brayton cycle takes advantages of both steam Rankine cycle and gas turbine system. Implementation of the Sc-CO₂ Brayton cycle also reduces the size of the

turbomachinery; therefore, the overall facilities size for the power cycle system can be four times smaller than conventional nuclear plant [4]. The residue of CO_2 is low at the operating pressure so purification facilities for the system will not be as complicated as in the traditional plant. It is also ideal for use since CO_2 is a more inert, more reliable and less contaminant media compare to other transfer media [2-5].

1.3. Corrosion issue caused by Sc- CO_2

With the development of applications which depend on Sc- CO_2 , one significant factor that may affect its future implementation is corrosion issue. Over three percent of the Gross Domestic Product (GDP) is wasted on corrosion among all industrial countries each year [2]. Serious corrosion leads to not only the increase of facility cost but is also a potential safety hazard. Similar to other types of fluids, Sc- CO_2 also causes corrosion and aging problems. Since Sc- CO_2 creates a new environment, conventional corrosion resistant material possibly fail to provide similar corrosion/aging resistance as in air. The difference between well-known oxidized corrosion that occurs in air or water is that in Sc- CO_2 environment, high temperature carburization is another corrosion/aging mechanism that may cause localized corrosion or aging [2]. That is also called environment-assisted cracking (EAC). Previous studies have focused on material corrosion performance in Sc- CO_2 for oxidation and carburization and often focus on common industrial material, such as stainless steel, mild steels, aluminum base alloys and Ni base alloys [2].

Experimental analysis based on steels is more complete than on other metals since steel is usually considered the main material for structures and facilities. F. Rouillard, F. Charton and G. Moine discuss four types of steels corrosion in Sc- CO_2 environment: T91, 316L, 253MA and

Alloy 800 [6]. These four types of alloys largely differ by their content of Ni and Cr, as shown in Table 1.1.

Table 1.1 Main compositions of four types of alloys in weight %.

	T91	316L	253MA	Alloy 800
Fe	Balance	Balance	Balance	Balance
Cr	8.63	17.4	20.75	19.95
Ni	0.23	11.1	10.97	30.9
C	0.1	0.02	0.089	0.04
Mn	0.43	1.39	0.5	0.71
Si	0.31	0.63	1.61	0.39
Mo	0.95	2.05	0.33	--
Ti	0.003	--	--	0.46
N	0.03	0.064	0.157	--
S	0.006	0.001	0.001	0.004
P	0.02	0.032	0.02	--
Cu	0.046	--	0.11	0.08

Based on the mass gain and Glow Discharge Optical Emission Spectroscopy (GDOES) analysis of all samples, the authors found that the enrichment of Ni and Cr in the alloy significantly increases the corrosion resistance of the material. One another observation from the GDOES analysis of the four samples shows that for the outer oxide layer, Cr has the highest intensity while Fe has relative low intensity indicating that the outer oxide layer is enriched by Cr [6]. Furthermore, Field Emission Scanning Electron Microscope (FESEM) analysis shows that for T91, which contains less than 9wt% Cr, exhibits porous Cr-rich outer oxide layer where according to GDOES analysis C has diffused to deeper layers; however, 316L, 253MA and Alloys 800 exhibit a dense surface oxide layer [6]. They found that at least 17wt% of Cr in the alloy is needed for it to perform better and prevent the material from Sc-CO₂ corrosion. This is in

good agreement with other studies of the minimal Cr ratio in Ni-Cr alloy required for good corrosion resistance [3].

Similar conclusion regarding high Cr ratio in alloys for improved corrosion resistance, is obtained by Firouzdor et al. in their high temperature corrosion experiment (20 MPa CO₂, 650 °C for 500h, 1000h, and 3000h) [7] and Pint et al. in their wide temperature range experiment (20 MPa CO₂, up to 750 °C for 500h) on alloys [5]. Other potential corrosion factors of metal interface elements are through carbide formation but carburization depassivates the oxide layer covering the bulk metal [5, 7]. Firouzdor et al. state that the protective passive layer for alloys mainly consists of Cr oxide in Sc-CO₂ environment [7]. Since Cr has an important role in corrosion prevention, three types of Ni-based alloys were investigated experimentally in the paper by Firouzdor et al.: PE16, Haynes 230 and Alloy 625. The composition of these three alloys is shown in the Table 1.2.

Table 1.2 Main components of three types of Ni-based alloys in weight %.

	PE16	Haynes 230	Alloy 625
Ni	43.8	52.7	57.9
Fe	33.6	3	5
Cr	16.7	22	21.5
Mo	3.4	2	9
Co	--	5	1
W	--	14	--
Mn	0.13	0.5	0.5
Si	0.2	0.4	0.5
Al	1.1	0.3	0.4
Ti	1	--	0.4
Cb+Ta	--	--	3.7

X-ray Diffraction (XRD) and X-ray Photoelectron Spectroscopy (XPS) analysis reveals that the oxide layer is Cr-rich and the main component of the layer is Cr_2O_3 [7]. Besides Cr_2O_3 , other minor metal oxides were found on the surface. XRD shows that the oxide layer on PE16 also contains $\text{Cr}_{1.4}\text{Fe}_{0.7}\text{O}_3$ and NiCr_2O_3 phase while the oxide layer on Haynes 230 contains a NiCr_2O_4 phase [7]. Experiments conducted by Pint et al. came to a similar conclusion and further stated that the impurities, such as O_2 and H_2O , have little effect on the carburization compare to CO_2 on alloy surface at long exposure times [5].

Sarrade et al. summarized previous experimental data and obtain a maximum operating temperature for various alloys under Sc- CO_2 condition [2] as shown in Table 1.3.

Table 1.3 Alloys and their highest operation temperature.

Alloy type	Mild Steel	9Cr -steel	316H steel	NiCr alloy	Ni Aluminum alloy
Operation temperature	350 °C	450 °C	650 °C	650 °C -750 °C	>750 °C

According to their conclusion, Ni-based alloy is the only alloy that shows great corrosion resistance in Sc- CO_2 environment at high temperature. For Ni-Cr alloys, above 650 °C, the formation of Cr oxide protects the alloy from corrosion. The oxide passive layer forms easily and can resist the carburization better than that on steel. When operating temperature is above 750 °C, Ni-aluminum alloys can be ideal candidates for corrosion resistant material [2].

1.4 Carburization corrosion mechanism

The mechanism of carburization is of fundamental importance when designing corrosion resistance materials in Sc- CO_2 environment. Carburization is the formation of metal carbides when the material is exposed to carbon environment [6-9]. For pure metal in Sc- CO_2 environment, Sc- CO_2 is the only source of carbon so the carbon that forms carbides can only

come from Sc-CO₂. The major source of carburization and the formation of carbides are initiated from the dissociation of CO₂ and carbon diffusion into the interface of the material.

Gheno et al. studied the carburization of ferritic Fe-based alloys containing Cr experimentally [8] and suggested the following reaction steps for CO₂ dissociation and metal carbide formation [8]:



The aggregation of Cr oxide for high Cr alloys, mainly Cr₂O₃, is also observed. The oxidation step for Cr is [8]



The first step, where CO₂ directly decomposes into CO and O, is also acknowledged by other authors [9-14].

As specifically described in these papers, elementary steps of CO₂ dissociation to CO and O on metal or alloy surfaces can be separated into two processes:

Adsorption for CO₂ on the surface:

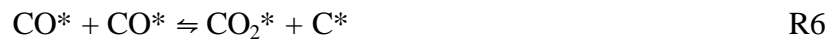


CO₂ dissociation to CO and O:



whereas * stands for adsorption sites.

Elementary step for CO dissociation is



The other possible step mentioned in the literature is the direct dissociation of CO [12, 13, 15]:



There are limited studies investigating the CO₂ dissociation step on Ni and its alloys surface. The process is often referenced to studies of Water Gas shift (WGS) reaction on Ni surface. Catapan et al. studied reactions R5-R7 using density functional theory (DFT) as a part of their research on WGS and Coke formation on a Ni surface. Activation energy for these two steps is compared and they concluded that the activation energy for R6 is higher than R7 on Ni surface [12]. Blaylock et al. came to a similar conclusion that CO dissociation always follows R7 reaction route to form C and O rather than R6 on Ni surface [13] and other studies also came to the identical conclusion [15, 16].

1.5 Ni and Ni-based alloys

Ni has a face-centered cubic (fcc) crystal structure in its solid phase. Unlike cobalt, fcc structure is the only stable crystal structure for Ni below its melting point (1455 °C). Therefore, Ni maintains an fcc crystal lattice structure during the CO₂ dissociation process at all temperatures below its melting point.

Ni-based alloys will basically keep its fcc structure but their properties vary with the alloying element [2, 7, 17-26]. Zhang et al. investigated the behavior of Ni-iron and Ni-copper alloy in CO₂ environment [17]. Compared to the Ni (111) surface, Ni-iron alloy will increase the adsorption ability of carbon and oxygen while alloying with copper weakens it [17]. Also, Ni-iron is not favorable for decarburization while Ni-copper alloy is favorable [17]. They also state that by greatly decreasing carbon deposition the Ni-copper alloy has a good carbon resistance at room temperature [17]. Ni-cobalt alloy is other well studied alloy. Liu et al. stated that Ni-cobalt alloy coating has an excellent wear and corrosion resistance to oxidation in air environment when the coating is produced by electro-deposition in Sc-CO₂ environment [18]. During the processing of the coating, Sc-CO₂ corroded the surface so that the surface was brighter and less

rough indicating that Ni-cobalt alloy is not an ideal candidate for high temperature Sc-CO₂ corrosion resistance [18].

For Ni alloy properties in high temperature Sc-CO₂ Ni-Cr alloy is an ideal candidate among alloys that they were studied according to Sarrade et al. and Das et al. [2, 19], because of the excellent resistance to carburization of Cr in steels and other types of alloys at high temperature. Das et al. conclude that a quite strong bond formed between Cr and oxygen and the bond distance between these two atoms is small, which can be considered as the initial state of protective Cr oxide layer [19]. Kumar et al. studies, based on Alloy 800 with quantum molecular dynamics approach, also supports that point that the Cr component will aggregate to the surface when the surface is exposed to water [20].

Previous studies have shown that at least 17% of Cr is essential for corrosion resistance [6, 7]. Therefore, Ni-Cr alloy in this study is designed with the Cr content of nearly 20%. Since Cr has a body-centered cubic (bcc) crystal structure, according to the Ni-Cr phase diagram shown as Figure 1.5, two possible crystal structures exists for Ni-Cr alloy.

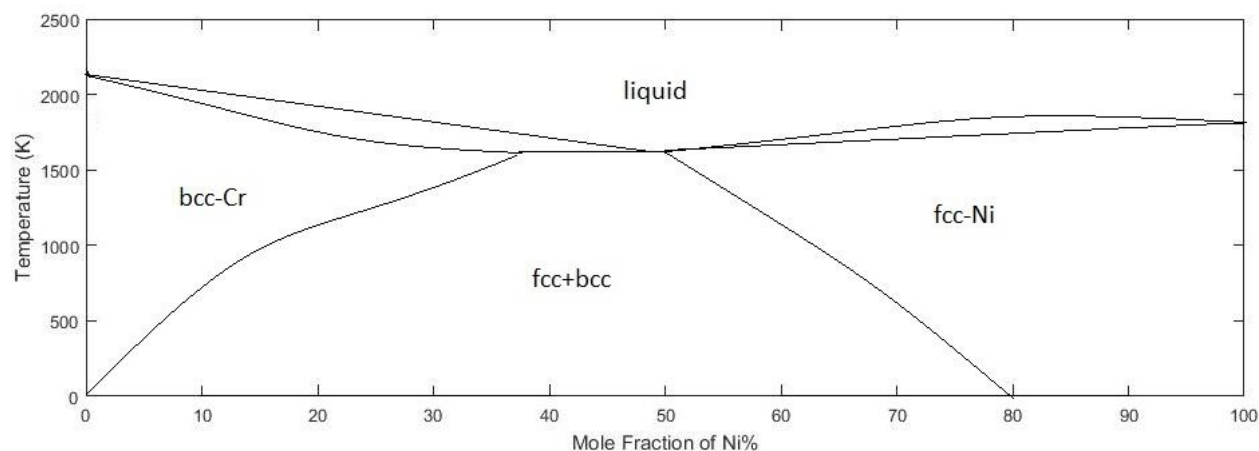


Figure 1.5 Ni-Cr phase diagrams according to mole fraction of Ni.

At nuclear power plant operation temperatures, around 700°C -1000°C, fcc structure is the main structure of the Ni-rich alloy [23-26]. This is consistent with Breidi et al. studies on energetic modeling of Ni-Cr alloy and Petrović et al. investigation on Ni-Cr thin film characterization [21, 22]. Rahaman et al. investigated the possible proportion of Ni to Cr theoretically and indicate that $\text{Ni}_{6.66}\text{Cr}_{3.33}$, $\text{Ni}_{7.5}\text{Cr}_{2.5}$, Ni_8Cr_2 , $\text{Ni}_{8.33}\text{Cr}_{1.67}$ and Ni_9Cr are several possible selections for the Ni-Cr alloy [23]. Similar conclusions is also reached in other studies [2, 7, 17-22, 24, 25]. Furthermore, Connétable et al. discussed the possible structures for the Ni-Cr alloy based on theoretical calculation. They state that alloy type $\text{X}_3\text{Y-L1}_2$, similar to Cu_3Au alloy, is the only stable structure for the $\text{Ni}_{7.5}\text{Cr}_{2.5}$ [26], that structure is shown in Figure 1.6.

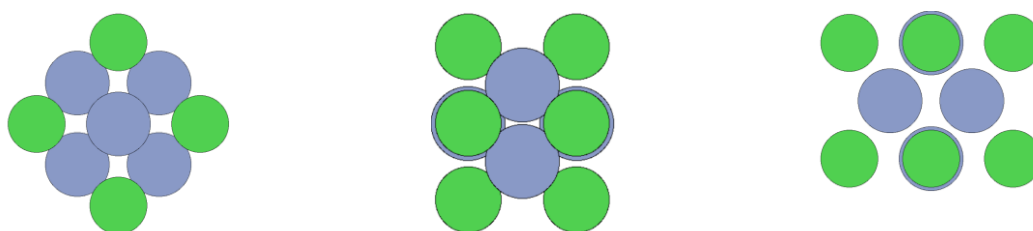


Figure 1.6 Crystal Structure for Ni_3Cr , z-y-x view. Ni atoms are shown in green and Cr atoms in grey.

They calculated the formation energy for the alloy to be -0.038 kJ/mol with the lattice constant of 3.565 Å [26]. As for the atomic order, Rahaman et al. and Zhang et al. obtained that the atomic order for Ni-chromium alloy to be random [23, 24].

1.6 Motivation

To date experiments have indicated some common commercial alloy, such as 9Cr-1Mo steel, 316H steel, Alloy 625 and Alloy 690, which shows great potential in corrosion resistance under specific conditions; however, as Sarrade et al. pointed out, only arbitrary conclusions can

be obtained for a specific alloy owning great resistance in a specific temperature range [2]. Only Ni-based alloys showed great resistance at operating temperatures over 650 °C. Also, Sarrade et al. suggested that Ni-Cr and Ni-Al are two ideal candidates at this temperature range [2].

Experimental characterizations including XRD, XPS and GDOES have been conducted on corrosion resistance providing some intuitive insights such as the composition of the passive layer. The corrosion resistance of three types of commercially available Ni-based alloys, PE16, Haynes 230 and Alloy 625 have previously been studied experimentally [7]. These alloys have similar Ni and Cr ratios, Ni_7Cr_3 . The ratio of Ni to Cr for Ni-based alloy where the crystal structure still follows fcc structure ranges from Ni_5Cr_5 to Ni_9Cr . Experiments based on these common materials gives great insight into corrosion resistance of these alloys but fail to cover different ratios of alloying elements. Experimental studies of different alloying ratios are expensive and time consuming, computational methods can be fast and affordable and provide complimentary information of the system, in particular electron structure calculations can provide insights into atomic interactions and details of the reaction kinetics and potential energy surface of the system.

To the best of the author's knowledge, detailed information about the mechanism of the corrosion process for metals or alloys in Sc-CO_2 environment have not yet been determined. Using theoretical approach, we can determine the reaction mechanism and study the effects of different alloying ratios on the corrosion resistance. The calculation process is based on highly simplified systems, which can help decouple the different components of a complex reactions included in corrosion. Although it might fail to represent the macroscopic corrosion phenomenon, theoretical results provide an insight into the microscopic processes such as reaction kinetics, ligand and coverage effects. Theoretical calculation also save time and are

relatively inexpensive. Hence, the overall objective of this study is to investigate Ni and its alloy's performance in Sc-CO₂ environments theoretically method based on DFT, and determines alloys that have higher resistance to carburization in Sc-CO₂.

2 Theoretical Background

2.1 Density Functional Theory (DFT)

Everything in the world, no matter their size, shape, phase or mass, are composed of atoms and molecules. Therefore, it is atoms and molecules that control the properties of matter and understanding their interaction is fundamental for the progress in science and technology. DFT method [27, 28] is a theoretical approach that focuses on the atomic and electron structure that allows humankind to study not only the intrinsic properties but also series of more complicated physical and chemical processes. DFT calculations have attracted more and more attention in the last few years with its reliable results, progress in cluster computing has made it possible to study more complex systems at low cost compared to conventional experimental method [27-32].

In order to understand properties of matter, which is a collection of atoms, the fundamental thing that needs to be studied is the formation energy of a substance [27]. In order to understand the chemical or physical properties of a material, the corresponding position of atoms, as well as the position of their nucleus and electron, also needs to be studied [27]. Calculating the energy and position of atoms can be divided into solving those for electrons and nucleus separately. This is known as the Born-Oppenheimer approximation [29]. The lowest energy state, the ground state of electrons, is described through the approximation of a set of electrons moving as a function of set of nuclei [27]. This is known as adiabatic potential energy surface [27, 28]. Hence, it is the difference in ground-state energy between two matters that

make them differ from each other. Since the ground-state energy is time independence, the simplified form of Schrödinger equation, as shown in Eq. 2.1, is applied in the calculation [27, 28].

$$H\psi = E\psi \quad \text{Eq. 2.1}$$

Where H is the Hamiltonian operator, ψ is set of solutions, or eigenstates, of the Hamiltonian, E is the energy of the state ψ . The Hamiltonian operator in Eq. 2.1 for a collection of electrons can be written as series of interaction energies, shown in Eq. 2.2 [27]:

$$\left[\frac{\hbar^2}{2m} \sum_{i=1}^N \nabla_i^2 + \sum_{i=1}^N V(r_i) + \sum_{i=1}^N \sum_{j < i} U(r_i, r_j) \right] \psi = E\psi \quad \text{Eq. 2.2}$$

Where m is the mass of the electron, the three terms in the bracket represent the kinetic energy of the electron, the interaction between the electron and the nuclei and the interaction between two electrons. E is the ground state energy of all electrons in the system and ψ is the electronic wave function [27, 28]. The wave function, ψ , can be approximately expanded as Hartree product, Eq. 2.3 [27].

$$\psi = \psi_1(r) \psi_2(r) \dots \psi_N(r) \quad \text{Eq. 2.3}$$

Based on the Schrödinger equation, Kohn and Hohenberg came up with two mathematical theorems that are seen as the foundation of DFT [27, 28].

Theorem 1: “The ground-state energy from Schrödinger’s equation is a unique functional of the electron density.”

Theorem 2: “The electron density that minimizes the energy of the overall functional is the true electron density corresponding to the full solution of the Schrödinger equation.”

Theorem 1 indicates that the ground-state energy and ground state electron density has function-like correlation. Therefore, the properties of a substance can be determined by ground-state electron density. With this correlation, the dimension of Schrödinger equation is simplified

from $3N$ to 3, as Figure 2.1 shows. Moreover, the ground state energy is the solution of Schrödinger equation.

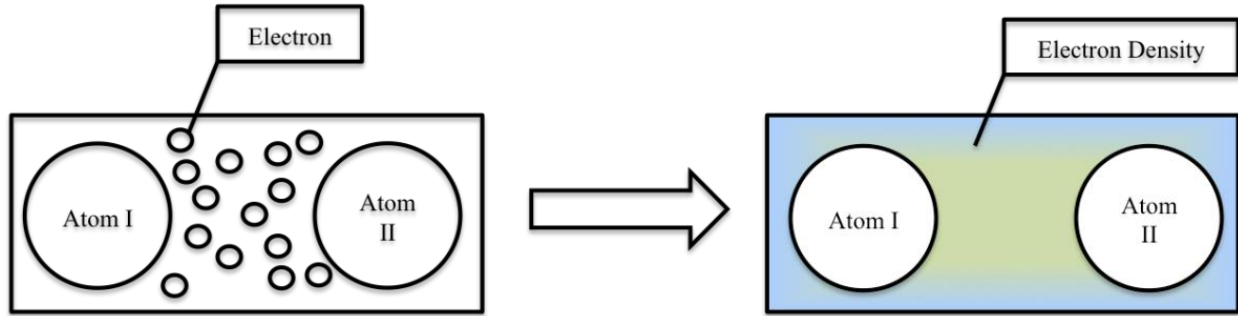


Figure 2.1 Illustration of DFT. Determining the ground-state electron density instead, the dimension of Schrödinger's equation can be simplified from $3N$ to 3.

Theorem 2 is the compensation on the basis of Theorem 1 with the additional description of the functional. The theorem indicates that the electron density that minimizes the functional is the true electron density and corresponding to the solution of the Schrödinger's equation.

The functional in the two theorems can be described as wave functions for single electrons in Hartree products (Eq. 2.3), $\psi_i(\mathbf{r})$ [27]. Recalling electron density is function of $\psi_i(\mathbf{r})$, Theorem 1 can be written as a function [27]:

$$E[\{\psi_i\}] = E_{\text{known}}[\{\psi_i\}] + E_{\text{XC}}[\{\psi_i\}] \quad \text{Eq. 2.4}$$

The first term, $E_{\text{known}}[\{\psi_i\}]$, describes interactions and kinematics of electrons. Its form is shown in Eq. 2.5 [27]:

$$E_{\text{known}}[\{\psi_i\}] = \frac{\hbar^2}{2m} \sum_i \psi_i^* \nabla^2 \psi_i d^3r + \int V(\mathbf{r}) n(\mathbf{r}) d^3r + \frac{e^2}{2} \iint \frac{n(\mathbf{r})n(\mathbf{r}')}{|\mathbf{r} - \mathbf{r}'|} d^3r d^3r' + E_{\text{ion}} \quad \text{Eq. 2.5}$$

The first term in Eq. 2.5 is the kinetic energies of electron; second is the Coulomb interactions between electrons and nuclei; third is the Coulomb interactions between two electrons and the last term is the Coulomb interaction between two nuclei [27].

In Eq. 2.4, the second term, $E_{XC} [\{\psi_i\}]$, is the exchange-correlation functional which defines all other mechanical effects excluded by $E_{\text{known}} [\{\psi_i\}]$. The difficulties in solving Eq. 2.4 are still huge. However, with Kohn-Sham equations [32], as shown in Eq. 2.6, $E_{\text{known}} [\{\psi_i\}]$ can be obtained.

$$\left[\frac{\hbar^2}{2m} \nabla^2 + V(r) + V_H(r) + V_{XC}(r) \right] \psi_i(r) = \varepsilon_i \psi_i(r) \quad \text{Eq. 2.6}$$

$V(r)$ is the potential describing the interaction between electron and nuclei [27, 32]. $V_H(r)$ is Hartree Potential that defines the Coulomb repulsion between electrons and overall electron density with the form in Eq. 2.7 [27, 32]:

$$V_H(r) = e^2 \int \frac{n(r')}{|r - r'|} d^3r' \quad \text{Eq. 2.7}$$

$V_{XC}(r)$ is the functional derivative of the exchange-correlation energy, as Eq. 2.8 shows [27, 32].

$$V_{XC}(r) = \frac{\delta E_{XC}(r)}{\delta n(r)} \quad \text{Eq. 2.8}$$

Having solved the $E_{\text{known}} [\{\psi_i\}]$ in Eq. 2.4, the other term, the exchange-correlation functional $E_{XC} [\{\psi_i\}]$, can be obtained using the uniform electron gas approximation for the whole system. In this case, the exchange-correlation potential can be written as the form in Eq. 2.9:

$$V_{XC}(r) = V_{XC}^{\text{electron gas}}[n(r)] \quad \text{Eq. 2.9}$$

The exchange-correlation energy can then be defined in the form Eq. 10:

$$E_{XC}^{\text{LDA}}(\psi) = \int r \psi(r) \varepsilon_{XC}(\psi) d^3 \quad \text{Eq. 2.10}$$

Then the approximation that defines the exchange-correlation functional is based only on the local density, the method is called local density approximation (LDA) [27, 33]. However, this approximation has limitations. For systems with slowly varying charge densities, LDA is quite

accurate. However, for systems that are strongly correlated, the independent particle pictures break down and LDA become less accurate. Based on LDA, generalized gradient approximation (GGA) [27, 34] was proposed with more physical information involved in the equation, as shown in Eq. 2.11.

$$E_{XC}^{GGA}(\psi) = \int r \psi(r) \epsilon_{XC}(\psi, \nabla) d^3 \quad \text{Eq. 2.11}$$

Therefore, the exchange-correlation functional considers the local electron density and the gradient in electron density, as Eq .2.12 shows.

$$V_{XC}^{GGA}(r) = V_{XC}[n(r), \nabla n(r)] \quad \text{Eq. 2.12}$$

This equation considers the spatial variation of the electron density, $\nabla n(r)$, so the approximation provides more flexibility while describing real material [27].

There are many nonempirical functional that can be applied in calculation to perform GGA two commonly used are: Perdew-Wang functional (PW91) [35] and Perdew-Burke-Ernzerhof functional (PBE) [36].

To solve those equations described above, thousands or hundreds of thousands of calculations are needed. The development of high performance computer provides an opportunity to accomplish this process. Vienna Ab initio Simulation Package (VASP) [3] is one of the widely applied software used for density functional theory calculations. VASP was initially written by Mike Payne in 1980s and it has been maintained and developed by Jürgen Hafner, Georg Kresse and Jürgen Furthmüller since 1989. The software is able to solve many-body Schrödinger equations using density functional theory (DFT). Using DFT as its basic methodology, it solves the Kohn-Sham equations (Eq. 2.6) using either the LDA or the GGAs approach [27, 33]. It can also calculate the forces and stress tensor for DFT, Hartree-Fock and

Hybrid functional. Also, it can also calculate the dynamics of a chemical or physical process. It can also be used to calculate magnetism, linear response to electric fields and ionic displacements. VASP extracts the needed pseudo potentials and electronic data from its database specified by user.

2.2 Nudged Elastic Band (NEB) Method

In section 2.1, one of the applications for VASP is to calculate the dynamics of a chemical or physical process. Nudged Elastic Band (NEB) Method [27, 38-40] is the approach used here to investigate the CO₂ dissociation. NEB method introduces a set of states, shown as a set of images in the calculations, and relaxes these states toward the minima energy path [27, 40]. Hence, an energy connection between two energy minima is established. NEB method is based on optimizing images of the reaction or diffusion path between the initial and final state to determine the potential energy system and the transition state. The optimization is done by projecting out the component of the force due to the potential perpendicular to the band and adding spring forces along the band between two images [27]. That is, NEB calculation applies a force projection scheme where the real forces works perpendicular to the band and the spring forces works parallel to the band. To obtain the image at the saddle point, in the calculation, the image tries to maximize the energy along the band and minimize that in all other directions [27, 31, 32]. After the force converges for each state, the saddle point is obtained, as shown in Figure 2.2 [27, 31]. Also, the other images on energy path find their lowest energy while maintaining equal space to adjacent images, as shown in Figure 2.2 [27, 31].

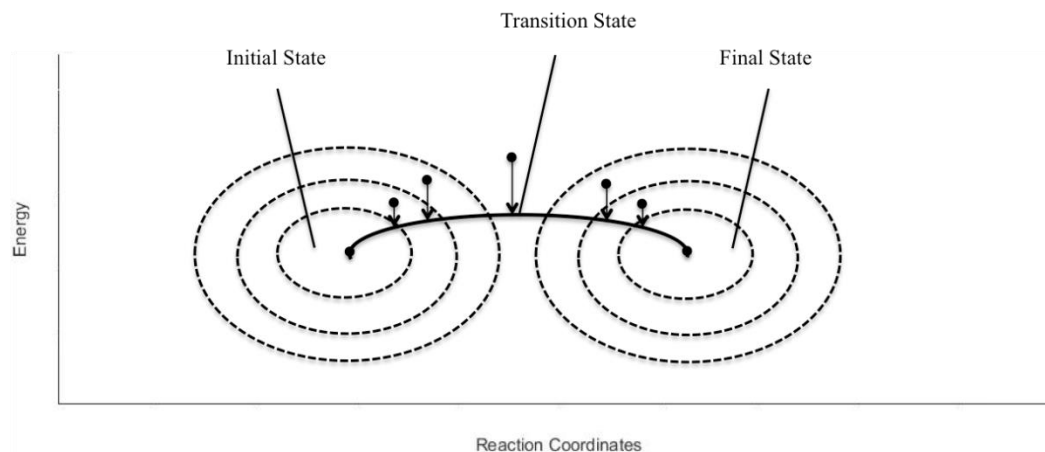


Figure 2.2 Illustration of the method behind NEB calculation. The black curve between the initial and final states is the minimized energy path for the process. The points above are the initial setting for the energy path. In NEB calculation, these points are converged and approach to the real minima energy path.

Based on the minimum energy path, we can obtain the following information about the process: the activation energy for both forward and reverse reaction, energy difference between initial and final states, and the position and nature of the transition state. For instance, Figure 2.3 shows the minimum energy path for the diffusion of an oxygen atom between different sites on a Ni surface.

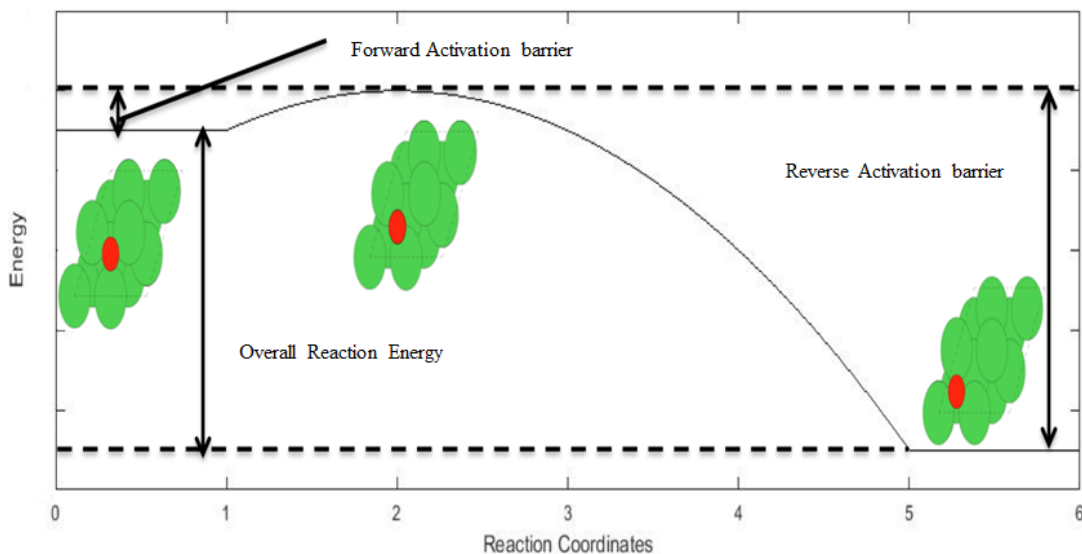


Figure 2.3 Minimum energy paths for O atom diffusing from a hcp site, over a bridge site to a fcc site on a Ni (111) surface

The energy path curve between the initial state and final state is obtained via NEB calculation [27]. Here the initial, final and transition states are identified and best linear fit is used between them, the line is here therefore is only a guide to the eye but not the real energy path. According to the figure, the difference between the initial and final state is the reaction energy and shows that this diffusion path is exothermic. The difference between the transition state and initial state is the forward activation barrier and that energy difference between the final state and transition state is the reverse activation barrier. From the value of energy difference between the initial and the final state, the thermodynamic of the process, endothermic or exothermic, can be obtained. For the process shown in Figure 2.3, the diffusion of an oxygen atom from hcp site to fcc site is exothermic. Also, comparison between forward and backward activation energy can provide information about the process. In this example, the fcc site is more stable for oxygen atom adsorption so the backward activation energy is higher than the forward

activation energy. Furthermore, for a process with multiple elementary steps, such as the synthesis of ammonia, comparing the activation energy between different steps can help determining the rate-limiting step for the whole process.

3. Computational Modeling and Results

3.1. Surface Slab Setup

Previous studies have shown that at high temperature, addition of Cr to Ni exhibits significant corrosion resistance in Sc-CO₂ environment [2, 5-9, 17-25, 41-43]. In this study, CO₂ direct dissociation process on Ni and Ni-Cr alloys surface is investigated theoretically using DFT calculations. Experiments have shown that Ni is fcc-structured metal and Cr is bcc-structured metal [10-15, 22-25, 39, 45-48, 55]. In this study, we first determine the lowest energy of Ni and Cr in different crystal structure to benchmark our approach. XRD characterization of Ni-Cr alloy showed that Ni (111) and Cr (110) facet have the highest intensity. CO₂ adsorption and dissociation on Ni (111) has been studied in details previously [10-14, 17, 19-26, 41-44]. Zhang et al. studied the different facets of fcc crystal structured metal and concluded that the (111) facet has the lowest surface energy comparing to other surface such as (100), (110) and (211) [45]. They also calculated the surface energy for bcc crystal structure and concluded that the (110) plane is the thermodynamically most stable surface among the Ni bcc closed packed surface structures [46-48]. In this study, CO₂ adsorption and dissociation is studied on Ni (111) and Cr (110) surfaces as well as on Ni-Cr alloys.

3.1.1. Ni (111) surface

A six layers slab is established with 5 Å vacuum space on each end leading to an overall 10 Å vacuum space between two slabs in z-direction a commonly applies vacuum space in DFT

calculations for metal slabs[10, 11, 13, 49-54]. The bottom two layers are fixed with the remaining four layers relaxed. The surface slab is shown in Figure 3.1.

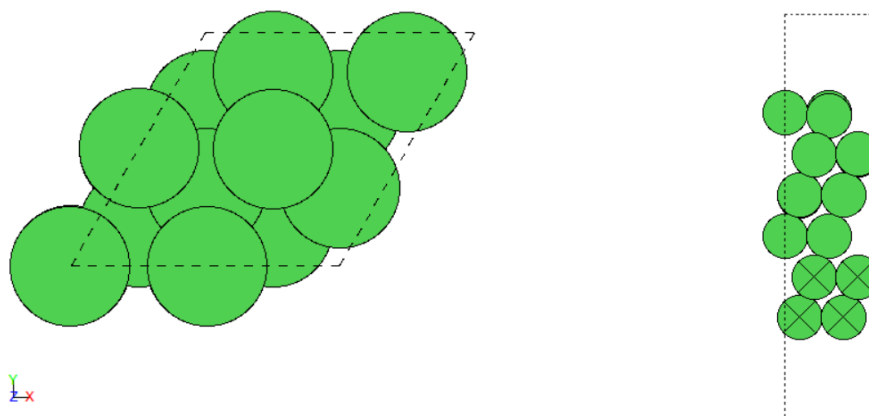


Figure 3.1 Relaxed Ni (111) surface with 5 Å vacuum space on each end, overall 10 Å vacuum space between two slabs along the z-axis for the simulations cell. The bottom two layers are fixed with the top four layers relaxed.

After relaxation, the distance between the first and second layer is increased by 0.24 Å, compared to the bulk structure, while the distance between the second and third layer is increased by 0.18 Å. Layers below the third layer show less variation for these two models. The Ni (111) surface has four available adsorption sites for mono-atom adsorption: bridge site, fcc site, hcp site and ontop site. Bridge site is the site between two closest adjacent atoms. Ontop site is located perpendicular over the surface atom. Fcc site and hcp site are generally called hollow site but for the Ni (111) structure, there are two types of hollow site that differ by the second layer atom location. The four-adsorption sites are shown in Figure 3.2.

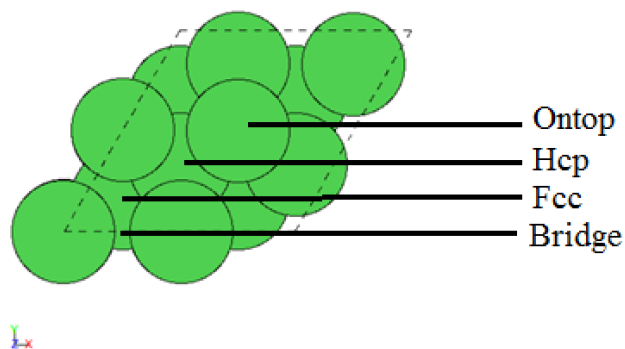


Figure 3.2 Four adsorption site on a Ni (111) surface: ontop, hcp, fcc and bridge site, respectively.

3.1.2 Ni-Cr alloy

Few theoretically studies have focused on the structure of the Ni-Cr alloy system for different Ni-Cr ratios either as large ratios or Cr doped Ni [19-21, 23, 24, 26, 41-43, 55]. For the doped Ni alloys, one Ni atom in the top layer is replaced with one Cr atom [19, 42]. For the structure of Ni-Cr alloy with Ni as dominant ratio, Breidi et al. and Ortiz-Roldan et al. found that the crystal structure will keep an fcc structure [21, 41] in good agreement with the phase diagram shown in Figure 1.5. Das et al. studied water and oxygen adsorption on Ni (111) and fcc structure Ni-Cr (111) surface and they applied three models of the alloy in their study: single Cr atom substitution in the top layer of Ni (111), two Cr atoms substitution in the top layer of Ni (111) and replacement of one Ni atoms in a top layer and one in the second layer [19]. They build a 2x2x4 surface so the Ni-Cr alloy model has three different proportions: $\text{Ni}_{9.4}\text{Cr}_{0.6}$, $\text{Ni}_{8.8}\text{Cr}_{1.2}$ and $\text{Ni}_{7.5}\text{Cr}_{2.5}$, respectively. Their models are shown in Figure 3.3.

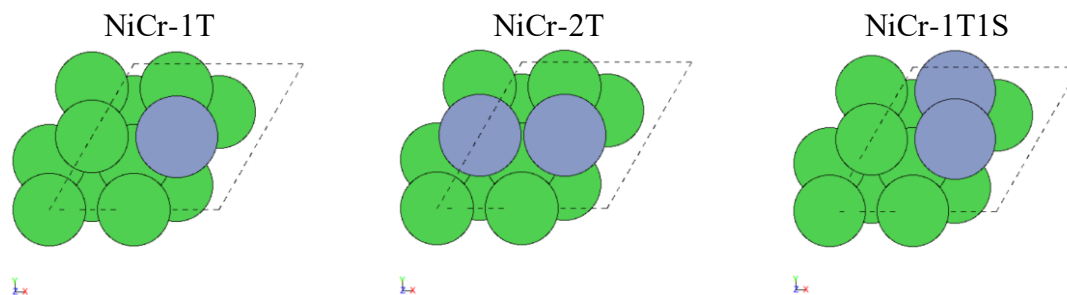


Figure 3.3 Schematic of $\text{Ni}_{9.4}\text{Cr}_{0.6}$, $\text{Ni}_{8.8}\text{Cr}_{1.2}$ and $\text{Ni}_{7.5}\text{Cr}_{2.5}$ based on the models in reference [19]. Ni atoms are shown in green and Cr atoms in grey.

They calculate the bulk energy for each alloy model. The bulk energy difference between the alloy surface and pure Ni (111) for one Cr substitution (NiCr-1T) is -6.31 eV and for the model with two alloying atoms in the top layer (NiCr-2T) is -6.86 eV [19]. The bulk energy for the model with one alloying atoms in top layer and one in the second layer (NiCr-1T1S) is -6.17 eV [19]. All these three models have lower energy than pure Ni bulks. Compared to the other two structures, NiCr-2T configuration has the lowest energy indicating that this structure is the most thermodynamically favored. This structure is also consistent with experimental results which show that Cr tends to aggregate to the surface to form Cr oxide protective film to resist further corrosion [2, 6-8, 22]. Das et al. further investigated Ni-Cr alloy following the Ni-Cr ratio in an Alloy 600, $\text{Ni}_{7.1}\text{Cr}_{1.6}\text{Fe}_{0.6}$ [20]. For their Ni-Cr only calculations, they studied the ratio of Ni to Cr from 8.4 to 1.6 via a substitution model. The model consisted of total of 48 atoms (2x4x6 slab) with 7 Ni atoms substituted by Cr following the designed ratio. Cr atoms were placed in every layer with two atoms in the third layer. The position of the Cr atoms in each layer is arbitrary [20]. Their study focused on the mechanism of the Ni-Cr alloy oxidation process. They

concluded that the reason of the great corrosion resistance of Ni-Cr alloy is the formation of oxide passive layer on the alloy [20]. Since their computational tool is quantum chemical molecular dynamics (QCMD), the final stage of their model was a great starting point for the current study. After 1000fs, the length of their simulations, the Cr atoms have aggregated to the surface and formed a Cr-O passive film on the surface [20]. The final surface does not only have Cr-O bond but also Ni-O bonds indicating that Ni is also one of the components of the oxide passive layer. This result is consistent with experimental observation [5, 7]. It can be concluded from their results that the top layer is composited by Cr, Ni and O but the bonds on the surface are mostly Cr-O bond [20]. This is also consistent with the experiment conclusion that Cr_2O_3 is the main protective layer for Ni-Cr alloy in corrosion [22]. A similar study was also done by Kim et al. based on same type of alloy, alloy 600 [55]. They used a $2 \times 2 \times 4$ Ni model with four Ni atoms replaced by Cr atoms in each layer, as shown in the Figure 3.4 [55]. This is represented in current DFT calculations by modeling the surface with the higher concentration of Cr. Cr is not the only element interacting with O in the top layer but Ni is also presented on the surface.

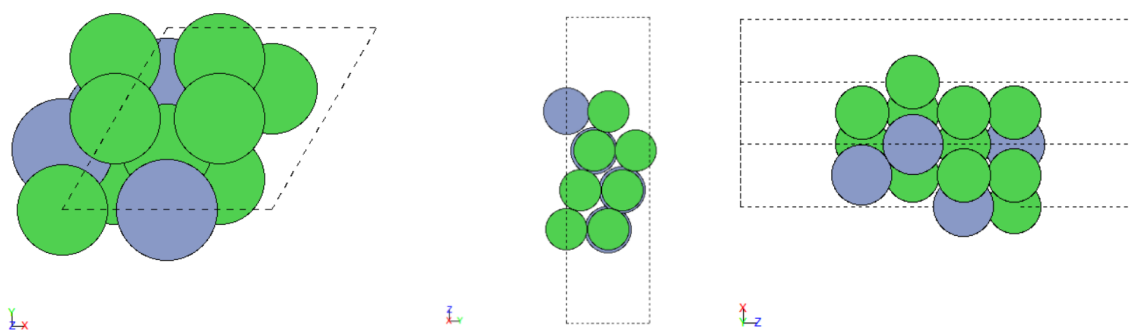


Figure 3.4 $2 \times 2 \times 4$ Ni-Cr (111) alloy surface with four Ni atoms replaced by Cr atoms in each layer based on models from reference [55].

Breidi et al. studied the lattice parameter and formation enthalpy of pure Ni, pure Cr and Ni-Cr with the Exact-Muffin-Tin-Orbitals (EMTO) method and found that the lattice parameter increases with increasing Cr ratio [21]. Although Cr is a well-known to be a bcc structured metal in nature, theoretically calculation for fcc structure Cr indicates that it has larger lattice constant than fcc-Ni. When Cr atoms substitute Ni atoms in the fcc bulk structure, the lattice constant will shift from fcc-Ni closer to fcc-Cr.

Rather than doped and substitution model, some studies investigated and determined the most stable structure for Ni-Cr alloy with specific alloy configuration group [23, 26, 43]. A group of alloys that have same type of crystal structures is classified to an alloy configuration group with a specific name such as $L1_0$, $L1_2$, DO_{60} and $D1_a$ [23]. Rahaman et al. studied the atomic ordering of Ni-Cr alloy in the fcc structure with the screened generalized perturbation method (SGPM) and PAW method [23]. They concluded that for the Ni to Cr ratio of one, type $L1_0$ structure was the most stable bulk structure, shown in Figure 3.5 [23].

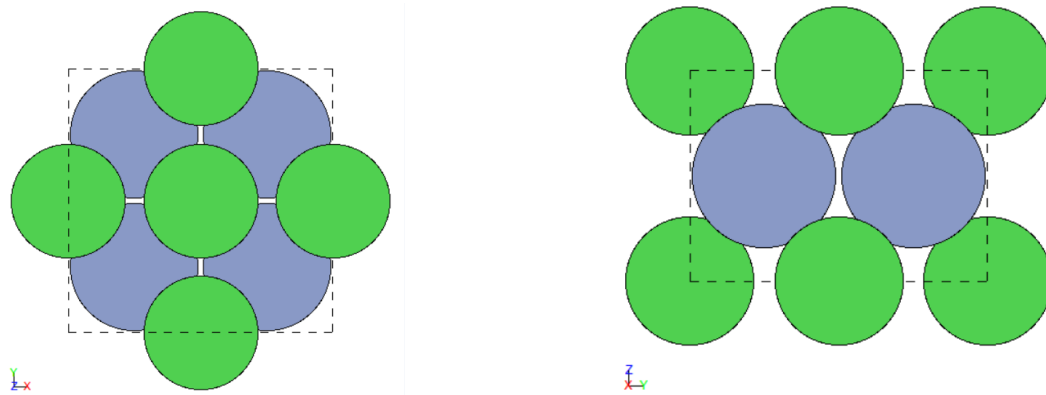


Figure 3.5 Schematics of type $L1_0$ crystal structure of Ni_5Cr_5 alloy.

But for the $\text{Ni}_{6.7}\text{Cr}_{3.3}$ alloy, the most stable atomic order of the Ni-Cr alloy is same as the Pt_2Mo alloy, shown in Figure 3.6 [23].

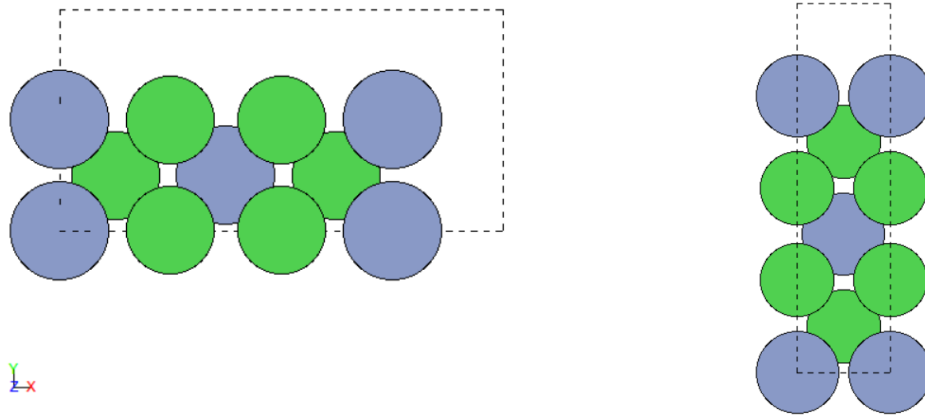


Figure 3.6 Schematics of the most stable bulk crystal structure of $\text{Ni}_{6.7}\text{Cr}_{3.3}$ alloy.

For the Ni to Cr ratio of 7.5 to 2.5, type DO_{60} bulk structure is the most stable structure, shown in Figure 3.7 [23].

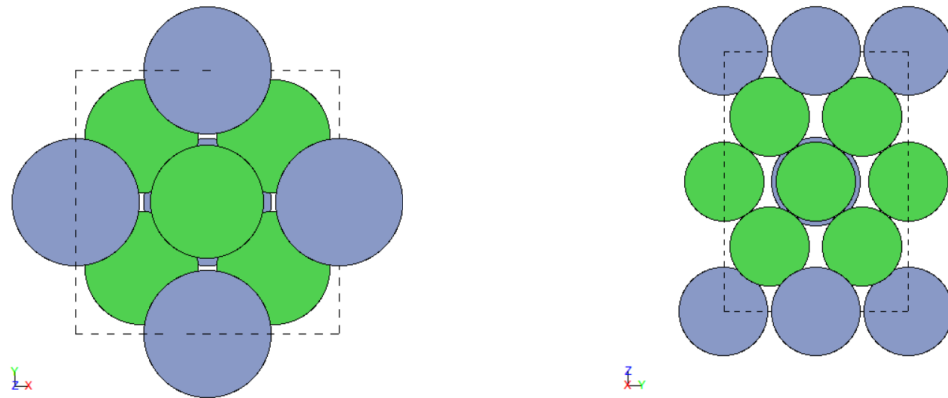


Figure 3.7 Schematics of type DO_{60} bulk crystal structure of $\text{Ni}_{7.5}\text{Cr}_{2.5}$ alloy.

For the 8 to 2 Ni to Cr ratio, type D1_a bulk structure is the most stable structure, which is in the same crystal structure as Ni_4Mo alloy, shown in Figure 3.8 [23].

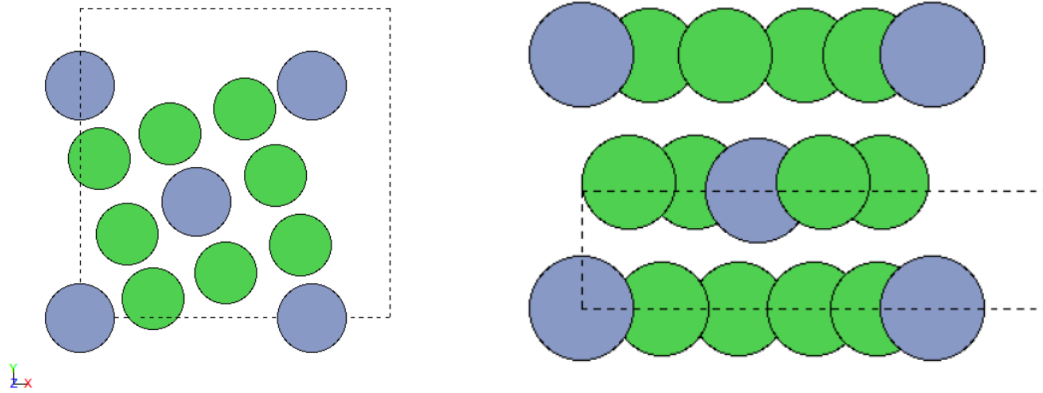


Figure 3.8 Schematic of type D1_a bulk crystal structure of Ni₈Cr₂ alloy.

Connétable et al. studied the formation enthalpies of series of Ni based alloy to determine the most stable crystal structure for Ni-Cr alloy at different Ni-Cr ratio [26]. They determined that there are seven possible configurations that can appear in Ni-Cr alloys at different ratios based on the investigation of alloy Inconel 718 during the solidification process [26]. These possible stable configurations and their corresponding alloys are D0_a, DO₆₀, L1₂ for Ni_{7.5}Cr_{2.5}, D8₅ for Ni₅Cr₅ and C14, C15, C36 for Ni_{6.7}Cr_{3.3} [26]. They employed DFT calculations to determine the most stable configuration of each alloy and concluded that for Ni_{7.5}Cr_{2.5}, L1₂ is the only stable structure, shown in Figure 3.9.

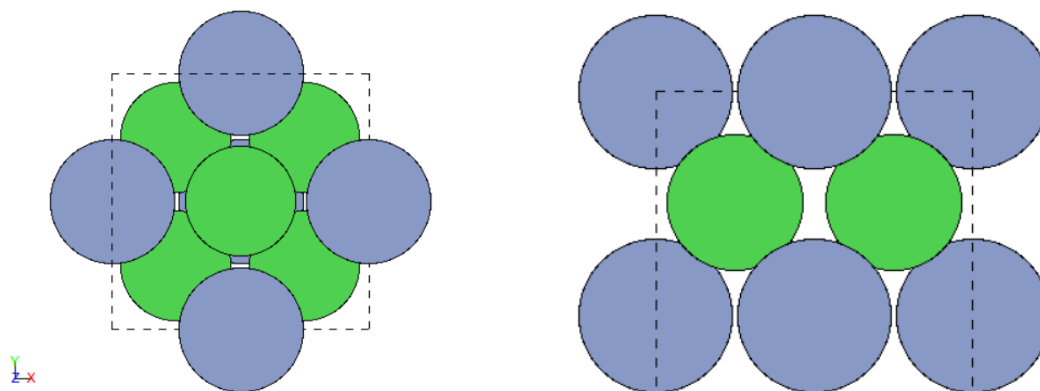


Figure 3.9 Schematic of L1₂ bulk crystal structure of Ni_{7.5}Cr_{2.5} alloy.

The Connétable et al. study did not consider the DO₆₀ structure while few years later Rahaman et al. studied different Ni_{7.5}Cr_{2.5} alloy structure including the DO₆₀ and found the DO₆₀ to be more stable than L1₂ for Ni_{7.5}Cr_{2.5}. Comparing Figure 3.7 and Figure 3.9, the difference between DO₆₀ and L1₂ is the distribution of Cr in the Ni bulk. DO₆₀ has 9 Cr atoms substitute Ni atoms in two adjacent Ni unit cells in z direction while L1₂ has 8 Cr atoms substituted Ni atoms in one unit cell. Each Ni atom in L1₂ configuration interacts with four Cr atoms and eight Ni atoms. The Ni-Cr bond is more complicated in DO₆₀ structure; DO₆₀ can be considered a combination of two L1₂ alloy combination with substitution of a Ni atom in the third layer with Cr atom. As Figure 3.7 shows, Ni atom on the top layer interacts with four Cr atoms and eight Ni atoms which are identical to the L1₂ configuration but the Cr atom in the third layer interacts with 12 Ni atoms. These two conflicting conclusions need further investigation. Connétable et al. also did not determine the thermodynamically stable structure for Ni₅Cr₅ and Ni_{6.7}Cr_{3.3} [26] but the conclusion can be compensated by Bai et al. study which calculated the bulk energy and lattice constant of Ni_{6.7}Cr_{3.3} [43]. Their model is the same as the configuration shown in Figure 3.6.

In current study, we include two different Ni-Cr alloys with Ni-Cr ratios: 5 to 5 and 1.67 to 8.33. For the 5 to 5 ratio, which represents surface enrichment, four models, called Model I, II,

III and IV are tested: in Model I 12 Cr atoms substitute all the fcc-Ni atoms in the top three layers; Model II follows the $L1_0$ structure in the (111) direction. Model III has 12 Ni atoms substituting all the bcc-Cr atoms in every other layers starting in the second layer and Model IV is 12 Ni atoms substituting all the bcc-Cr atoms in the top three layers. The four different models are shown in Figure 3.10 (a-d), respectively. We calculate and compare the lattice constant and lowest bulk energy for all the models. The comparison of the lowest bulk energy will help us determining the most stable configuration of the Ni_5Cr_5 alloy. The computed results are shown in Table 3.1.

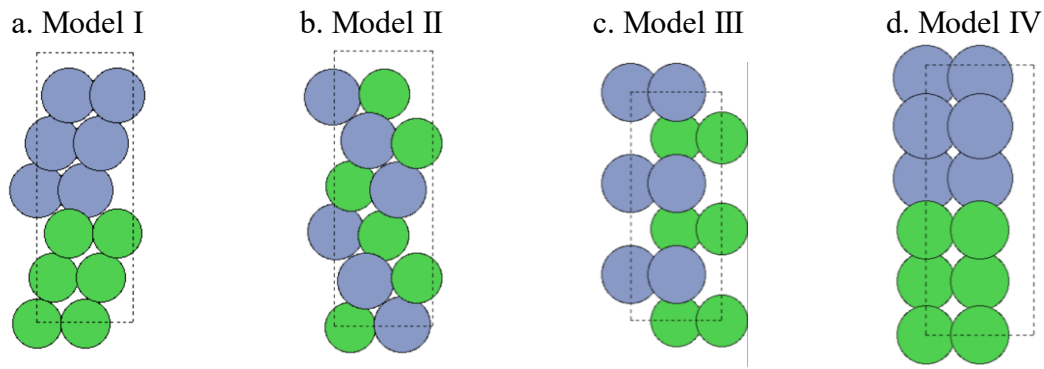
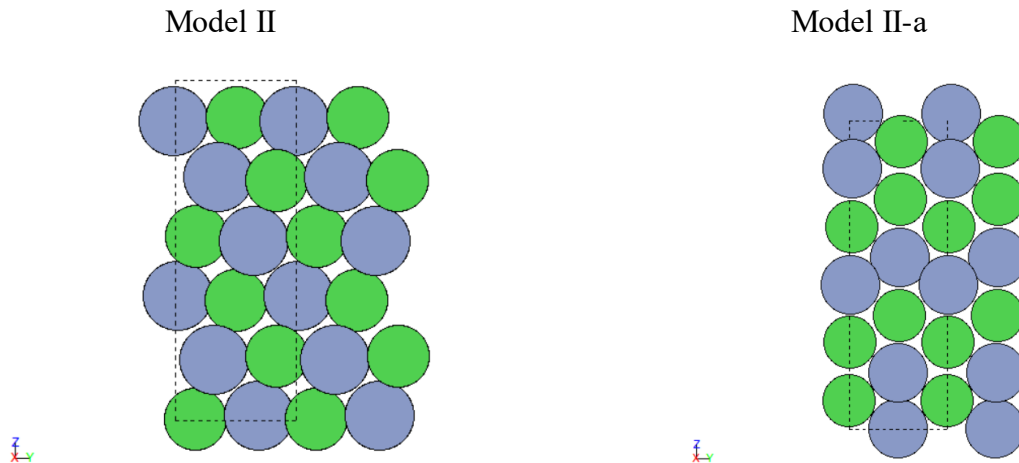


Figure 3.10 Schematics of Ni_5Cr_5 alloy. Model I, a) 12 Cr atoms substitute all fcc-Ni atoms on top three layers. b) Model II, follows $L1_0$ alloy structure, 12 Cr atoms substitute 2 fcc-Ni atoms in each layer. c) Model III, 12 Ni atoms substitute all bcc-Cr atoms in separated layers. d) Model IV, 12 Ni atoms substitute all bcc-Cr atoms in the bottom three layers.

Table 3.1 The lattice constant of Model I to IV of Ni_5Cr_5 alloy

	Lattice Constant (\AA)	Bulk Energy comparing to Model I (eV)
Model I	3.55	0
Model II	3.60	-15.73
Model III	2.82	-1.56
Model IV	2.83	-15

We conclude that Model I configuration is the least stable structure while the bulk energy of Model II is the lowest among the four models. We conclude that Model II, $L1_0$ structure is thermodynamically most favored of these models that are consistent with previous study [23]. We relaxed the volume of all four models and found that only Model II configuration changed significantly. We compared the lowest bulk energy of the changed configuration of Model II, called Model II-a, with the initially designed Model II and find the Model II-a to be more stable. The two models are shown in Figure 3.11.

**Figure 3.11** Schematics of Model II and Model II-a, the $L1_0$ structure after relaxed volume.

We compare the configuration of Model II and Model II-a and found the difference between two models are the atomic ordering in the top and bottom layers but because of the

periodicity of the simulation cell these are all surface layers. Ni atoms and Cr atoms are shifted forming “Ni and Cr stacks” leading to rows of Ni and Cr on the surface. The lowest bulk energy for Model II-a is -7.63 eV lower than Model II, $L1_0$ configuration, indicating that the Model II-a is thermodynamically more stable than Model II. Further adsorption models are based on the Model II-a. For the Model II-a, there are nine adsorption sites available, shown in Figure 3.12.

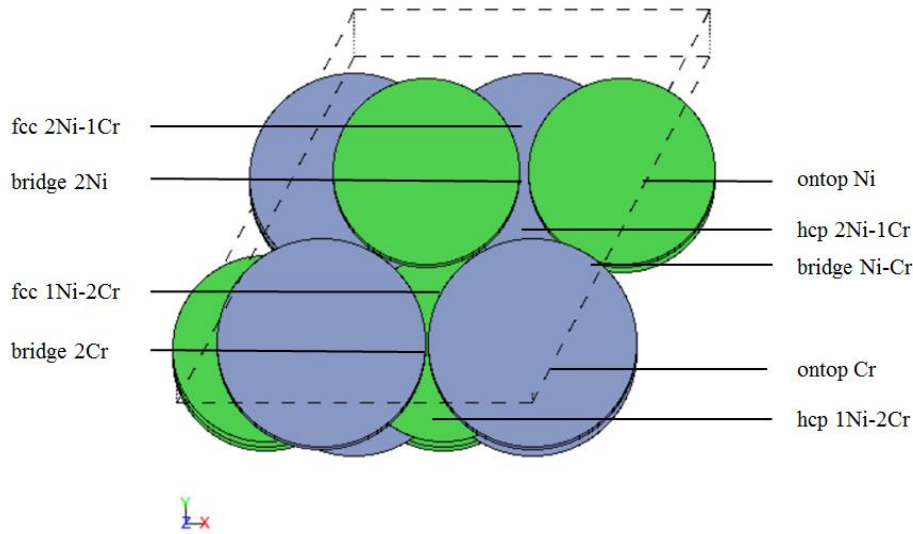


Figure 3.12 Schematics of nine adsorption sites on Ni_5Cr_5 (111) alloy surface.

3.2 DFT computational details

All calculations are performed with Vienna Ab Initio Simulation Package (VASP) [35]. The exchange-correlation energies are represented by generalized gradient approximation (GGA) proposed by Perdew-Burke-Ernzerhof functional (PBE) [34]. $4 \times 4 \times 1$ Monkhost-Pack meshes is applied to sample the Brillouin zone in the reciprocal space. A plane wave energy cutoff of 400eV is applied in the calculation. All geometries are optimized until the forces acting on each atom are converged below 0.01 eV/\AA . For the subsequent Nudged Elastic Band (NEB) calculation [27, 38-40], geometries are optimized until the forces are converged to 0.05 eV/\AA for all images. To test the reliability of the selected K-point mesh, we test the adsorption energy for

CO₂, CO, CO+O and C+O adsorption on Ni (111) surface at different K-points. The results are listed in Table 3.2 and show that adsorption energies are converged to 0.02 eV at 4x4x1 K-points. The adsorption energy is defined in Equation 3.1; where $E_{\text{adsorbate}}$ is the minima energy of the adsorbate far away from the surface; E_{slab} is the total energy of the surface without an adsorbate and E_{tot} is the total energy of the adsorbate on the surface at its minima energy adsorption site. The negative adsorption energy suggested a favorable adsorption and more negative value indicates stronger binding.

$$E_{\text{ad}} = E_{\text{tot}} - E_{\text{adsorbate}} - E_{\text{slab}} \quad \text{Eq. 3.1}$$

Table 3.2 The adsorption energy of CO₂, CO, CO+O and C+O adsorption on Ni (111) surface for different number of K-points:

K points	Adsorption energy (eV)			
	CO ₂	CO	CO+O	C+O
4x4x1	0.24	-1.91	-3.58	-10.96
6x6x1	0.24	-1.92	-3.59	-10.95
8x8x1	0.23	-1.91	-3.57	-10.96

The adsorption energy differences are about 0.01-0.02 eV for the of 4x4x1, 6x6x1 and 8x8x1 k-points mesh. 4x4x1 k-points mesh is therefore sufficient for calculation. We also compute the lattice constant of Ni. The calculated lattice constant for Ni primary cell is 3.52 Å that is consistent with experiment value and calculation value [11, 22] as shown in the Table 3.3.

Table 3.3 Calculated lattice constant and reference data for fcc-Ni, bcc-Ni, bcc-Cr and fcc-Cr.

Lattice Constant	This study (Å)	Reference data (Å)
fcc-Ni	3.52	3.51[56], 3.52[11,22,56], 3.53[56]
bcc-Ni	2.82	2.80 [57]
bcc-Cr	2.83	2.84 [58], 2.86 [59]
fcc-Cr	3.68	3.62 [59]

3.3 Lattice Constant for Ni, Cr and Ni Cr Alloy

3.3.1 Ni

As described in Section 3.2. fcc crystal structure is the most stable structure for Ni. Here we calculate the lattice constant of fcc-Ni. The calculation results and the corresponding reference value are shown in Table 3.3. We also calculate the lattice constant of bcc-Ni. Although bcc is not the nature crystal structure for Ni, it is significant for determine the lattice parameters in Ni-Cr alloys.

The bulk energy for the bcc-Ni is 49.45 eV larger than the bulk energy of fcc-Ni indicating that fcc-Ni is thermodynamically more stable. This conclusion is consistent with experimental findings. We calculated the packing density of bcc crystal structure and fcc structure following the Eq. 3.2:

$$\text{Packing Density} = \frac{\text{Volume of atoms}}{\text{Volume of the unit cell}} = \frac{\frac{4}{3}\pi r^3}{a^3} \quad \text{Eq. 3.2}$$

Whereas r represent the radius of atom and a represent the lattice constant. For fcc crystal structure, there are 4 atoms in a unit cell and the atoms touch along the diagonal of the faces of the cube. The length of the face diagonal equals $\sqrt{2}a$ which is $4r$ so $r = \frac{\sqrt{2}}{4}a$. The calculated packing density for fcc structure is 0.74. For bcc crystal structure, there are 2 atoms in a unit cell and the atoms touch along the body diagonal. The length of the body diagonal is so $\sqrt{3}a$ which is $4r$ so $r = \frac{\sqrt{3}}{4}a$. The calculated packing density for bcc structure is 0.68. Comparing packing density of the two configurations, we obtained that bcc structure is less dense than fcc structure.

3.3.2 Cr

The most stable crystal structure for Cr in nature is bcc. Here, the lattice constant for bcc-Cr has been calculated and compared with experimental findings, shown in Table 3.3. In order to

figure out the reason for the lattice parameter shift in Ni-Cr alloy, the lattice constant for fcc Cr is determined. The bulk energy for fcc-Cr is 9.46 eV higher than bcc-Cr indicating that bcc structure is thermodynamically more favored for Cr. The lattice constant for fcc-Cr is 3.68 Å that is 30 % larger than that of bcc-Cr.

3.3.3 Ni-Cr Alloy

3.3.3.1 Ni_5Cr_5

We calculate the lattice parameters for the most stable structures of Ni_5Cr_5 alloy, Model II-a. The calculation result is shown in Table 3.4. The computed lattice constant is larger than that of fcc-Ni but smaller than fcc-Cr. The reason of the increasing value is that the alloy is still fcc structure so both Ni and Cr in the lattice are in fcc structure. As shown in section 3.3.2.2, the lattice constant for fcc-Cr is 3.68 Å which is 4.5 % larger than that of fcc-Ni. So as a medium state between Ni and Cr, the lattice parameter of Ni-Cr alloy is between the lattice parameters of fcc-Ni and fcc-Cr.

3.3.3.2 $\text{Ni}_{8.33}\text{Cr}_{1.67}$

We also calculate the lattice constant for Ni-Cr alloy for another Ni-Cr ratio, $\text{Ni}_{8.33}\text{Cr}_{1.67}$. The result is also shown in Table 3.4.

Table 3.4 Calculated lattice constant for Ni_5Cr_5 and $\text{Ni}_{8.33}\text{Cr}_{1.67}$ alloy.

Lattice Constant	This study (Å)	% increase from pure Ni
Ni_5Cr_5	3.54	0.5
$\text{Ni}_{8.33}\text{Cr}_{1.67}$	3.53	0.25

The lattice constant for this ratio is also in the range of the lattice constant of fcc-Ni and fcc-Cr. Comparing to the lattice constant of pure Ni, the lattice constant for Ni_5Cr_5 and

$\text{Ni}_{8.33}\text{Cr}_{1.67}$ is increased by 0.5% and 0.25%, respectively. Since there are more fcc-Ni atoms in the bulk, the lattice constant is closer to the fcc-Ni.

3.4 Adsorption models

The interaction between the bottom layer of periodic image and the surface can be neglected with the 10 Å vacuum space. Also, the vacuum space results in a relaxation of the surface atoms to minimize the surface energy discussed earlier in section 3.1.1. All surface atoms, post surface relaxation, are kept frozen during calculation of the adsorption to save computational time. The adsorbates interact with surface atoms either through weak interaction (physisorption) or chemical bonding (chemisorption). The adsorption energy describes the strength of the interaction between the adsorbates and the surface, lower adsorption energy indicates stronger bond.

3.4.1 Adsorption on Ni (111)

3.4.1.1 CO₂ adsorption

Since CO₂ is very stable and has linear configuration in gas phase, in general, CO₂ is expected to have quite weak adsorption interactions with the Ni (111) surface. Previous studies have shown different results for CO₂ adsorption on Ni (111) surface and the initial state for CO₂ dissociation is still debated [9, 10, 56]. Zhu et.al found no one favored adsorption site for CO₂ physisorption on Ni (111) where the CO₂ keeps its linear configuration and the adsorption energy for CO₂ physisorption on Ni (111) was only -0.02eV [56]. They investigated the situations when C was located on fcc, hcp, bridge and ontop site and found that the adsorption energy for all the binding sites are nearly identical indicating that the CO₂ physisorption on Ni (111) surface has no one favored site [56]. The weak interactions supported the finding of rather flat potential

energy surface. They concluded that the covalent bonds between CO₂ molecule and Ni (111) surface fail to form until the CO₂ molecule was artificially bent and activated [56]. Since the bent CO₂ was found not to be stable on the Ni (111) surface, Zhu et al. conclude that the precursor state to initiate the CO₂ decomposition on Ni (111) is physisorbed CO₂ [56]. Similarly, Mohsenzadeh et al. stated that CO₂ molecule fails to bind strongly to Ni (111) with -0.03 eV adsorption energy with CO₂ keeping its linear structure [10]. When CO₂ is bent to an O-C-O bond angle of 133°, the adsorption energy decreases to -0.07eV [10].

Ko et al. came to similar conclusion but obtained stronger interactions than Zhu et al. They found the adsorption energy of CO₂ on Ni (111) to be -0.27eV [9]. Comparing Ko et al. and Zhu et al. approaches, they differ by two points: the converge force criteria and the surface size. Zhu et al. used 3x3x4 slab with bottom layer fixed and converged to 0.01eV/ Å while Ko et al. used 3x3x5 slab with bottom two layers fixed and converged 0.03eV/ Å. This difference is surprising for the same coverage, and same functional and hard to determine the reasons without the raw data. Ko et al. proposed a two-step for CO₂ dissociation mechanism. The first is physisorption of CO₂ on the surface from the gas phase and the second is formation of CO₂^{δ-} adsorbed from the physisorbed CO₂, namely, CO₂ activation [9].

Previous studies for CO₂ dissociation use the activated state CO₂ configuration as the precursor for dissociation, where the activated state of CO₂ is referred to as CO₂^{δ-} [9, 10-14]. The whole process can be described as initial CO₂ physisorption on Ni (111) [9, 14] followed by the electrons transferring from the Ni surface to the CO₂ pulling the CO₂ closer to the surface and bending it [9].

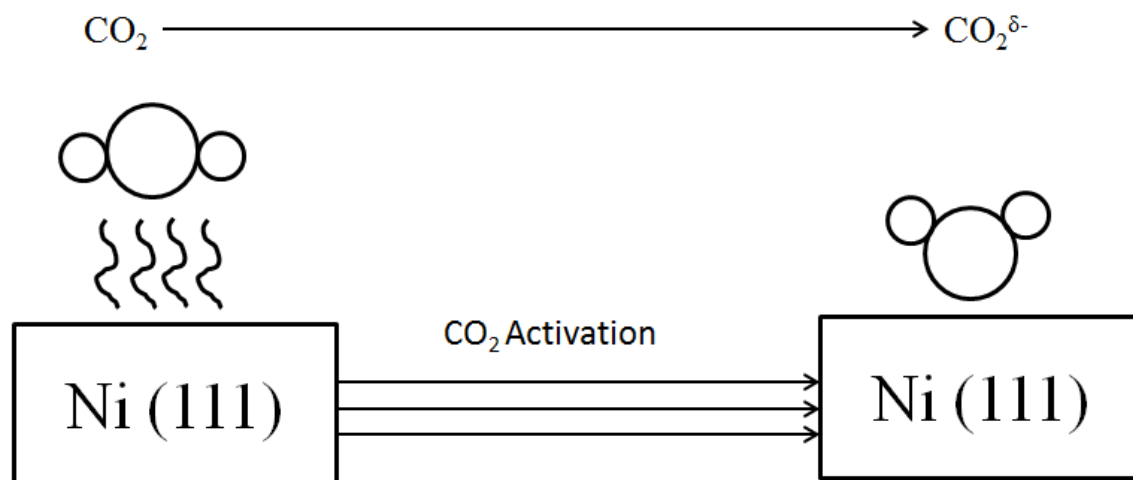


Figure 3.13 Schematic of CO₂ activation process before dissociation. It starts from CO₂ physisorption on Ni surface and is transferred to activated state of CO₂, CO₂^{δ-}, with electrons moving from Ni (111) surface to CO₂.

CO₂ will transition to its activated state CO₂^{δ-} during the process [9, 14]. The activated state of CO₂ actually stands for an intrinsic precursor for CO₂ dissociation [9, 14]. The process of CO₂ physisorption and activation before dissociation can be described in Figure 3.13.

In this study, we model both the CO₂ physisorption and activated state on Ni (111), calculating the adsorption energy and corresponding bonding lengths, the C-Ni length. C-Ni length is defined as the distance between C and the nearest Ni atom. The results, including adsorption energy and bond length for CO₂ physisorption are shown in Table 3.5. The adsorption model is shown in Figure 3.14.

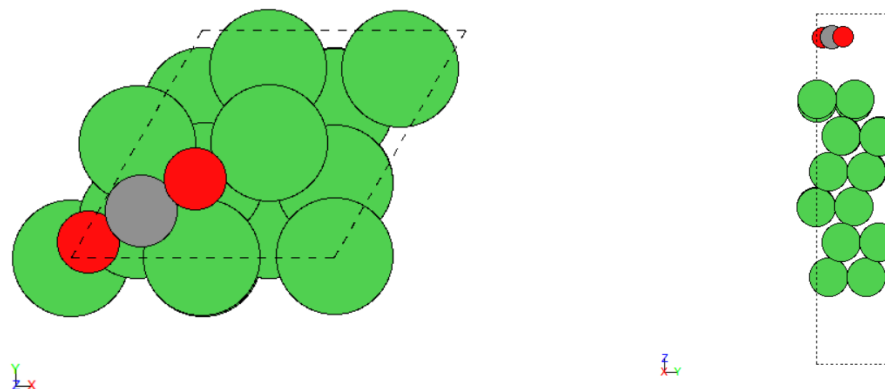


Figure 3.14 Physisorption of CO_2 on Ni (111) surface.

The high adsorption energy indicates that CO_2 interacts very weakly with Ni (111) surface which is consistent with previous finding [56]. Although the interaction is quite weak, it is still thermodynamically stable.

For activated CO_2 , we study the four possible adsorption sites: 2-fold bridge, 4-fold bridge, hcp and fcc. CO_2 molecule on the 2-fold bridge site interacts with two adjacent Ni atoms with one $\text{C}=\text{O}$ bond pointing away from the Ni (111) surface while the other forms a $\text{C}-\text{Ni}$ and $\text{O}-\text{Ni}$ bond on the other end of CO_2 . CO_2 molecule in the 4-fold bridge site interacts with two adjacent Ni atoms but forms $\text{C}-\text{Ni}$ bond and the two O atoms are equal distance from the surface above the Ni atoms. CO_2 on the hcp site interacts with all four Ni atoms on the surface. C occupies the Ni center bridge site and two O atoms occupy fcc and hcp sites, respectively. Two O atoms interact with Ni atoms at on diagonal line. CO_2 molecules in the fcc site interacts with three Ni atoms while C occupies a fcc site with two O atoms occupying ontop and hcp site, respectively. These four adsorption configurations are shown in Figure 3.15 a) to d). Comparison of the structure and adsorption energies for the different configurations is shown in Table 3.5.

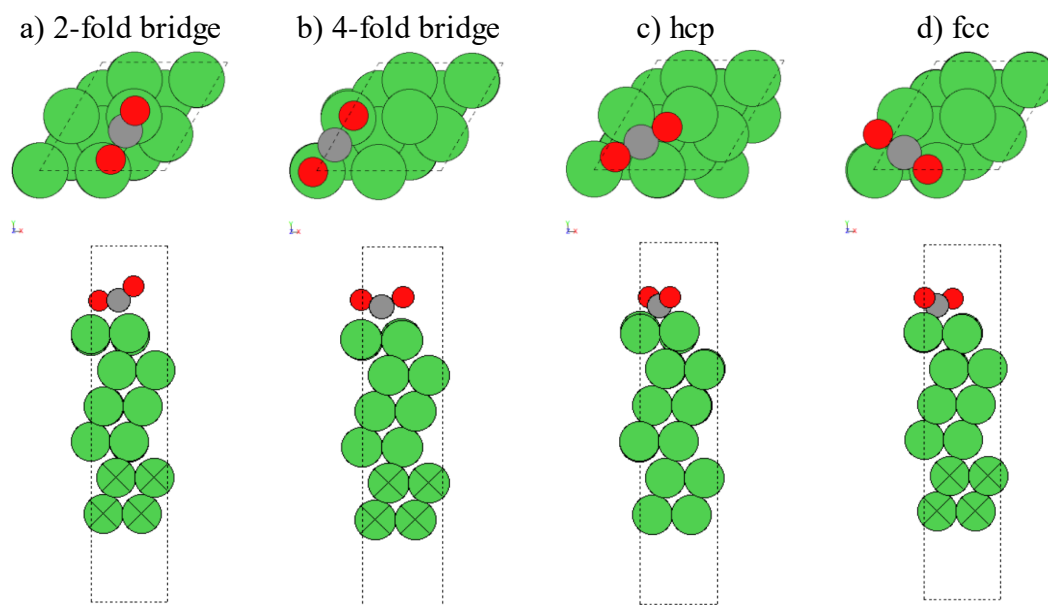


Figure 3.15 Four adsorption configurations for CO₂ activated state on Ni (111).

Table 3.5 Adsorption energy and bond length for CO₂ in physisorption and activated state on Ni (111) surface. The physisorption line refers to a linear adsorption configuration and is the most stable configuration relative to a linear CO₂ in gas phase. The physisorption configuration has flat energy surface and no preferred adsorption site. $E_{\text{ad-linear CO}_2}$ and $E_{\text{ad-bent CO}_2}$ refers to adsorption with reference to linear CO₂ or activate (bent) CO₂ in gas phase respectively.

		$E_{\text{ad-linear CO}_2}$ (eV)	Reference E_{ad} (eV) [9-11,14]	$E_{\text{ad-bent CO}_2}$ (eV)	C-O distance (Å)	C-Ni distance (Å)	O-C-O angle
Physisorption CO ₂		-0.02	-0.02	--	1.18	4.02	180°
Activate CO ₂	2-fold bridge	0.39	0.31	-1.59	1.27	1.98	137°
	4-fold bridge	0.38	0.45	-1.60	1.21	1.99	137°
	hcp	0.24	0.36	-1.74	1.27	2.03	134°
	fcc	0.35	0.46	-1.62	1.26	2.08	133°

The hcp site is has the lowest adsorption energy among all configurations of CO₂ activated state on Ni (111). Previous studies [9-11, 14] calculated the adsorption energy using the linear CO₂ as reference state. Their found the interaction between CO₂ and Ni surface to be positive indicating that adsorption of activated CO₂ on Ni surface is thermodynamically

unfavorable. In our study we also calculate the adsorption energy following their method and get consistent result. Note that adsorption energies are calculated relative to the lowest energy configuration in gas phase, which is linear CO_2 . The positive adsorption energy therefore doesn't exclude favorable interactions between the activated CO_2 and the surface but suggests that the interactions between the CO_2 and the surface are not strong enough to make it more favorable than the linear configuration in the gas phase. So we further studied the interaction with the surface by using the energy of a bent CO_2 as reference state to calculate the adsorption energy and get negative value indicating that the adsorption is thermodynamically stable relative to the bent form in the gas phase.

3.4.1.2 CO adsorption

Previous studies have shown that CO chemisorbs on Ni surfaces [11, 15, 16, 57, 58]. Eichler [57] investigated CO adsorption on different sites of Ni (111) surface at various coverages from 1/12 ML to 1 ML and concluded that the adsorption energy and most favorable adsorption site for CO adsorption on Ni (111) at 1/4 ML coverage was -1.93 eV on an a hcp site. The bond length between C and O was 1.192 Å while the bond length for C and the nearest Ni atom was 1.321 Å. As for other coverage he also found that hcp was the most stable adsorption site for CO adsorption. Xu et al. obtain a consistent conclusion in their study on the co-adsorption phenomenon of CO and H on Ni (111) surface [58]. They found that CO favors the hcp site on Ni (111) with its axis orthogonal to the surface [58]. The adsorption energy was -1.96 eV and the C-Ni bond length was 1.94 Å and the C-O bond length was 1.19 Å [58]. They also stated that the adsorption of CO had little effect on the interlayer distance of the Ni [58]. Mohsenzadeh et al. studied the CO adsorption on Ni (111) surface [11]. They concluded that CO binds to the surface via C with adsorption energy of -1.89 eV [11]. They compared their

calculation data to experimental data and found that the calculated value was 0.5 eV higher than experimental values indicating that the calculated value implied weaker bonding than experimentally observed CO adsorption [11]. They explained that difference as the inability of the PBE functional to accurately predict CO binding energies [11]. They computed the bond length between Ni and C to be 1.15 Å for CO adsorption [11].

We also determine the most favored adsorption site for CO on Ni (111) and compare to previous results from the literature. CO adsorbs perpendicular to the Ni surface with C adjacent to the Ni surface. We calculate the adsorption energy of the bridge, fcc, hcp, and ontop sites. The different adsorption structures are shown in Figure 3.16 and energies and structural parameters are shown in Table 3.6.

Table 3.6 Adsorption energy and bond length for CO chemisorption on Ni (111).

	E_{ad} (eV)	Reference E_{ad} (eV)	C-O distance (Å)	C-Ni distance (Å)	O-C-Ni(111) angle
bridge	-1.80	-1.82[56]	1.19	1.88	90°
fcc	-1.89	-1.91[56]	1.19	1.96	90°
hcp	-1.91	-1.89[11] -1.92[54] -1.93[55] -1.92[54] -1.93[55] -1.96[56]	1.19	1.94	90°
ontop	-1.58	-1.50[56]	1.16	1.73	90°

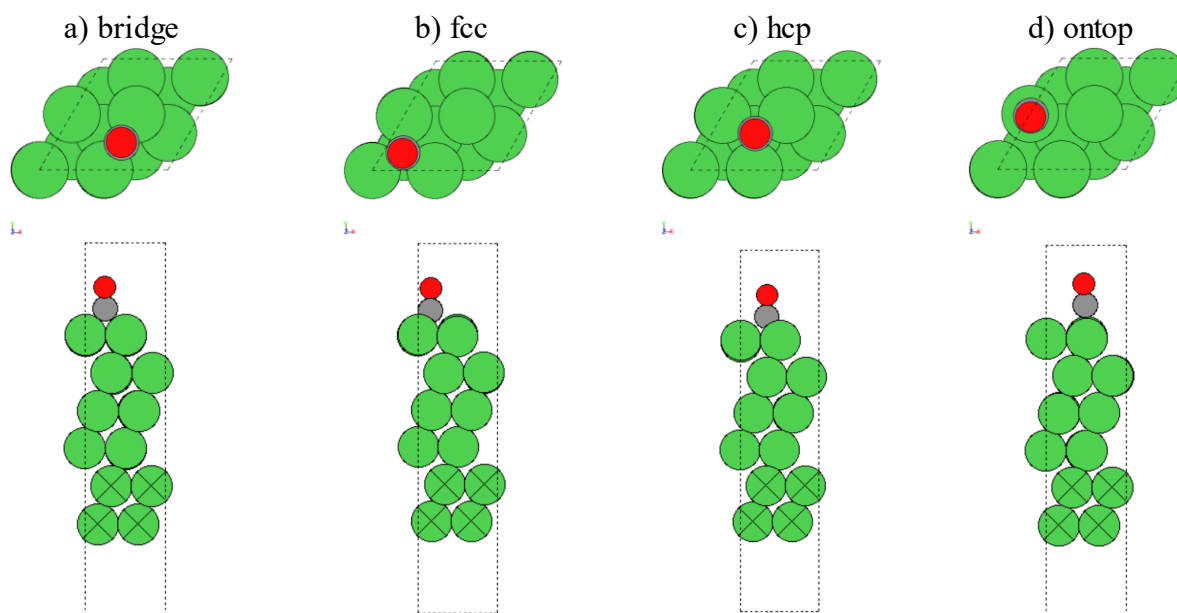


Figure 3.16 Four different adsorbate configurations at different sites for CO chemisorption on Ni (111).

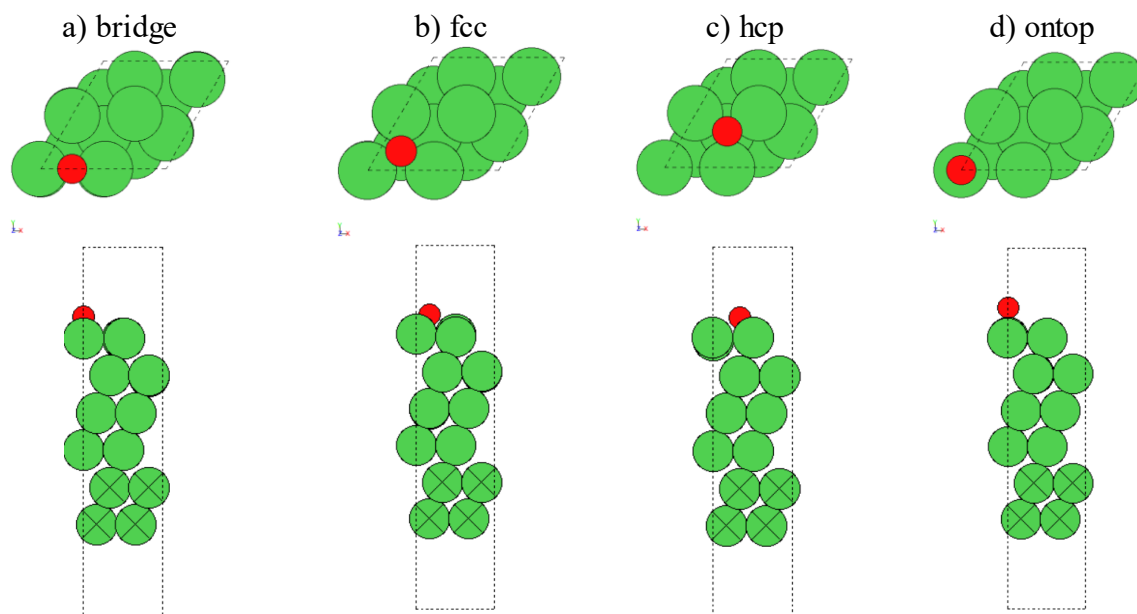
It can be concluded that CO adsorbs perpendicular to the Ni (111) surface with the most stable adsorption site on an hollow site in good agreement with previous literature, but the energy difference between the hcp and the fcc site is barely significant [11, 56-58].

3.4.1.3 O adsorption

Previous research has shown that oxygen adsorption on Ni (111) is most favorable on a fcc site while the distance between O and Ni is 1.86 Å [12]. The adsorption energies and O-Ni bond length for different adsorption site are shown in Table 3.7. Adsorption models are shown in Figure 3.17.

Table 3.7 O adsorption energy and parameter-Ni distance on Ni (111).

	E_{ad} (eV)	Reference E_{ad} (eV)	O-Ni distance (\AA)
bridge	-2.41	-	1.79
fcc	-2.60	-2.81 [60]	1.84
hcp	-1.95	-	1.83
ontop	-0.61	-	1.67

**Figure 3.17** Four adsorption models for O chemisorption on Ni (111). The adsorption energy and bond length agree well with the reference data [62].

The most favored adsorption site for O chemisorbed on Ni (111) surface is an fcc site which is in good agreement with previous studies [62]. The bond length for O to the closest Ni atom is 1.84 \AA that is also consistent with previous calculations [14, 62].

3.4.1.4 C adsorption

Carbon adsorption on Ni (111) has previously been studied as a part of on WGS and dry reforming of methane [12-14, 56]. In this study, we calculate the carbon adsorption on Ni (111).

The calculated adsorption energy and bond distance are shown in Table 3.8. The schematic of the adsorption models is shown in Figure 3.18.

Table 3.8 C adsorption energy and bond length on Ni (111).

	E_{ad} (eV)	Reference E_{ad} (eV)	C-Ni distance (Å)
bridge	-6.38	-	1.72
fcc	-6.79	-	1.77
hcp	-6.85	-6.61 [12], -6.00 [13], -6.61 [14], -6.78 [54],	1.77
ontop	-4.45	-	1.64

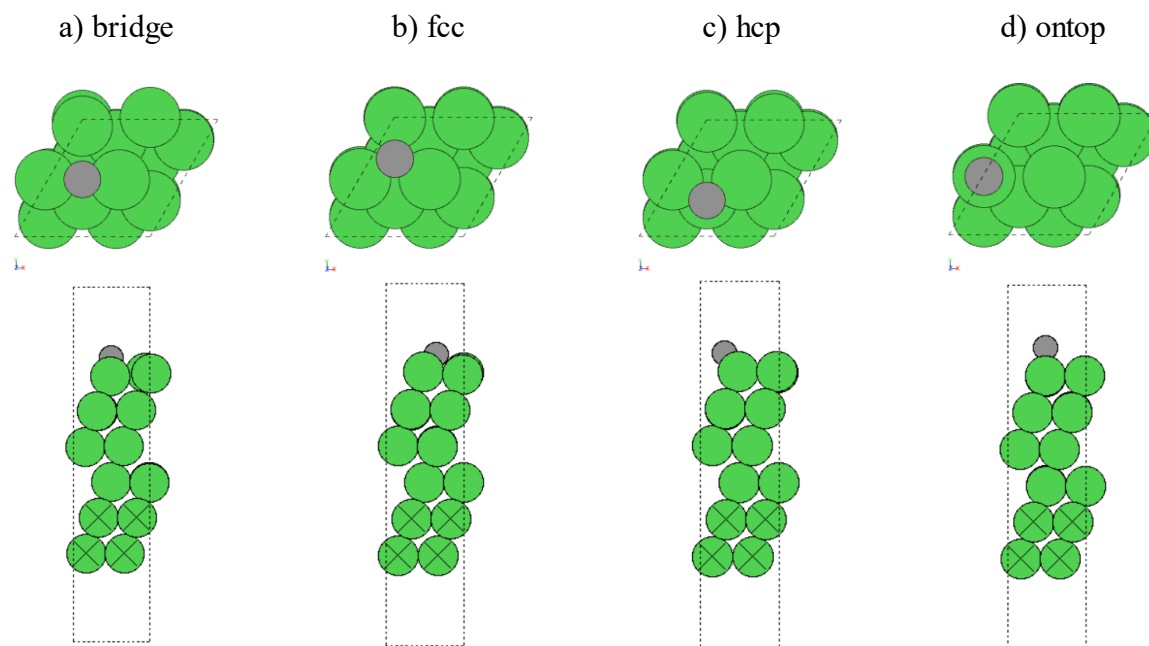


Figure 3.18 Four adsorption models for C chemisorption on Ni (111).

The most favored adsorption site for C on Ni (111) is an fcc site with adsorption energy of -6.85 eV that is consistent with previous studies [12-14, 56]. The distance between C and the closest Ni atom is 1.77 Å. The adsorption energy is quite low indicating strong interaction

between C and Ni.

3.4.1.5 CO and O co-adsorption

The co-adsorption energy for CO and O is studied to determine the reaction energy of the first elementary step of CO₂ dissociation. Since the most stable adsorption site for CO and O mono-adsorption model has been obtained, the co-adsorption model is obtained by putting O in an fcc site as its favored site and put CO on all other available sites on Ni (111), as shown in Figure 3.19.

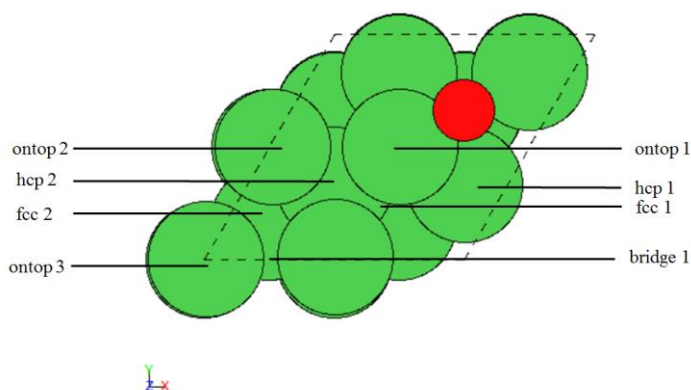


Figure 3.19 Available adsorption sites on Ni (2x2) surface for CO and O co-adsorption.

We find the lowest energy co-adsorption structure to be where CO is on an fcc-2 site and O on an fcc-1 shown in Figure 3.19. The lowest energy configuration identified is shown in Figure 3.20.

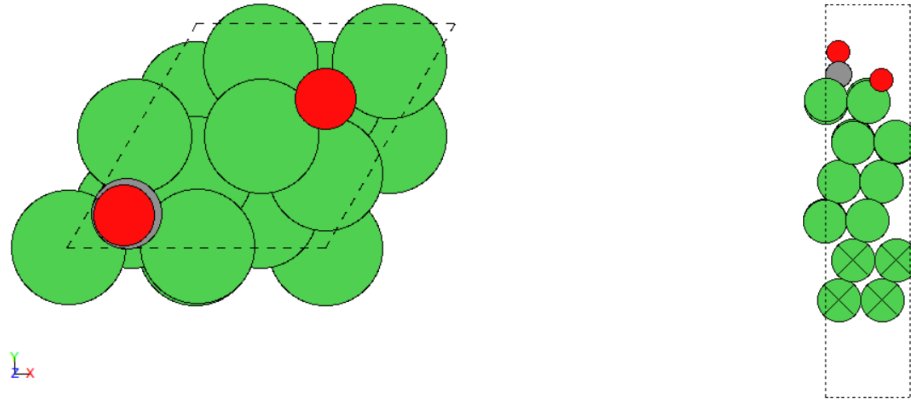


Figure 3.20 Adsorption model for CO and O co-adsorption on Ni (111).

The adsorption energy of CO and O co-adsorption is -6.60 eV. The bond length between C and the closest Ni atom is 1.98 Å and that for O in the co-adsorption model is 1.82 Å. The bond length of CO and O to Ni (111) in the co-adsorption model is similar to CO and O mono-adsorption on the Ni (111). The distance between CO and O is 2.5 Å. The negative value for adsorption energy indicates that the co-adsorption is thermodynamically stable. In the previous sections, we calculated the adsorption energy of single CO and O at fcc site and found them to be -1.89 eV and -2.60 eV respectively, the combined adsorption energy of CO and O infinitely far apart is therefore -4.49 eV which is 2.11 eV higher than the co-adsorbed adsorption energy. This suggests significant attractive interactions between the two adsorbates but does not account for any changes in the adsorbate configuration other than the adsorption site. We also calculate the interaction between CO and O following Eq. 3.3:

$$E_{\text{interaction}} = E_{\text{tot}} - E_{\text{CO}} - E_{\text{O}} - E_{\text{Ni}} - E_{\text{ad-CO}} - E_{\text{ad-O}} \quad \text{Eq.3.3}$$

Whereas $E_{\text{interaction}}$ is the interaction energy between two adsorbates, E_{tot} is the overall energy of the system, $E_{\text{ad-CO}}$ and $E_{\text{ad-O}}$ is the adsorption energy of CO and O in its co-adsorbed

configuration but in absence of the other coadsorbate on Ni surface, respectively. The interaction energy between CO and O is -0.22 eV indicating attractive interactions between CO and O.

3.4.1.6 C and O co-adsorption

The co-adsorption energy of carbon and oxygen on Ni (111) surface is studied to determine the thermodynamic feasibility of the second elementary step of CO₂ dissociation. Similar to the method employed for CO and O co-adsorption, we put O in its most stable adsorption site, fcc, and move C to all possible sites. The available adsorption sites are the same as in the CO and O co-adsorption model, Figure 3.20. We find that the most stable adsorption configurations were O occupies the fcc site while C stays on a hcp site. The lowest energy adsorption configurations are shown in Figure 3.21.

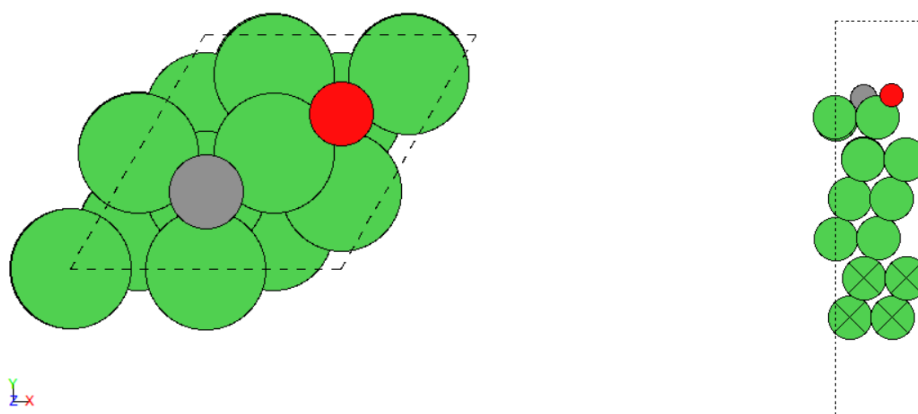


Figure 3.21 Adsorption model for C and O co-adsorption on Ni (111).

The total co-adsorption energy is -10.96 eV indicating that the structure is very stable. The bond length between C and closest Ni atom is 1.76 Å and that for O adsorption in the co-adsorption model is 1.83 Å which is the same adsorbate-Ni distance (within 0.01 Å) as for the mono-adsorption. The distance between C and O is 2.88 Å. The adsorption energy is more negative, by 1.51 eV, than the combined C and O mono-adsorption on Ni (111) indicating that

the co-adsorption for C and O model is more stable than when adsorbed separately on Ni (111).

We also calculate the interaction between C and O following Eq. 3.4:

$$E_{\text{interaction}} = E_{\text{tot}} - E_{\text{C}} - E_{\text{O}} - E_{\text{Ni}} - E_{\text{ad-C}} - E_{\text{ad-O}} \quad \text{Eq.3.4}$$

Whereas $E_{\text{ad-C}}$ is the adsorption energy for C with absence of O in the coadsorption model on Ni surface. The computed interaction energy between C and O is -0.59 eV indicating C and O has an attractive interaction to each other.

3.4.2 Adsorption on Ni-Cr alloy

3.4.2.1 $\text{Ni}_{8.33}\text{Cr}_{1.67}$

3.4.2.1.1 CO_2 adsorption

We investigated CO_2 physisorption and activated state on $\text{Ni}_{8.33}\text{Cr}_{1.67}$ surface. The interaction of CO_2 with Ni-Cr alloy was initially calculated assuming a straight, gas-phase like configuration of CO_2 . We found no stable adsorption configuration for linear CO_2 on the $\text{Ni}_{8.33}\text{Cr}_{1.67}$ alloy.

The activated state of CO_2 , $\text{CO}_2^{\delta-}$, on $\text{Ni}_{8.33}\text{Cr}_{1.67}$ surface is investigated by artificially activating the CO_2 prior to adsorption. The CO_2 was initially put on four adsorption sites on the surface: two fold bridge, four fold bridge, fcc and hcp. On pure Ni, the $\text{CO}_2^{\delta-}$ interacts with the C atom while the two oxygen atoms point away from the surface. On the alloyed surface the CO_2 molecule has about 20° smaller in O-C-O angle then on Ni and lies nearly parallel to the alloy surface suggesting favorable interactions between the O and the surface. The decrease in adsorption energy supports this observation. The adsorbate configurations are shown in Figure 3.22 a) to d) and the results are summarized in Table 3.9.

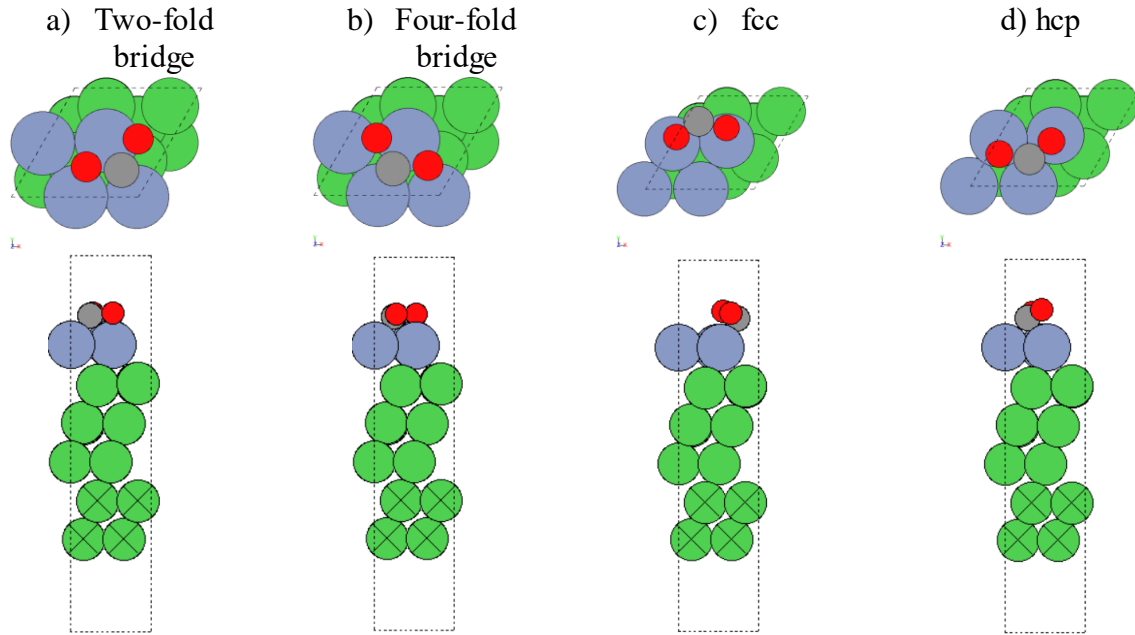


Figure 3.22 Four different adsorption configurations for $\text{CO}_2^{\delta-}$ on $\text{Ni}_{8.33}\text{Cr}_{1.67}$ alloy.

Table 3.9 Adsorption energy and bond length for CO_2 activated state on $\text{Ni}_{8.33}\text{Cr}_{1.67}$ alloy.

	$E_{\text{ad-linear CO}_2}$ (eV)	$E_{\text{ad-bent CO}_2}$ (eV)	C-O distance (Å)	C-Cr distance (Å)	O-Cr distance (Å)	O-C-O angle
2-fold bridge	0.19	-4.72	1.39	1.93	2.05	111°
4-fold bridge	0.18	-4.73	1.39	1.94	2.05	112°
fcc	0.24	-4.67	1.31	1.95	1.94	121°
hcp	0.25	-4.66	1.30	1.95	1.99	122°

We find that the most stable adsorption site for CO_2 on the alloy surface is bridge site. The adsorption energy for 2-fold bridge and 4-fold bridge are 0.19 and 0.18 eV respectively. The positive value indicates that activated state CO_2 is thermodynamically unstable but slight more stable than $\text{CO}_2^{\delta-}$ adsorption on Ni (111) suggesting a slight stabilizing effect from the alloying. We further employ the bent CO_2 as reference state to calculate the adsorption energy of the activated CO_2 and obtain negative value indicating that attractive interactions between the

activated CO₂ and the surface. The adsorption energy of CO₂ using bent CO₂ as reference state is lower than that of Ni (111) further suggesting that the Ni-Cr alloy will enhance the adsorption of CO₂.

3.4.2.1.2 CO adsorption

The CO adsorption is studied on the Ni_{8.33}Cr_{1.67} alloy. There are four adsorption sites, same as for the Ni (111) surface in Figure 3.2, available. The calculation results are shown in Table 3.10.

Table 3.10 Adsorption energy and bond length for CO chemisorption on Ni_{8.33}Cr_{1.67}.

	E_{ad} (eV)	C-O distance (Å)	C-Cr distance (Å)	O-C-Cr(111) angle
bridge	-1.92	1.18	1.88	73.3°
fcc	-0.76	1.19	1.82	28.3°
hcp	-0.96	1.19	2.12	89.7°
ontop	-1.03	1.19	1.88	90.0°

The adsorption configurations are shown in Figure 3.23 a-d

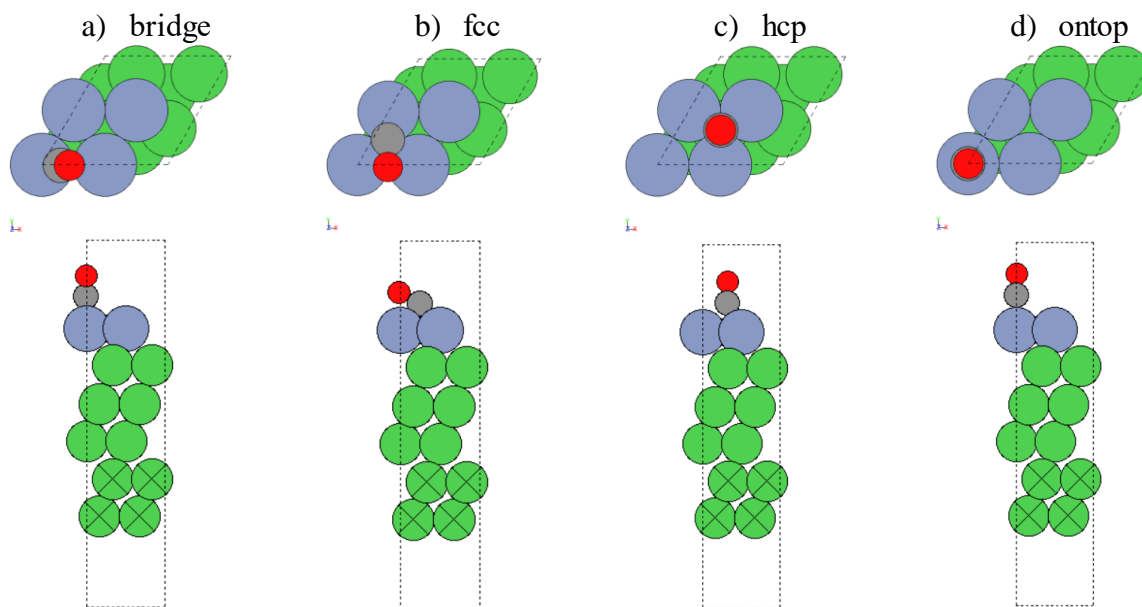


Figure 3.23 a) bridge site; b) fcc adsorption; c) hcp adsorption; d) ontop adsorption for CO on Ni_{8.33}Cr_{1.67}.

We compare the results from the alloy calculations with data for CO on Ni (111) surface; the most favored adsorption site is bridge site in the alloy models which is different from the pure Ni model where CO is most stable on a hollow site. The adsorption energy for this alloy model is almost -2 eV indicating strong interactions between CO and the alloy surface. The difference between the adsorption energy between this alloy model and pure Ni is only 0.01 eV and therefore not significant. We conclude that although the adsorption site is different from the pure Ni, the adsorption energy is nearly same as for pure Ni model indicating that the interaction between C and alloy surface is still strong. The bond length between C and O is same, around 1.19Å. Difference from CO adsorbed perpendicularly to the surface, some CO adsorption configuration on the alloy surface will tilt to a specific angle indicating the strong interaction between O and the surface.

3.4.2.1.3 O adsorption

We studied the adsorption of O atom on $\text{Ni}_{8.33}\text{Cr}_{1.67}$ surface. Four adsorption models are investigated to determine the most stable adsorption site and its adsorption energy. The calculation results are shown in Table 3.11. Here we summarized the adsorption energy and the distance between O atoms to the nearest Cr atom.

Table 3.11 O adsorption energy and bond length on $\text{Ni}_{8.33}\text{Cr}_{1.67}$.

	E_{ad} (eV)	O-Cr distance (Å)
bridge	-3.90	1.90
fcc	-2.99	1.90
hcp	-4.19	1.88
ontop	-1.24	1.66

The adsorption model is shown in Figure 3.24 a to d:

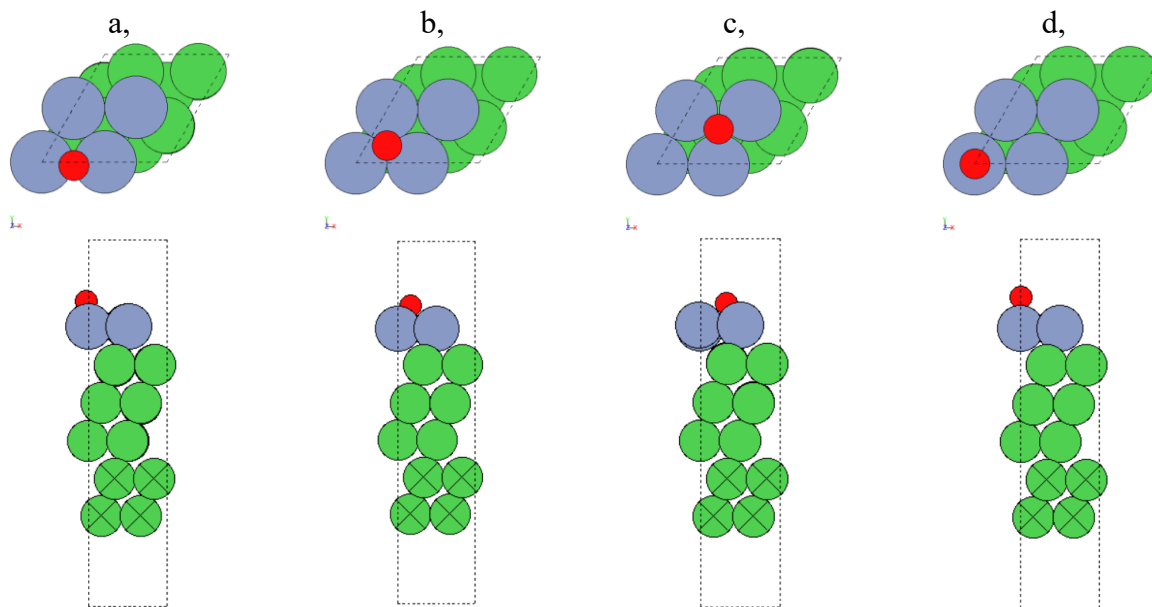


Figure 3.24 Four adsorption models for O adsorption on $\text{Ni}_{8.33}\text{Cr}_{1.67}$ alloy.

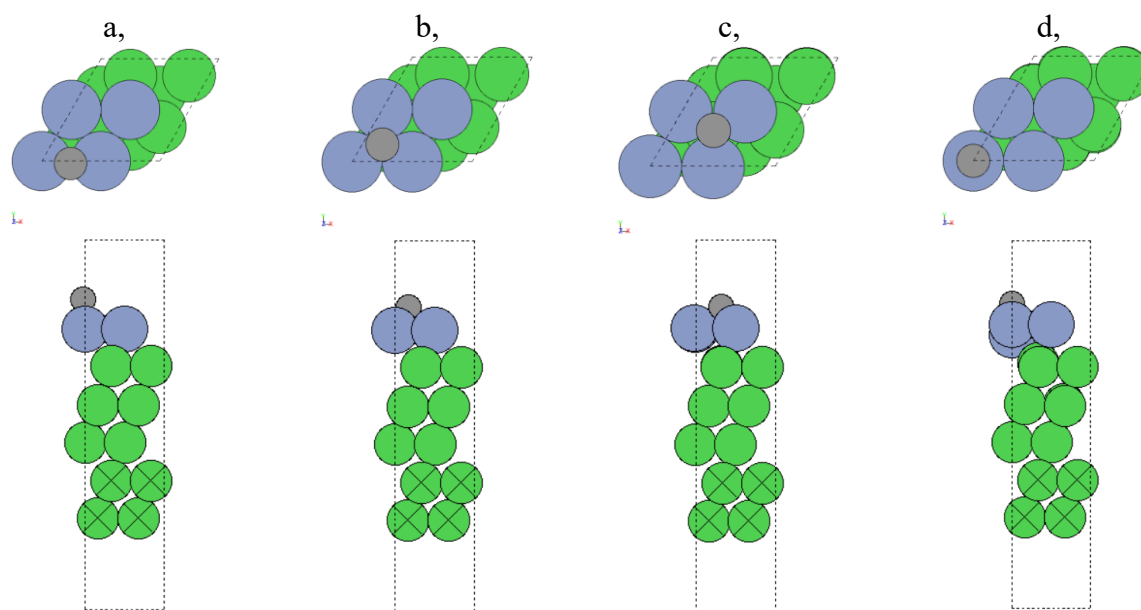
The most favored adsorption site for O atom on $\text{Ni}_{8.33}\text{Cr}_{1.67}$ is the hcp site with adsorption energy of -4.19 eV. The adsorption energy for the alloy model is nearly 1.5 times lower than that for pure Ni surface indicating that oxygen atom interacts much stronger with the alloy surface. The much stronger interaction for O on alloy the surface indicates that that Cr is more oxophilic than Ni and may suggest that the oxygen passive film is easier to form on Ni-Cr surface. This observation is consistent with Das et al. investigation on Ni-Cr alloy [19].

3.4.2.1.4 C adsorption

The adsorption model of carbon on $\text{Ni}_{8.33}\text{Cr}_{1.67}$ is studied and the adsorption energy is calculated. We found that the bridge site, as shown in Figure 3.23 a), is unstable for C adsorption. Results for C adsorption are summarized in Table 3.12 and in Figure 3.25.

Table 3.12 C adsorption energy and bond length on $\text{Ni}_{8.33}\text{Cr}_{1.67}$.

	E_{ad} (eV)	C-Cr distance (\AA)
bridge	-	-
fcc	-6.22	1.87
hcp	-7.33	1.86
ontop	-5.22	1.71

**Figure 3.25** Four adsorption models for C adsorption on $\text{Ni}_{8.33}\text{Cr}_{1.67}$ alloy.

C is most stable on a hcp site on $\text{Ni}_{8.33}\text{Cr}_{1.67}$ alloy surface with adsorption energy of -7.33 eV. The adsorption energy is lower than on pure Ni surface indicating that C interacts stronger with the alloy surface than Ni (111).

3.4.2.1.5 CO and O co-adsorption

We studied the co-adsorption model of CO and O on $\text{Ni}_{8.33}\text{Cr}_{1.67}$ alloy surface, as before we place the O on its most favored adsorption site and move CO to other sites on the surface to calculate the most stable configuration of the co-adsorption. The most stable configuration of the

co-adsorption was when CO adsorbs in ontop site and O occupies hcp site, as shown in Figure 3.26.

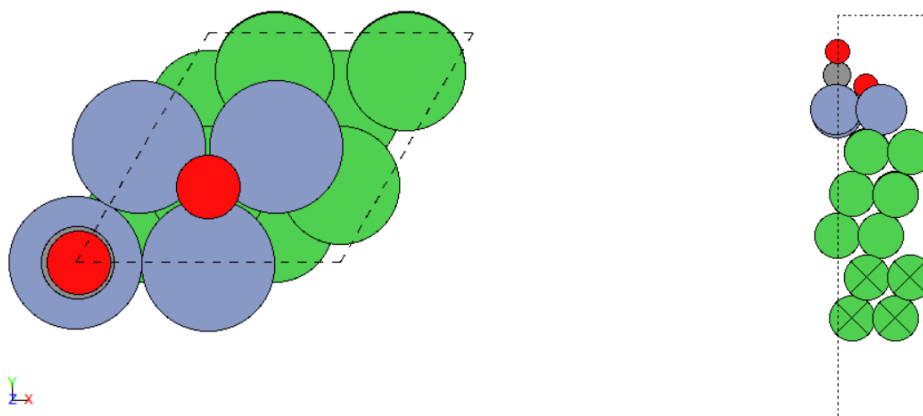


Figure 3.26 Adsorption model for CO and O co-adsorption on $\text{Ni}_{8.33}\text{Cr}_{1.67}$.

The co-adsorption energy is -8.97 eV and lower than the adsorption energy on pure Ni surface indicating that the co-adsorption for CO and O on the alloy surface is more stable than on pure Ni surface. The bond length between C and closest Cr is 1.89 Å and 1.87 Å for O. Distance between CO and O is 2.86 Å. The co-adsorption of CO and O is 3.75 eV lower in energy than the individual molecules/atoms adsorbed on the same surface and adsorption sites indicating that the interaction between CO and O is attractive. The co-adsorption is more favored on this alloy surface than the pure Ni (111) and the distance between the two adsorbates is slightly larger. We further calculate the interactions between two adsorbates following the Eq. 3.3 and get the energy between CO and O is -0.19 eV indicating that the interaction between CO and O is attractive.

3.4.2.1.6 C and O co-adsorption

The co-adsorption model for C atom and O atom is studied by putting C on its favored adsorption site, hcp site and putting O on all other available sites to determine the most stable

model for C and O co-adsorption. Configuration where C occupies one hcp site while O stays on the adjacent fcc site is the most stable adsorbate configuration model for C and O co-adsorption on $\text{Ni}_{8.33}\text{Cr}_{1.67}$. The results are shown as Figure 3.27.

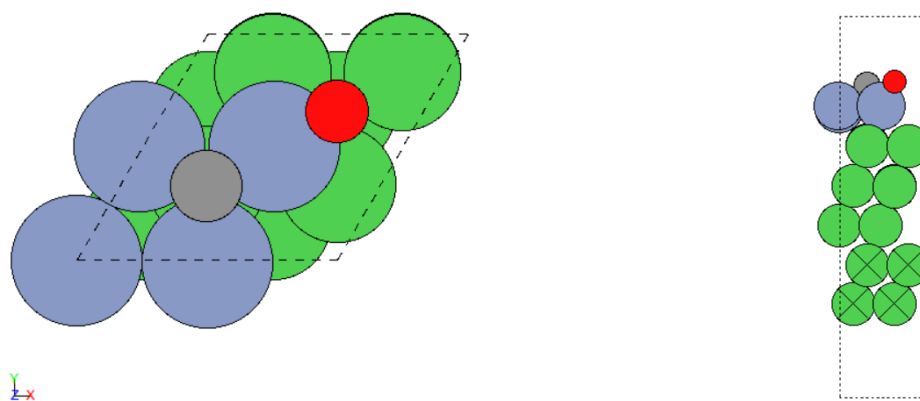


Figure 3.27 Adsorption model for C and O co-adsorption on $\text{Ni}_{8.33}\text{Cr}_{1.67}$.

The adsorption energy is -12.85 eV indicating that the structure is quite stable. The bond length between C and nearest Cr atom is 1.83 Å and that for O adsorption in this co-adsorption model is 1.85 Å. The distance between C and O is 2.90 Å. The negative value for adsorption energy indicates that the co-adsorption model is thermodynamically stable. The adsorption energy is 1.89 eV lower than that on pure Ni surface indicating that the interaction between the adsorbates and alloy surface is more stable than on the pure metal. The bond length between the adsorbates and the alloy surface is same as on the Ni surface. This co-adsorbate structure is also 2.43 eV lower in energy than the mono-adsorbates in the same adsorption site suggestion significant attractive interaction between the two. We also study the interaction between two adsorbates and calculate the energy between them following Eq. 3.4. We obtain the interaction as

-0.58 eV indicating that there are attractive interactions between two adsorbates on the alloy surface.

3.4.2.2 Ni_5Cr_5

3.4.2.2.1 CO_2 adsorption

We studied CO_2 adsorption on the Ni_5Cr_5 surface. CO_2 physisorption is studied by putting CO_2 molecule several Ångström away from the alloy surface while keeping the linear configuration of the CO_2 . The calculated model is shown in Figure 3.28.

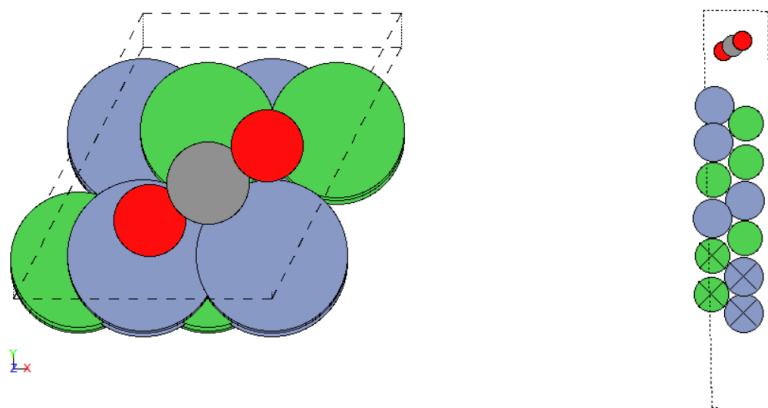


Figure 3.28 Configuration of CO_2 physisorption on Ni_5Cr_5 surface.

The physisorption energy is -0.13 eV indicating that the physisorption of the linear CO_2 is thermodynamically favored. The distance between CO_2 molecule to the surface is 3.70 Å and the bond length between C and O is 1.18 Å.

For the activated state, CO_2 molecule is initially put on bridge 2Ni, bridge 2Cr, fcc 1Ni-2Cr and hcp 2Ni-1Cr site, the results are shown in Figure 3.29 and Table 3.13.

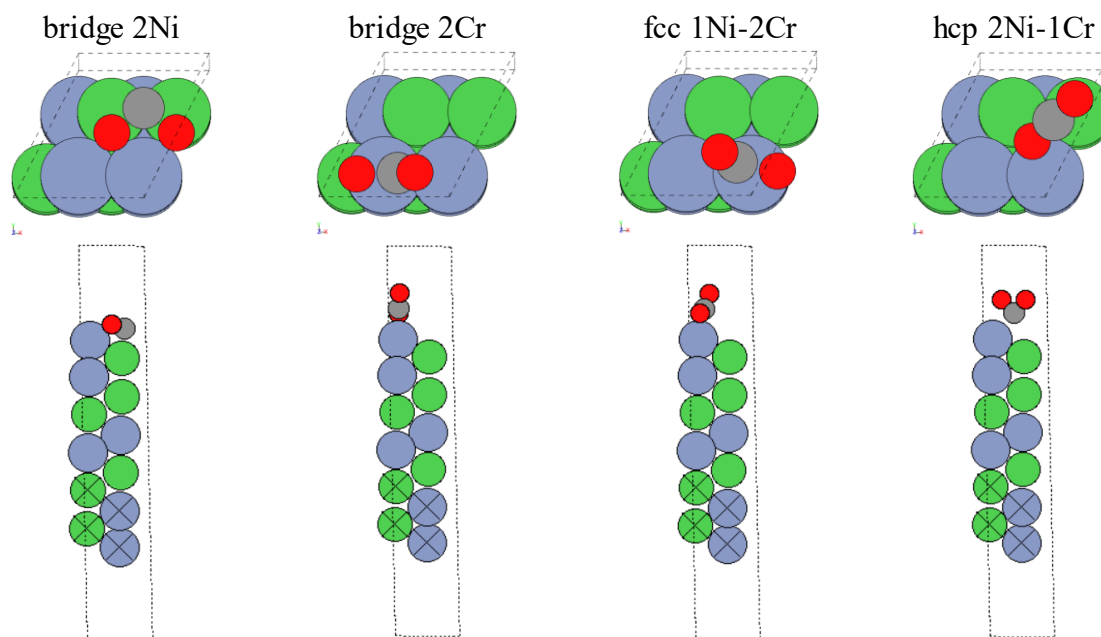


Figure 3.29 Activated state of CO₂ on Ni₅Cr₅ surface.

Table 3.13 Adsorption energy and bond length for CO₂ activated state on Ni₅Cr₅ alloy.

	$E_{\text{ad-linear CO}_2}$ (eV)	$E_{\text{ad-bent CO}_2}$ (eV)	C-O distance (Å)	O-C-O angle
bridge 2Ni	0.75	-1.66	1.35	111°
bridge 2Cr	-0.71	-3.13	1.19	130°
fcc 1Ni-2Cr	-0.76	-3.18	1.20	130°
hcp 1Ni-2Cr	0.70	-1.71	1.40	112°

We find two stable configurations for activated CO₂ on the Ni₅Cr₅ alloy, bridge 2Cr and fcc 1Ni-2Cr. In both of these configurations the C of CO₂ interacts with a top site of Cr, so although the adsorbates started as different configurations they have converged to a similar one. The adsorption energy is -0.76 eV indicating that the activated state of CO₂ on Ni₅Cr₅ alloy is thermodynamically favored but the interaction is weak. The adsorption energy of the activated CO₂ state calculated with linear CO₂ as reference state on the Ni₅Cr₅ alloy negative while for Ni (111) and Ni_{8.33}Cr_{1.67} alloy it is positive indicating stronger interactions and thermodynamically

avored CO₂ adsorption on the Ni₅Cr₅ alloy surface. We also calculate the adsorption energy employing the bent CO₂ as reference state and obtain negative values indicating attractive interactions between the activated CO₂ and the Ni₅Cr₅ alloy. Comparing the CO₂ adsorption energy, using linear CO₂ as reference state, for the three surfaces, we conclude that the Cr content will enhance the adsorption of CO₂ on the surface.

3.4.2.2.2 CO adsorption

We investigated the CO adsorption on the Ni₅Cr₅ surface. The most stable adsorption site for CO adsorption is a bridge site. As shown in Figure 3.30.

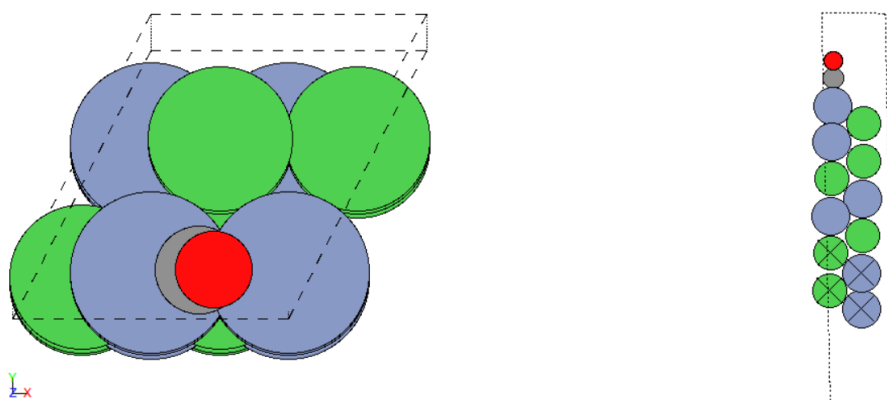


Figure 3.30 The most stable adsorption site for CO adsorption on Ni₅Cr₅ surface.

The adsorption energy is -1.89 eV. The bond length between C and the nearest Cr is 1.96 Å. The lowest adsorption energy is close to that on pure Ni surface but the CO is more tilted to the side on the alloy surface indicating a slight surface O interaction. The angle of CO and the alloy surface is 79.4°.

3.4.2.2.3 O adsorption

We studied the O adsorption on Ni_5Cr_5 following the nine adsorption sites in Figure 3.12.

The most stable adsorption site for O on the alloy is bridge site, as shown in Figure 3.31.

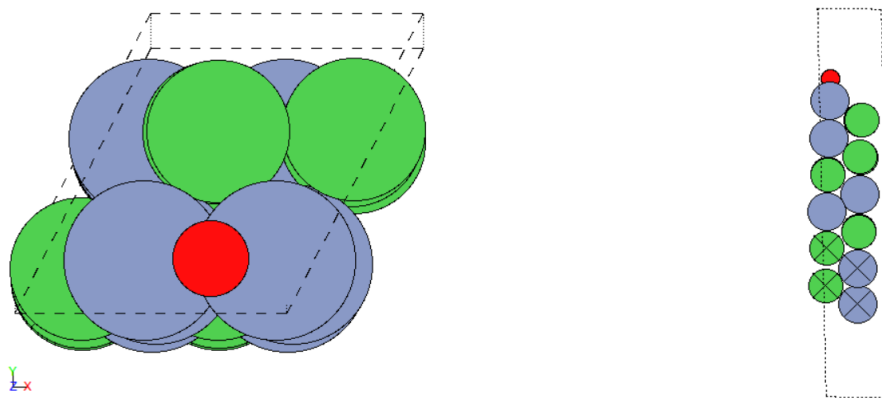


Figure 3.31 The most stable adsorption site for O adsorption on Ni_5Cr_5 surface.

The adsorption energy for O adsorb on Ni_5Cr_5 surface is -6.75eV . The bond length between O and Cr is 1.79 \AA . The adsorbate interaction is stronger than oxygen adsorption on pure Ni surface by 0.92 eV but 0.67 eV weaker than on the $\text{Ni}_{8.33}\text{Cr}_{1.67}$ indicating that higher Cr content on the surface will lead to stronger surface-O interactions in agreement with previous studies [19]. So we can conclude based on our observation in Section 3.4.1.3 that O adsorption is enhanced when Ni is alloyed with Cr making it easier to form a chrome oxide than on pure Ni surface.

3.4.2.2.4 C adsorption

The chemisorption of C on Ni_5Cr_5 alloy surface is investigated. The most stable adsorption site is a bridge site with adsorption energy of -7.50 eV , Figure 3.32. The bond length between C and the nearest Ni is 1.89 \AA .

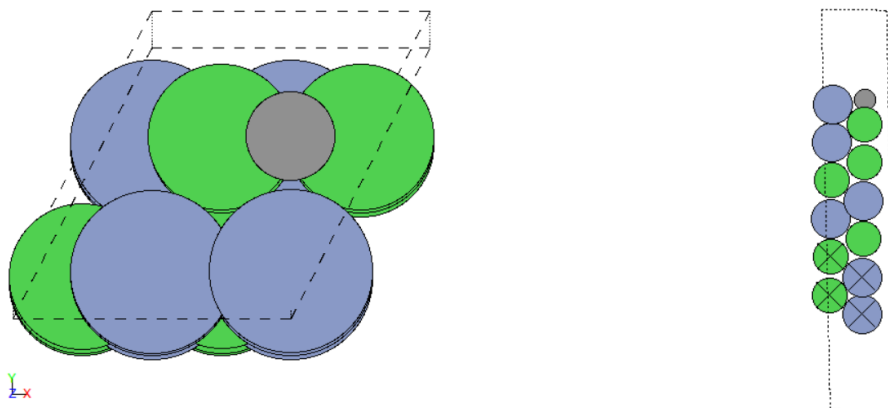


Figure 3.32 The most stable adsorption site for C on Ni_5Cr_5 surface.

The most stable adsorption site is on a bridge between two Ni atoms and the adsorption energy is about 9.3% lower than on the pure Ni surface indicating more favorable interactions between the C and the Cr surface atoms.

3.4.2.2.5 CO and O co-adsorption

We further studied the co-adsorption model for CO and O on Ni_5Cr_5 surface by putting CO on its most stable adsorption site, bridge 2Cr site and O atom occupying other available sites on the surface. The most stable configuration for CO and O on Ni_5Cr_5 surface is when CO occupies the bridge 2Cr site and O possess the hcp 1Ni-2Cr site, as Figure 3.33 shows.

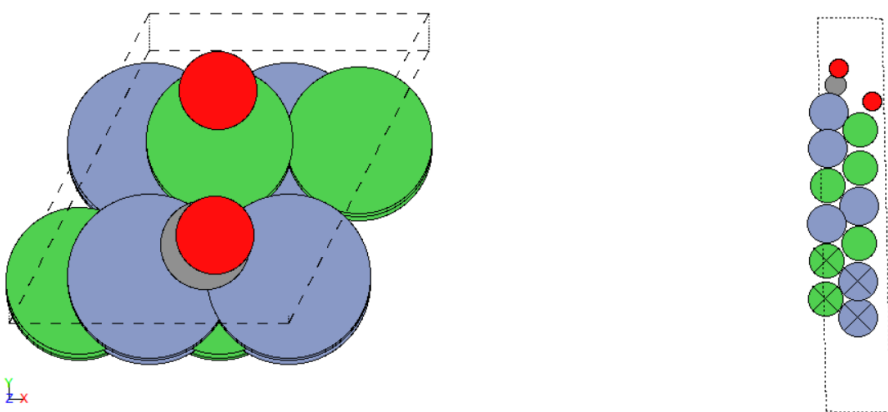


Figure 3.33 Adsorption model for CO and O co-adsorption on Ni_5Cr_5 .

The adsorption energy for the co-adsorption is -7.68 eV so the co-adsorption is thermodynamically favorable and more stable than on pure Ni surface. The bond length between C and nearest Cr is 1.97 Å and that for O and nearest Ni is 2.01 Å. The distance between CO and O is 2.54 Å. The adsorption energy is 1.08 eV lower than that on pure Ni surface but 1.29 eV higher than that on $\text{Ni}_{8.33}\text{Cr}_{1.67}$ indicating that the interaction between the adsorbates and the alloy surface is much more stable than pure metal but less stable than on $\text{Ni}_{8.33}\text{Cr}_{1.67}$. The bond length between adsorbates and alloy surface is the same as on the Ni surface.

This co-adsorbate structure is also 0.68 eV lower in energy than the mono-adsorbates in the same adsorption site suggestion significant attractive interaction between the two.

3.4.2.2.6 C and O co-adsorption

We investigated the co-adsorption model for C and O on Ni_5Cr_5 surface. The co-adsorption model for C atom and O atom is studied by putting C on its favored adsorption site, bridge 2Cr site and O on all other available sites to determine the most stable configuration for C and O co-adsorption. The structure where C occupies bridge 2Cr site while O stays on the adjacent fcc 1Ni-2Cr site is the most stable adsorption model for C and O co-adsorption on Ni_5Cr_5 alloy. The results are shown as Figure 3.34.

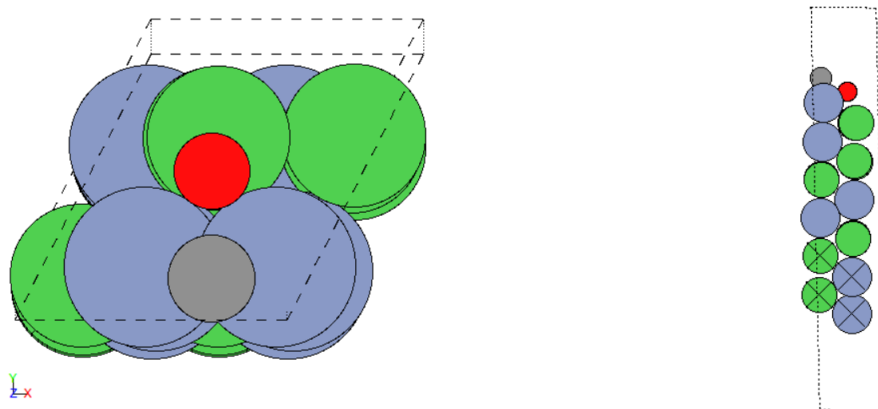


Figure 3.34 Adsorption model for C and O co-adsorption on Ni_5Cr_5 alloy.

The adsorption energy is -9.91 eV indicating that the structure is thermodynamically stable. The bond length between C and Cr atom is 1.87 Å. The bond length of adsorbed O to nearest Cr is 1.93 Å and that for O to nearest Ni is 2.05 Å. The bond length between C and O is 1.87 Å.

The adsorption energy is 1.05 eV lower than that on pure Ni surface but 2.94 eV higher than that on $\text{Ni}_{8.33}\text{Cr}_{1.67}$ surface indicating that the interaction between the adsorbates and alloy surface is more stable than pure metal but less stable than $\text{Ni}_{8.33}\text{Cr}_{1.67}$. The bond length between adsorbates and alloy surface is the same as on the Ni surface and $\text{Ni}_{8.33}\text{Cr}_{1.67}$.

This co-adsorbate structure is also 0.42 eV lower in energy than the mono-adsorbates in the same adsorption site suggesting significant attractive interaction between the two.

3.5 Nudged Elastic Band (NEB) calculation

We have obtained the most stable adsorption site for CO_2 physisorption, $\text{CO}_2^{\delta-}$, co-adsorption of $\text{CO} + \text{O}$ and $\text{C} + \text{O}$ in the previous section. We performed NEB calculation in this section to determine the activation barrier, backward activation barrier and reaction energy for the activation process of CO_2 on Ni (111) and two elementary steps for CO_2 dissociation on Ni (111) and Ni-Cr alloy. Note in this section, we determined the energy of the initial, final and the transition states but the line between them is only a guide to the eye and not the true minimal energy path.

3.5.1 CO_2 activation and dissociation on Ni (111)

3.5.1.1 CO_2 activation

As described in section 3.4.1.1, the CO_2 molecule is activated before dissociation. Hence, we calculate the activation process for CO_2 activation, the CO_2 physisorption to $\text{CO}_2^{\delta-}$ process. The energy diagram is shown in Figure 3.35.

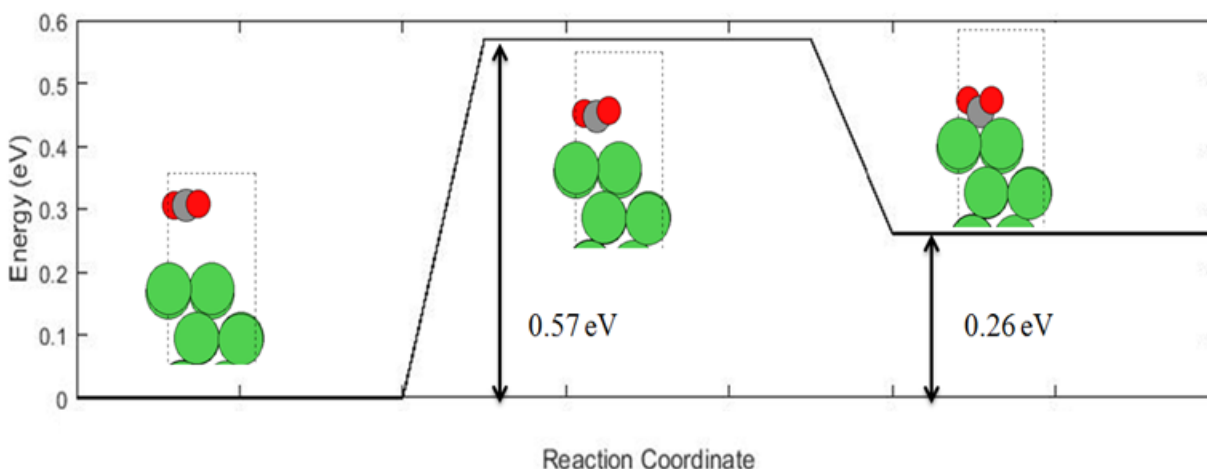


Figure 3.35 Diagram of the reaction energy and activation energy of CO_2 activation. The activation process is slightly endothermic with 0.57 eV activation barriers.

The activation process is endothermic by 0.26 eV and has a 0.57 eV activation barrier the reverse process has 0.31 eV barrier.

3.5.1.2 $\text{CO}_2^{\delta-} \rightleftharpoons \text{CO} + \text{O}$

The activation barrier for $\text{CO}_2^{\delta-}$ dissociation has been determined previously by Catapan et al. [11] and Zhu et al.[56] which found the dissociation barrier to be 0.58 eV and 0.67 eV respectively. We also calculated this dissociation barrier and found it to be 0.61 eV and the overall reaction step to be exothermic by 0.53 eV in good agreement with previous studies. The reverse barrier is 1.14 eV making recombination of CO and O unlikely. The potential energy surface is shown in Figure 3.36

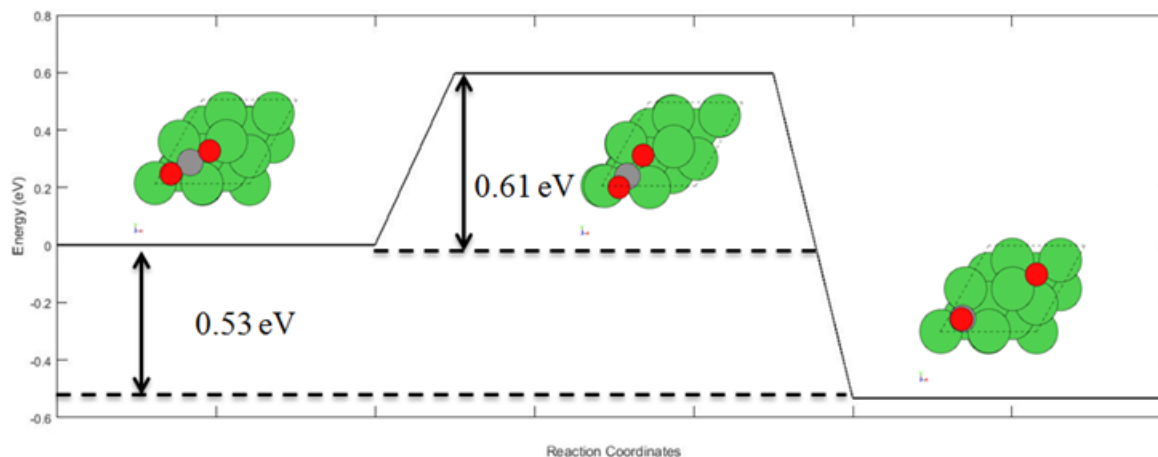


Figure 3.36 Diagram of the reaction and activation energy of the $\text{CO}_2^{\delta-}$ dissociation.

3.5.1.3 $\text{CO} \rightleftharpoons \text{C} + \text{O}$

The energy landscape for the next dissociation step, CO dissociation to C_{ads} and O_{ads} , are shown in Figure 3.37.

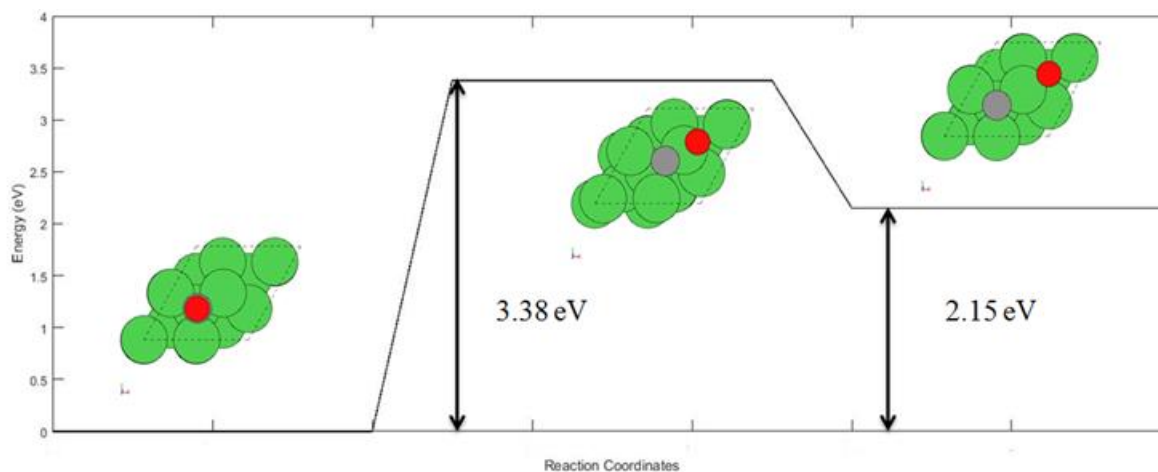


Figure 3.37 Diagram of the reaction and activation energy of the CO dissociation.

This elementary step is endothermic by 2.15 eV with a high forward barrier of 3.37 eV and a backward activation barrier of 1.22 eV in reasonable agreement with previous studies [12].

3.5.1.4. Overall reaction mechanism of CO₂ dissociation on Ni (111)

We combine our NEB result for all three processes, CO₂ activation, CO₂^{δ-} ⇌ CO + O and CO ⇌ C + O for CO₂ dissociation on Ni (111) in Figure 3.38.

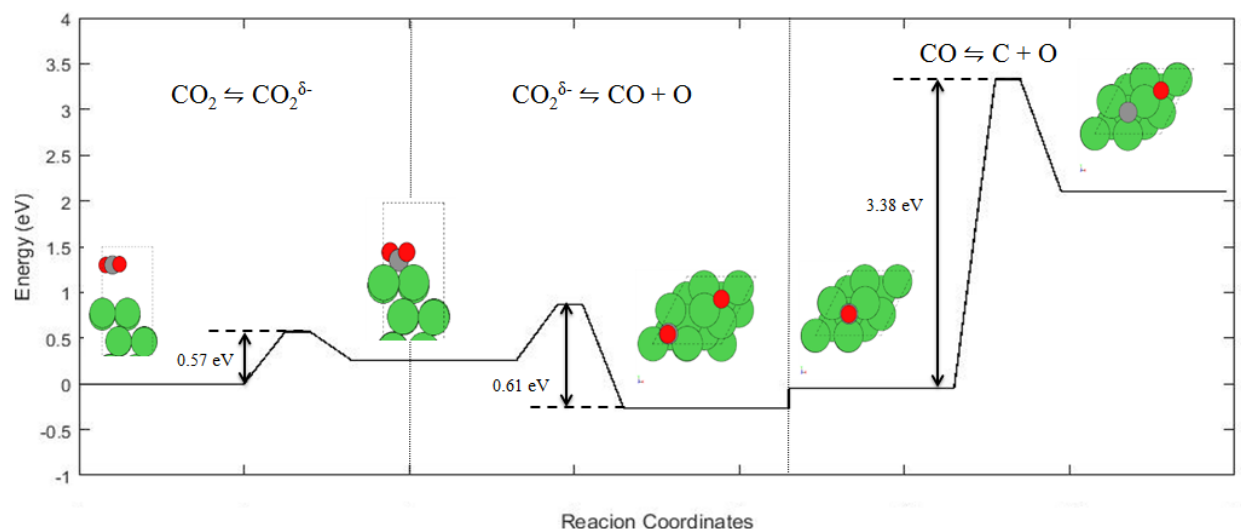


Figure 3.38 Potential energy diagram for the overall reaction mechanism of CO₂ dissociation on Ni (111).

The overall process is endothermic and the highest activation barrier for the overall process is 3.38 eV which is on the third step, the CO dissociation. The step between CO + O and CO removes the interactions between the CO and O since that is not included in the following reaction step, essentially assuming infinite distance between the adsorbates. The high barrier for CO dissociation suggests that Ni will be covered with CO (and O) at low temperatures.

3.5.2 CO₂ dissociation on Ni_{8.33}Cr_{1.67}

3.5.2.1 CO₂^{δ-} ⇌ CO + O

We employed NEB to determine the activation barrier for CO₂^{δ-} dissociation on Ni_{8.33}Cr_{1.67} alloy surface and find it to be exothermic by 1 eV with a 1.44 eV activation barrier in good agreement with previous studies. The reaction energy diagram is shown in Figure 3.39.

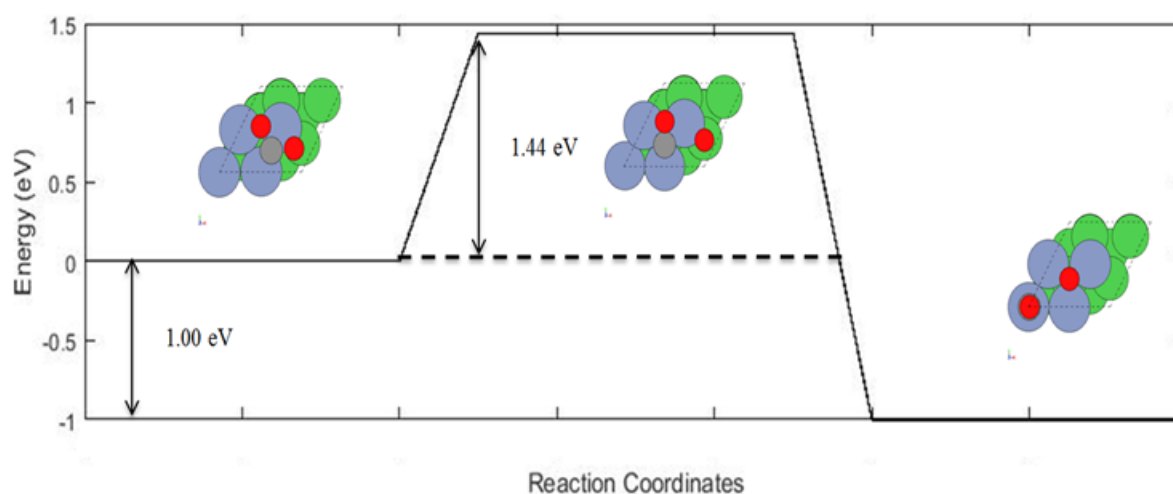


Figure 3.39 Diagram of the reaction energy of the CO₂^{δ-} direct dissociation on Ni_{8.33}Cr_{1.67} alloy surface.

The reverse barrier is 2.44 eV. Comparing the forward activation barrier with the same step on pure Ni surface, the barrier on Ni_{8.33}Cr_{1.67} alloy is nearly 2.36 times larger indicating that CO₂ is more difficult to dissociate on Ni_{8.33}Cr_{1.67} alloy surface and further indicating that Ni-Cr alloy can perform better corrosion resistance than pure Ni in Sc-CO₂ environment.

3.5.2.2 CO ⇌ C + O

We study the dissociation of CO on Ni_{8.33}Cr_{1.67} alloy surface to determine the transition state and the activation barrier. The reaction energy diagram is shown in Figure 3.40.

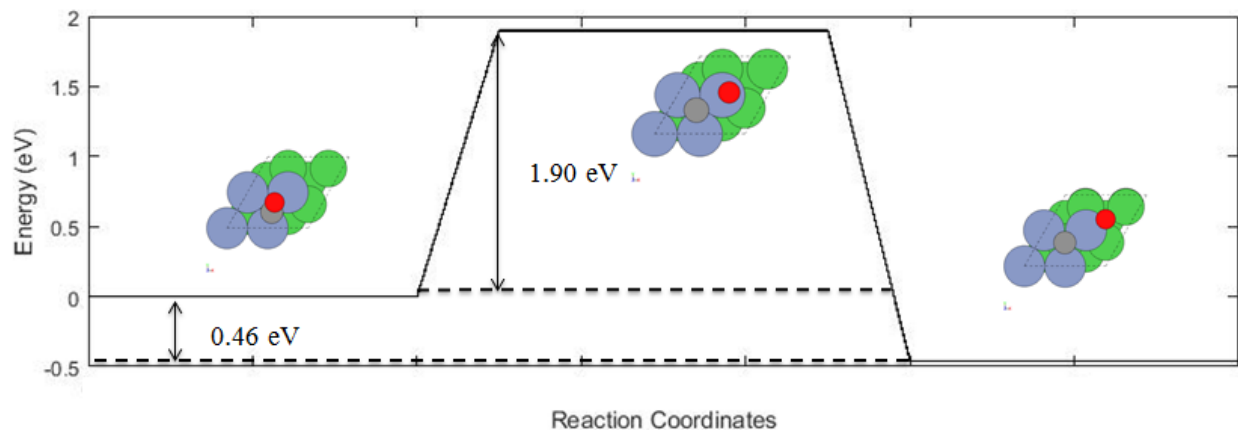


Figure 3.40 Diagram of the reaction energy of the CO dissociation on $\text{Ni}_{8.33}\text{Cr}_{1.67}$ alloy surface.

The activation barrier for CO dissociation is 1.90 eV with the reaction energy of -0.46 eV. The forward reaction is exothermic. The reverse barrier is 2.36 eV. The forward barrier is lower than that on pure Ni surface indicating that the CO is easier to dissociate on the Ni-Cr surface.

3.5.2.3 Overall reaction mechanism of CO_2 dissociation on $\text{Ni}_{8.33}\text{Cr}_{1.67}$ alloy

We combine the two elementary steps for CO_2 dissociation on $\text{Ni}_{8.33}\text{Cr}_{1.67}$ alloy together to reveal the overall mechanism of the process, as shown in Figure 3.4.

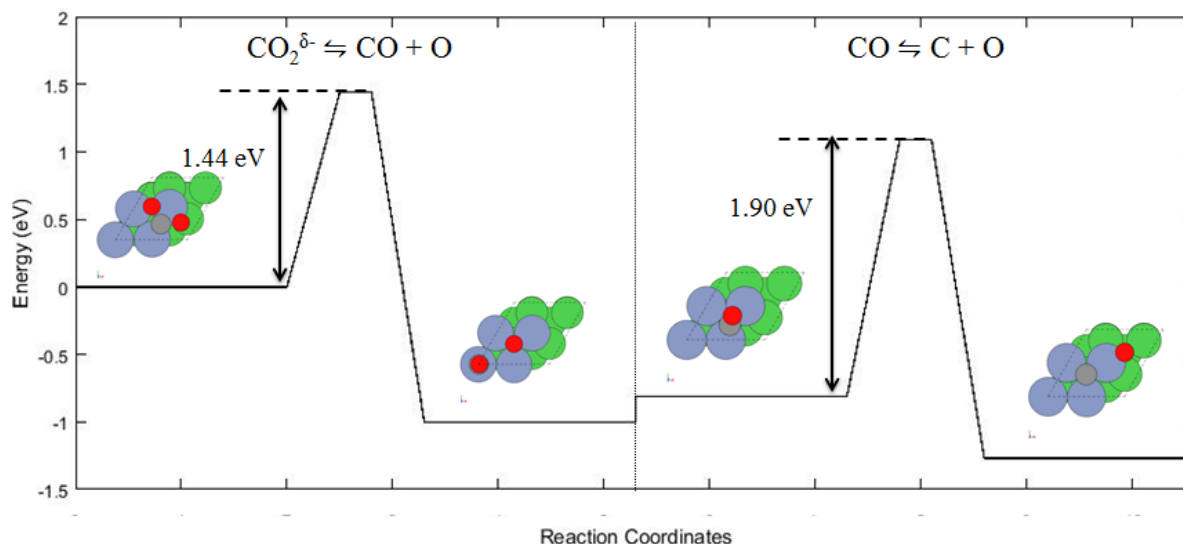


Figure 3.41 Diagram of the reaction energy of the overall reaction mechanism of CO_2 dissociation on $\text{Ni}_{8.33}\text{Cr}_{1.67}$ alloy.

The overall reaction is endothermic. The highest activation barrier for the overall process is 1.90 eV at the CO dissociation step which is lower than that of pure Ni; this is partly driven by the stability the Cr-O indicating that Ni-Cr is more oxophilic than Ni. Comparing with Ni (111), the activation barrier for CO_2 direct dissociation on the alloy surface is 2.36 times higher than Ni (111) indicating that it is hard for CO_2 to dissociate on the alloy surface.

3.5.3 CO_2 dissociation on Ni_5Cr_5

3.5.3.1 $\text{CO}_2^{\delta-} \rightleftharpoons \text{CO} + \text{O}$

We study the first elementary step, $\text{CO}_2^{\delta-}$ direct dissociation into CO and O, on Ni_5Cr_5 alloy surface. The summarized result is shown in Figure 3.42

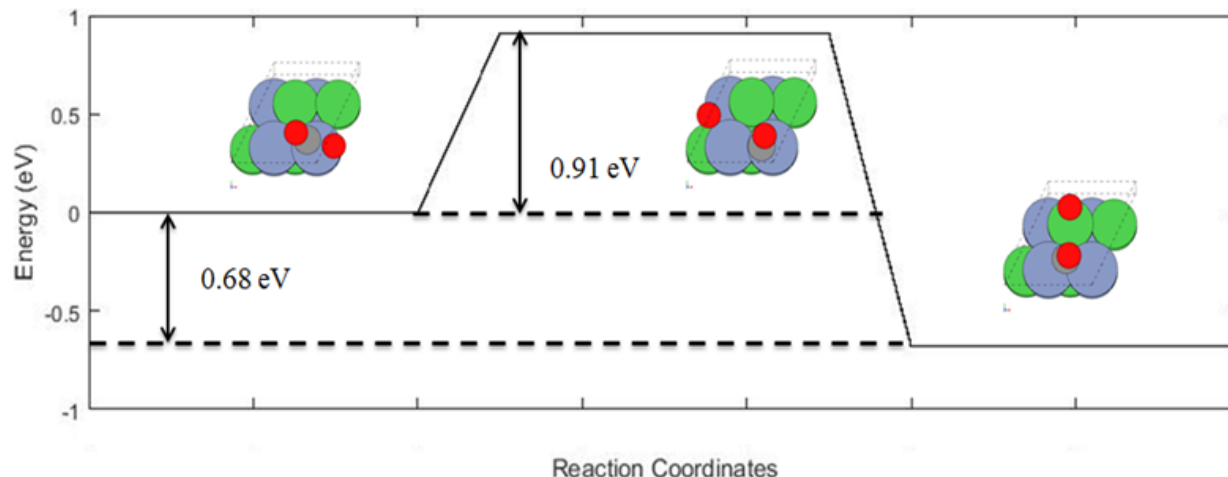


Figure 3.42 Diagram of the reaction energy of the $\text{CO}_2^{\delta-}$ direct dissociation on Ni_5Cr_5 alloy surface.

The dissociation of the activated CO_2 on Ni_5Cr_5 alloy surface, $\text{CO}_2^{\delta-}$, is exothermic with the energy 0.68 eV. The activation barrier for this step is 0.91 eV which is lower than the same step on $\text{Ni}_{8.33}\text{Cr}_{1.67}$ alloy surface but still higher than that on pure Ni surface indicating that Ni_5Cr_5 alloy performs better corrosion resistance in Sc- CO_2 alloy than pure Ni.

3.5.4 Overall minima energy path for CO_2 dissociation on Ni(111), $\text{Ni}_{8.33}\text{Cr}_{1.67}$ and Ni_5Cr_5 surface

We combine our NEB calculation of CO_2 dissociation on the three surfaces we studied together using activated state of $\text{CO}_2^{\delta-}$ as reference state of each of the surfaces and plot the overall minima energy path for CO_2 dissociation on three surfaces as shown in Figure 3.43.

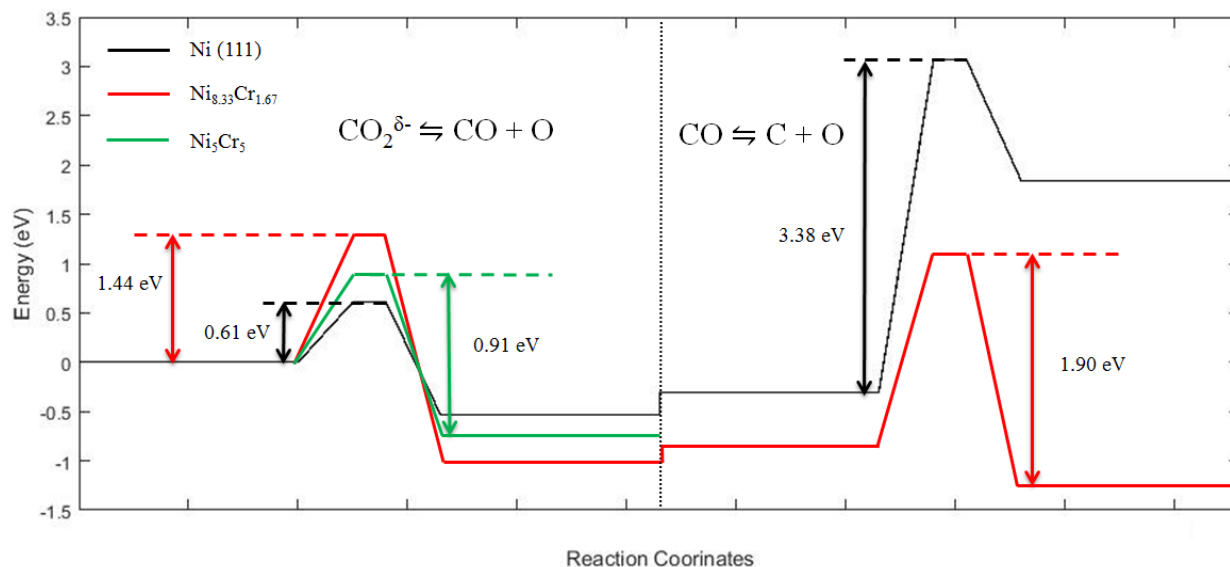


Figure 3.43 Diagram of the overall minima energy path for CO_2 dissociation on Ni (111), $\text{Ni}_{8.33}\text{Cr}_{1.67}$ and Ni_5Cr_5 .

From the Figure, the activation barrier of two types Ni-Cr alloy for the $\text{CO}_2^{\delta-}$ direct dissociation step is higher than that of pure Ni indicating that it is harder for CO_2 to dissociate on the Ni-Cr alloy surface. That is further suggests that Ni-Cr alloys have better resistance to high temperature carburization comparing to pure Ni and can be considered as potential candidate for corrosion resistant material at high temperature in Sc- CO_2 environment.

4 Conclusion and Recommendations for Future Work

Comparing the adsorbate-surface interactions of pure Ni and Ni-Cr alloy shows that oxygen is more stable on the Ni-Cr alloys and the alloy surfaces have higher activation barrier in CO_2 dissociation and the overall process indicating that it is harder for CO_2 to dissociate on the Ni-Cr surface than on the Ni surface. Also the oxide layer is more stable on Cr. This finding can further indicate that Ni-Cr alloy can perform better corrosion resistance in Sc- CO_2 environment.

In Section 1, based on the previous studies of carburization mechanism on the alloy surface, the carbon comes from the CO_2 in environment and after it dissociate on the surface, the carbon will diffuse into the deeper layers [8-14]. If CO_2 dissociation has higher activation barrier, there will be less carbon formed on the alloy surface and decreasing carbon surface concentration and hence the diffusion into the deeper layers. In our study, we found that the Ni-Cr alloy has a higher activation barrier for the CO_2 direct dissociation than pure Ni. So compared to Ni, Ni-Cr alloy has better corrosion resistance for high-temperature carburization. These finding can be used as a reference for future experimental studies towards materials that have ideal corrosion resistance in the Sc- CO_2 environment. The study can be further developed in a number of ways.

Current study has investigated two types of Ni-Cr alloy, Ni_5Cr_5 and $\text{Ni}_{8.33}\text{Cr}_{1.67}$. There are still other types of Ni-Cr alloy that could be investigated for their performance in CO_2 environment. Previous study has shown the most stable structure for several Ni based fcc structured Ni-Cr alloys [23, 26, 43]: $\text{Ni}_{6.7}\text{Cr}_{3.3}$ [23, 43], $\text{Ni}_{7.5}\text{Cr}_{2.5}$ [23], Ni_8Cr_4 [23, 26], as described in Chapter 3. Similar process can be also done on these alloys to determine their corrosion resistance in Sc- CO_2 environment. Further study can be developed on the CO_2 dissociation on pure Cr and Cr based bcc structured Cr-Ni alloys to further understand the role of Cr in CO_2 corrosion resistance. The role of adsorbed oxygen, and Cr oxide layers would also be of great interest. These calculations would be able to provide a complete view towards the corrosion resistance for Ni-Cr alloys in Sc- CO_2 environment and would provide a better reference for future experiments on the corrosion.

Current study only calculate the (111) surface for pure Ni and its alloy since Ni (111) surface is the most stable of the close packed surfaces; different surface structures and defects have been shown to play a critical role in many surface reactions so future studies should be

extended to other surfaces, such as (110) and (211) surface. Catapan et al. [11] studied the CO₂ dissociation on Ni (211) surface and indicated that the activation barrier for the rate limiting step of the overall dissociation process, the CO dissociation, is less than that on Ni (111) surface. They also found CO₂ adsorption to be more stable on Ni (211) than Ni (111) [11]. Detailed studies of other surface structures will provide insights into the role of surface structure in corrosion.

The surface in this study is designed as 2x2x6 surface so the coverage for adsorption is 0.25 ML for mono adsorption and 0.5 ML for co-adsorption. Future studies can be conducted on larger surface to study the effect of coverage on the reaction mechanism. This is especially important for co-adsorption; larger surface provides more adsorption sites and can decrease the interaction between the adsorbates which we found to be significant at these coverages. The larger surface and lower coverage will also allow us to compare a different CO dissociation mechanism $2\text{CO} \rightleftharpoons \text{CO}_2 + \text{C}$ which have been proposed as critical carburization step in Sc-CO₂ environment [8]. Catapan et al. [11] calculated the activation barrier and reaction energy for this reaction on a 2x2 Ni surface and states that it is not stable. Further work is needed on larger surface to determine if this reaction is one of the mechanisms for carburization on Ni and its alloy surface.

The other types of alloys, besides Ni-Cr alloy, may also play a critical role in corrosion resistance in Sc-CO₂ environment. Sarrade et al. suggested a Ni-Al alloy as other candidates for corrosion resistant material at high temperature [2]. This study could be extended to Ni-Al alloys or even mixture of Ni-Cr-Al, to build a more complete picture of the role of different elements in corrosion resistant material in Sc-CO₂ environment.

References

- [1] Wu, Tianbin, and Buxing Han. “Supercritical Carbon Dioxide (CO₂) as a Green Solvent.” *SpringerReference*, 28 Nov. 2012, doi: 10.1007/springerreference_301274.
- [2] Sarrade, et al. “Overview on Corrosion in Supercritical Fluids.” *The Journal of Supercritical Fluids*, vol. 120, 2017, pp. 335–344.
- [3] Marr, and Gamse. “Use of Supercritical Fluids for Different Processes Including New Developments—a Review.” *Chemical Engineering & Processing: Process Intensification*, vol. 39, no. 1, 2000, pp. 19–28.
- [4] Ahn, et al. “Review of Supercritical CO₂ Power Cycle Technology and Current Status of Research and Development.” *Nuclear Engineering and Technology*, vol. 47, no. 6, 2015, pp. 647–661.
- [5] Pint, B., and A. Keiser. “Initial Assessment of Ni-Base Alloy Performance in 0.1 MPa and Supercritical CO₂.” *JOM*, vol. 67, no. 11, 2015, pp. 2615–2620.
- [6] Rouillard, F., et al. “Corrosion Behavior of Different Metallic Materials in Supercritical Carbon Dioxide at 550 Degrees C and 250 Bars.” *Corrosion*, vol. 67, no. 9, 2011, pp. 1–7.
- [7] Firouzdor, et al. “Corrosion of a Stainless Steel and Ni-Based Alloys in High Temperature Supercritical Carbon Dioxide Environment.” *Corrosion Science*, 2013, pp. 281–291.
- [8] Gheno, et al. “Carburization of Ferritic Fe–Cr Alloys by Low Carbon Activity Gases.” *Corrosion Science*, vol. 53, no. 9, 2011, pp. 2767–2777.
- [9] Ko, Jeonghyun, et al. “Density Functional Theory Study for Catalytic Activation and Dissociation of CO₂ on Bimetallic Alloy Surfaces.” *The Journal of Physical Chemistry C*, vol. 120, no. 6, 2016, pp. 3438–3447.

- [10] Mohsenzadeh, et al. "DFT Study of the Water Gas Shift Reaction on Ni (111), Ni (100) and Ni (110) Surfaces." *Surface Science*, vol. 644, 2016, pp. 53–63.
- [11] Catapan, R. C., et al. "DFT Study of the Water-Gas Shift Reaction and Coke Formation on Ni (111) and Ni(211) Surfaces." *J. Phys. Chem. C*, 116 (38), 2012, pp. J. Phys. Chem. C, 2012, vol.116 (38).
- [12] Wang, ShengGuang, et al. "Kinetic Aspect of CO₂ Reforming of CH₄ on Ni (111): a Density Functional Theory Calculation." *Surface Science*, vol. 601, no. 5, 2007, pp. 1271–1284.
- [13] Blaylock, D. Wayne, et al. "Computational Investigation of Thermochemistry and Kinetics of Steam Methane Reforming on Ni (111) under Realistic Conditions." *Journal of Physical Chemistry C*, vol. 113, no. 12, 2009, pp. 4898–4908.
- [14] Wang, ShengGuang, et al. "Chemisorption of CO₂ on Ni Surfaces." *The Journal of Physical Chemistry. B*, vol. 109, no. 40, 2005, pp. 18956–63.
- [15] Han, et al. "Mechanism Studies Concerning Carbon Deposition Effect of CO Methanation on Ni-Based Catalyst through DFT and TPSR Methods." *International Journal of Hydrogen Energy*, vol. 41, no. 20, 2016, pp. 8401–8411.
- [16] Bengaard, et al. "Steam Reforming and Graphite Formation on Ni Catalysts." *Journal of Catalysis*, vol. 209, no. 2, 2002, pp. 365–384.
- [17] Zhang, Riguang, et al. "Insight Into the Effect of Cu-Ni (111) and Fe-Ni (111) Surface Structure and Second Metal Composition on Surface Carbon Elimination by O or OH: A Comparison Study with Ni (111) Surface." *The Journal of Physical Chemistry C*, vol. 119, no. 25, 2015, pp. 14135–14144.

- [18] Liu, et al. “Nanocrystalline Co-Ni Alloy Coating Produced with Supercritical Carbon Dioxide Assisted Electrodeposition with Excellent Wear and Corrosion Resistance.” *Surface & Coatings Technology*, vol. 292, 2016, pp. 37–43.
- [19] Das, Nishith Kumar, and Shoji, Tetsuo. “A Density Functional Study of Atomic Oxygen and Water Molecule Adsorption on Ni (111) and Cr-Substituted Ni (111) Surfaces.” *Applied Surface Science*, vol. 258, no. 1, 2011, pp. 442–447.
- [20] Das, et al. “A Multiscale Modelling Study of Ni–Cr Crack Tip Initial Stage Oxidation at Different Stress Intensities.” *Materials Chemistry and Physics*, vol. 122, no. 2, 2010, pp. 336–342.
- [21] Breidi, et al. “First-Principles Modeling of Energetic and Mechanical Properties of Ni–Cr, Ni–Re and Cr–Re Random Alloys.” *Computational Materials Science*, vol. 117, 2016, pp. 45–53.
- [22] Petrović S, et al. “Structure and Surface Composition of Ni-Cr Sputtered Thin Films.” *Science of Sintering*, vol. 38, no. 2, 2006, pp. 155–160.
- [23] Rahaman, Moshour, et al. “First-Principles Study of Atomic Ordering in fcc Ni-Cr Alloys.” *Physical Review B*, vol. 89, no. 6, 2014, pp. Physical Review B, 2/2014, vol.89 (6).
- [24] Zhang, and Lei. “The States of Nitrogen Atoms in the Processing of Ni–Cr Alloy Surface Nitriding Modification.” *Applied Surface Science*, vol. 301, 2014, pp. 346–350.
- [25] Ortiz-Roldan, Jose M., et al. “Thermostructural Behaviour of Ni-Cr Materials: Modelling of Bulk and Nanoparticle Systems.” *Physical Chemistry Chemical Physics*, vol. 17, no. 24, 2015, pp. 15912–15920.
- [26] Connétable, et al. “First Principle Energies of Binary and Ternary Phases of the Fe–Nb–Ni–Cr System.” *Calphad*, vol. 35, no. 4, 2011, pp. 588–593.

- [27] Sholl, David., and Steckel, Janice A. *Density Functional Theory A Practical Introduction*. Hoboken, Wiley, 2009.
- [28] Nityananda, Rajaram, et al. “Inhomogeneous Electron Gas.” *Resonance*, vol. 22, no. 8, 2017, pp. 809–811.
- [29] Sutcliffe, B, and Woolley. “On the Quantum Theory of Molecules.” *The Journal of Chemical Physics*, vol. 139, no. 22, 2012, pp. The Journal of Chemical Physics, 14 December 2012, vol.139 (22).
- [30] Cohen, Aron J., et al. “Challenges for Density Functional Theory.” *Chemical Reviews*, vol. 112, no. 1, 2012, pp. 289–330.
- [31] Marques, M. *Time-Dependent Density Functional Theory*. Berlin, Springer, 2006.
- [32] Kohn, W., and L.J. Sham. “Self-Consistent Equations Including Exchange and Correlation Effects.” *Physical Review Superseded in Part by Phys. Rev. A, Phys. Rev. B: Solid State, Phys. Rev. C, and Phys. Rev. D*, vol. 140, 1965
- [33] L. J. Sham, *Philos. Trans. R. Soc. Lond. Ser. A-Math. Phys. Eng. Sci.* 355 (163), 481-490 (1991).
- [34] Perdew, J.P. “Generalized Gradient Approximation for the Exchange-Correlation Hole of a Many-Electron System.” *Physical Review, B: Condensed Matter*, vol. 54, no. 23, 1996, pp. 16535–16540.
- [35] Perdew, JP, and Y Wang. “Accurate and Simple Analytic Representation of the Electron-Gas Correlation-Energy.” *Physical Review B*, vol. 45, no. 23, 1992, pp. 13454–13459.
- [36] Perdew, J.P et al. “Local and Gradient-Corrected Density Functionals.” *Chemical Applications of Density-Functional Theory*, 1996, pp. 453-462.

- [3] Kresse, and Furth Müller. “Efficiency of Ab-Initio Total Energy Calculations for Metals and Semiconductors Using a Plane-Wave Basis Set.” *Computational Materials Science*, vol. 6, no. 1, 1996, pp. 15–50.
- [38] Henkelman, G, et al. “A Climbing Image Nudged Elastic Band Method for Finding Saddle Points and Minimum Energy Paths.” *The Journal of Chemical Physics*, vol. 113, no. 22, 2000, pp. 9901–9904.
- [39] Sheppard, Daniel, et al. “Optimization Methods for Finding Minimum Energy Paths.” *Journal of Chemical Physics*, vol. 128, no. 13, 2008, p. 136106.
- [40] Kolsbjerg, Esben L., et al. “An Automated Nudged Elastic Band Method.” *Journal of Chemical Physics*, vol. 145, no. 9, 2016, p. 094107.
- [41] Ortiz-Roldan, Jose M., et al. “Thermostructural Behavior of Ni-Cr Materials: Modelling of Bulk and Nanoparticle Systems.” *Physical Chemistry Chemical Physics*, vol. 17, no. 24, 2015, pp. 16012–16020.
- [42] Ren, et al. “Adsorption and Diffusion of Fluorine on Cr-doped Ni (111) Surface: Fluorine-Induced Initial Corrosion of Non-Passivated Ni-based Alloy.” *Journal of Nuclear Materials*, vol. 478, 2016, pp. 295–302.
- [43] Bai, et al. “Enhanced Stability of the Strengthening Phase $\text{Ni}_2(\text{Cr}, \text{Mo})$ in Ni–Cr–Mo Alloys by Adjacent Instability.” *Computational Materials Science*, vol. 109, 2015, pp. 111–114.
- [44] Wang, SG, et al. “Formation of Carbon Species on Ni (111): Structure and Stability.” *Journal of Physical Chemistry C*, vol. 111, no. 29, 2007, pp. 10894–10903.
- [45] Zhang, et al. “Calculation of the Surface Energy of FCC Metals with Modified Embedded-Atom Method.” *Applied Surface Science*, vol. 229, no. 1, 2004, pp. 34–42.

- [46] Zhang, JianMin, et al. "Calculation of the Surface Energy of Bcc Metals by Using the Modified Embedded Atom Method." *Surface and Interface Analysis*, vol. 35, no. 8, 2003, pp. 662–666.
- [47] Wen, and Zhang. "Surface Energy Calculation of the bcc Metals by Using the MAEAM." *Computational Materials Science*, vol. 42, no. 2, 2008, pp. 281–285.
- [48] Zhang, et al. "Calculation of the Surface Energy of Bcc Transition Metals by Using the Second Nearest-Neighbor Modified Embedded Atom Method." *Applied Surface Science*, vol. 252, no. 23, 2006, pp. 8217–8222.
- [49] Huo, Chun-Fang, et al. "Adsorption and Dissociation of CO as Well as CH_x Coupling and Hydrogenation on the Clean and Oxygen Pre-Covered Co (0001) Surfaces." *Journal Of Physical Chemistry C*, vol. 112, no. 10, 2008, pp. 3840–3848.
- [50] Ge, Q., et al. "A First Principles Study of Carbon-Carbon Coupling over the (0001) Surfaces of Co and Ru." *Journal of Physical Chemistry B*, vol. 106, no. 11, 2002, pp. 2826–2829.
- [51] Li, X, et al. "Density Functional Theory Study of β -Hydride Elimination of Ethyl on Flat and Stepped Cu Surfaces." *The Journal of Chemical Physics*, vol. 127, no. 14, 2007, pp. The Journal of Chemical Physics, 14 October 2007, vol.127 (14).
- [52] Liu, Hongxia, et al. "Insight into the Preferred Formation Mechanism of Long-Chain Hydrocarbons in Fischer Tropsch Synthesis on hcp Co (1011) Surfaces from and Micro kinetic Modeling." *Catalysis Science & Technology*, vol. 7, no. 17, 2017, pp. 3760–3776.
- [53] Ge, Qingfeng, and Matthew Neurock. "Adsorption and Activation of CO over Flat and Stepped Co Surfaces: a First Principles Analysis." *The Journal of Physical Chemistry. B*, vol. 110, no. 31, 2006, pp. 15368–80.

- [54] Loveless, Brett T., et al. "CO Chemisorption and Dissociation at High Coverages during CO Hydrogenation on Ru Catalysts. (Report)." *Journal of the American Chemical Society*, vol. 135, no. 16, 2013, pp. 6107–6121.
- [55] Rahaman, Moshour, et al. "First-Principles Study of Atomic Ordering in fcc Ni-Cr Alloys." *Physical Review B*, vol. 89, no. 6, 2014, pp.
- [56] Zhu, et al. "DFT Studies of Dry Reforming of Methane on Ni Catalyst." *Catalysis Today*, vol. 148, no. 3, 2009, pp. 260–267.
- [57] Eichler, A. "CO Adsorption on Ni (111) - a Density Functional Theory Study." *Surface Science*, vol. 526, no. 3, 2003, pp. 332–340.
- [58] Xu, L., et al. "First-Principles Study on the Geometry and Stability of CO and Hydrogen Coadsorption on the Ni (111) 2x2 Surface. (Report)." *Chemical Physics*, vol. 323, no. 2 3, 2006, pp. 334–340.
- [59] Guo, Gy, and Hh Wang. "Gradient-Corrected Density Functional Calculation of Elastic Constants of Fe, Co and Ni in bcc, fcc and hcp Structures." *Chinese Journal of Physics*, vol. 38, no. 5, 2000, pp. 949–961.
- [60] Casillas-Trujillo, Luis, et al. "Compositional Effects on Ideal Shear Strength in Fe-Cr Alloys." *Journal of Alloys and Compounds*, vol. 720, 2017, pp. 466–472.
- [61] Guo, Gy, and Hh Wang. "Calculated Elastic Constants and Electronic and Magnetic Properties of bcc, fcc, and hcp Cr Crystals and Thin Films." *Physical Review B*, vol. 62, no. 8, 2000, pp. 5136–5143.
- [62] Wei, et al. "Density Functional Theory Study of SO₂-Adsorbed Ni (111) and Hydroxylated NiO (111) Surface." *Applied Surface Science*, vol. 355, 2015, pp. 429–435.

Appendix

Table A1 Total energy of all adsorbates, surfaces and adsorption models.

Surfaces/Adsorbates/adsorption models	Energy (eV)	Surfaces/Adsorbates/adsorption models	Energy (eV)
Single slab/adsorbate:			
Ni (111)	-126.06	Ni _{8.33} Cr _{1.67}	-139.91
Ni ₅ Cr ₅	-163.23	Linear CO ₂	-22.99
O	-1.67	CO	-14.80
C	-1.34	Bent CO ₂ in Ni(111)-CO ₂	-21.01
Bent CO ₂ in Ni _{8.33} Cr _{1.67} -CO ₂	-18.00	Bent CO ₂ in Ni ₅ Cr ₅ -CO ₂	-20.49
Ni(111) adsorption models:			
CO ₂ -physiorption	-149.07		
CO ₂ -2 fold bridge	-148.66	CO ₂ -4 fold bridge	-148.67
CO ₂ -hcp	-148.81	CO ₂ -fcc	-148.69
CO-bridge	-142.66	CO-fcc	-142.75
CO-hcp	-142.77	CO-ontop	-142.43
O-bridge	-132.89	O-fcc	-133.47
O-hcp	-133.37	O-ontop	-131.50
C-bridge	-133.78	C-fcc	-134.19
C-hcp	-134.25	C-ontop	-131.85
CO-O	-149.34	C-O	-140.62
Ni_{8.33}Cr_{1.67} adsorption models:			
CO ₂ -2 fold bridge	-162.63	CO ₂ -4 fold bridge	-162.64
CO ₂ -fcc	-162.57	CO ₂ -hcp	-162.57
CO-bridge	-156.63	CO-fcc	-155.47
CO-hcp	-155.67	CO-ontop	-155.74
O-bridge	-148.72	O-fcc	-147.80
O-hcp	-149.00	O-ontop	-146.05
C-fcc	-147.47	C-hcp	-148.58
C-ontop	-146.47		
CO-O	-165.57	C-O	-156.73
Ni₅Cr₅ adsorption models:			
CO ₂ -physiorption	-186.27		
CO ₂ -bridge 2Ni	-185.38	CO ₂ -bridge 2Cr	-186.85
CO ₂ -fcc 1Ni-2Cr	-186.91	CO ₂ -hcp 2Ni-1Cr	-185.43
CO	-179.92	O	-171.66
C	-172.07		
CO-O	-187.59	C-O	-176.90

Table A2 Structural parameters for all adsorption models studied. The inter-atom distance in this table is the distance of the adsorbates and the nearest adsorbent atom.

Structural parameter(Å)				
Surfaces	Lattice constant		Surfaces	Lattice constant
fcc-Ni	3.52		bcc-Ni	2.82
fcc-Cr	3.68		bcc-Cr	2.83
Ni _{8.33} Cr _{1.67}	3.53		Ni ₅ Cr ₅	3.54
Adsorption Model		Structural parameter(Å)		
Ni(111) adsorption models:				
NiCO ₂	C-O distance		C-Ni distance	C-surface plane distance
physisorption	1.18		4.02	3.83
2 fold bridge	1.27		1.98	1.86
4 fold bridge	1.21		1.99	1.82
hcp	1.26		2.08	1.37
fcc	1.27		2.03	1.54
NiCO	C-O distance		C-Ni distance	C-surface plane distance
bridge	1.19		1.88	1.41
fcc	1.19		1.96	1.33
hcp	1.19		1.94	1.32
ontop	1.16		1.73	1.73
NiO	O-Ni distance		O-surface plane distance	
bridge	1.79		1.22	
fcc	1.84		1.11	
hcp	1.83		1.10	
ontop	1.67		1.67	
Ni-C	C-Ni distance		C-surface plane distance	
bridge	1.72		1.04	
fcc	1.77		0.99	
hcp	1.77		0.98	
ontop	1.64		1.64	
	C-Ni distance	adsorbed O-Ni distance		adsorbate distance
Ni-CO-O	1.98	1.82		2.50
Ni-C-O	1.76	1.83		2.88
Ni _{8.33} Cr _{1.67} adsorption models:				
Ni _{8.33} Cr _{1.67} CO ₂	C-O distance	C-Cr distance	O-Cr distance	C-surface plane distance
2 fold bridge	1.39	1.93	2.05	1.53
4 fold bridge	1.39	1.94	2.05	1.53
fcc	1.31	1.95	1.94	1.53
hcp	1.30	1.95	1.99	1.56

Table A2 (Continued) Structural parameters for all adsorption models studied. The inter-atom distance in this table is the distance of the adsorbates and the nearest adsorbent atom.

Ni _{8.33} Cr _{1.67} CO	C-O distance	C-Cr distance	C-surface plane distance
bridge	1.18	1.88	1.74
fcc	1.19	2.09	1.45
hcp	1.19	2.12	1.57
ontop	1.19	1.88	1.88
Ni _{8.33} Cr _{1.67} O	O-Cr distance	O-surface plane distance	
bridge	1.90	1.24	
fcc	1.90	1.27	
hcp	1.88	1.18	
ontop	1.66	1.66	
Ni _{8.33} Cr _{1.67} C	C-Cr distance	C-surface plane distance	
fcc	1.87	1.22	
hcp	1.86	1.15	
ontop	1.71	1.71	
	C-Cr distance	adsorbed O-Cr distance	adsorbate distance
Ni _{8.33} Cr _{1.67} -CO-O	1.89	1.87	2.86
Ni _{8.33} Cr _{1.67} -C-O	1.83	1.85	2.90
Ni₅Cr₅ adsorption models:			
Ni ₅ Cr ₅ CO ₂	C-O distance	C-surface plane distance	
physisorption	1.35	3.70	
bridge 2Ni	1.19	1.91	
bridge 2Cr	1.21	1.99	
fcc 1Ni-2Cr	1.20	1.94	
hcp 2Ni-1Cr	1.40	1.97	
	C-Cr distance	C-surface plane distance	
Ni ₅ Cr ₅ CO	1.96	1.81	
Ni ₅ Cr ₅ C	1.89	1.57	
	O-Cr distance	O-surface plane distance	
Ni ₅ Cr ₅ O	1.79	1.47	
	C-Cr distance	adsorbed O-Ni distance	adsorbate distance
Ni ₅ Cr ₅ -CO-O	1.97	2.01	2.54
	C-Cr distance	adsorbed O-Cr distance	adsorbed O-Ni distance
Ni ₅ Cr ₅ -C-O	1.87	1.93	2.05
			1.87